Satellite-based $PM_{2.5}$ Exposure Estimation and Health Impacts over China

by

Ming Liu

A thesis
presented to the University of Waterloo
in fulfillment of the
thesis requirement for the degree of
Doctor of Philosophy
in
Geography

Waterloo, Ontario, Canada, 2020

Examining Committee Membership

The following served on the Examining Committee for this thesis. The decision of the Examining Committee is by majority vote.

External Examiner	Dr. Dongmei Chen, Professor Geography and Planning Queen's University
Supervisors	Dr. Jonathan Li, Professor Geography and Environmental Management University of Waterloo
	Dr. Rebecca K. Saari, Assistant Professor Civil and Environmental Engineering University of Waterloo
Internal Member	Dr. Chris Fletcher, Associate Professor Geography and Environmental Management University of Waterloo
	Dr. Michael A. Chapman, Professor Civil Engineering Ryerson University
Internal-external Member	Dr. Linlin Xu, Assistant Professor Systems Design Engineering University of Waterloo

Author's Declaration

This thesis consists of material all of which I authored or co-authored: see Statement of Contributions included in this thesis. This is a true copy of the thesis, including any required final revisions, as accepted by my examiners.

I understand that my thesis may be made electronically available to the public.

Statement of Contributions

The doctoral dissertation is compiled under the manuscript option, following the guidelines provided by the joint Waterloo-Laurier Graduate Program in Geography. One manuscript published in a refereed journal and two manuscripts in the process of review, as listed below, are presented in Chapters 3 to 5 respectively, where the manuscripts have some minor changes for consistent formatting.

1. **Liu M.**, Zhou G., Saari, R.K., Li S., Liu X., *Li J., 2019. Quantifying $PM_{2.5}$ mass concentration and particle radius using satellite data and an optical-mass conversion algorithm. *ISPRS Journal of Photogrammetry and Remote Sensing*. 158, 90–98. (Chapter 3)

2. **Liu M.**, *Saari, R.K., Zhou G., Liu X., *Li J., 2020. Size-differentiated patterns of exposure to submicron particulate matter across regions and seasons in China. *Atmospheric Environment*, minor revision. (Chapter 4)

3. **Liu M.**, *Saari, R.K., Zhou G., Liu X., *Li J., 2020. Recent trends in premature mortality and health disparities attributable to ambient PM2.5 exposure in China during 2005–2017. *Environmental Pollution*, submitted. (Chapter 5)

All these three first-authored manuscripts were written by myself and dominated by my intellectual efforts. The detailed roles of all co-authors are explained below.

For first manuscript, Liu M. conceived the main conceptual ideas, derived the models, wrote and revised the manuscript; Liu M. and Zhou G. developed the computer code and performed the experiments; Saari, R.K., Liu X. and Li J. provided guidance and edited the manuscript. Li S. and all co-authors were involved in the discussion and provided critical feedback and actively participated in the revision of the manuscript. For the second and third manuscript, Liu. M conceived the main original ideas in consultation with Saari, R.K., and wrote the manuscripts; Liu. M and Saari, R.K. devised the experiments and contributed to the final version of the manuscripts. Liu M. and Zhou G. conducted the experiments; Saari, R.K., Liu X. and Li J. supervised the work, involved discussion, and provided critical suggestions. All co-authors helped shape the research, analysis and revision of the manuscripts.

Abstract

Exposure to suspended fine particulate matter ($PM_{2.5}$) has been proven to adversely impact public health through increased risk of cardiovascular and respiratory mortality. Assessing health impacts of $PM_{2.5}$ and its long-term variations requires accurate estimates of large-scale exposure data. Such data include mass concentration and particle size, the latter of which may be an effect modifier on $PM_{2.5}$ attributable health risks. The availability of these exposure data, however, is limited by sparse ground-level monitoring networks.

In this dissertation, an optical-mass relationship was first developed based on aerosol microphysical characteristics for ground-level $PM_{2.5}$ retrieval. This method quantifies $PM_{2.5}$ mass concentrations with a theoretical basis, which can simultaneously estimate large-scale particle size. The results demonstrate the effectiveness and applicability of the proposed method and reveal the spatiotemporal distribution of $PM_{2.5}$ over China. To explore the spatial variability and population exposure, particle radii of $PM_{2.5}$ are then derived using the developed theoretical relationship along with a statistical model for a better performance. The findings reveal the prevalence of exposure to small particles (i.e. PM_1), identify the need for in-situ measurements of particle size, and motivate further research to investigate the effects of particle size on health outcomes. Finally, the long-term impacts of $PM_{2.5}$ on health and environmental inequality are assessed by using the satellite-retrieved $PM_{2.5}$ estimates over China during 2005-2017. Premature mortality attributable to $PM_{2.5}$ exposure increased by 31% from 2005 to 2017. For some causes of death, the burden fell disproportionately on provinces with low-to-middle GDP per capita. As a whole, this work contributes to bridging satellite remote sensing and long-term exposure studies and sheds light on an ongoing need to understand the effects of $PM_{2.5}$, including both concentrations and other particle characteristics, on human health.

Acknowledgements

I would like to express my deepest respect and gratitude to my principal supervisor, Professor Jonathan Li, for the invaluable guidance he provided about academic research and career development, as well as the freedom he gave me to do this work. He has shown me how matters can always be seen differently when viewed from another perspective. I am also impressed with his knowledge of the importance of environmental remote sensing using satellite data and his ability to find a balance between guidance and self-organized problem solving. He always encouraged me to try new and challenging things, guided me to solve one issue after another. I am also deeply indebted to Dr. Rebecca K. Saari, my co-supervisor, for her support, insightful suggestions and encouragement during this study. She has a very kind manner and a rigorous attitude towards academics. She taught me not only knowledge, but also how to be an open-minded and supportive female scholar in action. It is a great honor for me to have her as my co-supervisor and I am looking forward to continuing our collaboration in the future.

My sincere thanks are due to the examiners of my thesis, Prof. Dongmei Chen at Queen's University, Prof. Michael Chapman at Ryerson University, Prof. Linlin Xu, and Prof. Chris Fletcher at the University of Waterloo, for their for their expert review , enlightening suggestions and critical comments.

Many thanks to my colleagues and friends in Li's Lab for Geospatial Sensing and Data Intelligence and Saari's Air Lab at the University of Waterloo for their support and encouragement. Special thanks to Ying Li, Lingfei Ma, Minghao Liu, Yuan Fang, Shuai Yang, Qingyan Min, and Weiya Ye for their help and friendship in my daily life. Thanks also to faculty members in the Department of Geography and Environmental Management, University of Waterloo, Ms. Lori McConnell, and Mr. Alan Anthony for helping me during my study.

Most importantly, I would like to thank my country and the grant from the China Scholarship Council, so that I could have the opportunity to pursue my Ph.D. degree and to have a beautiful experience in Canada.

Dedication

I dedicate this work to the memory of my beloved father, Zhenjiang Liu, who passed away before I finished my first-year doctoral studies. I had promised to make him proud and I hope the achievement of this monumental academic goal could be at least the first step to fulfill this promise. I wish that he could still be alive today to share with me the celebration and the felicity of my graduation with a Doctor of Philosophy degree.

I would also like to dedicate this work to my mother, Yizhe Yuan, who has a strong and gentle soul and never fails to be my best friend. I would not be where I am today without her encouragement and moral support. Special gratitude to my dearest boyfriend for cheering me up on my worst days, for accepting me as I am with my virtues and defects, and for persistently being my side despite the long distance and time difference.

Table of Contents

List of Figures

List of Tables

List of Abbreviations

AE	Angstrom Exponent
AERONET	Aerosol Robotic Network
ANN	Artificial Neural Networks
AOD	Aerosol Optical Depth
BTH	Beijing-Tianjin-Hebei Metropolitan Region
CALIOP	Cloud-Aerosol Lidar with Orthogonal Polarization
CMAQ	Community Multi-Scale Air Quality Model
COD	Causes Of Death
COPD	Chronic Obstructive Pulmonary Disease
CRFs	Concentration-Response Functions
CTM	Chemical Transport Model
CV	Cross Validation
DALYs	Disability-Adjusted Life-Years
DB	Deep Blue
DEM	Digital Elevation Model
DT	Dark Target
EMAC	ECHAM/Messy Atmospheric Chemistry Model
ERF	Exposure-Response Function
GAM	Generalized Additive Model
GBD	Global Burden of Diseases
GDP	Gross Domestic Product
GEMM	Global Exposure Mortality Model
GEOS-Chem	Goddard Earth Observing System Chemical Model with Chemistry
GWR	Geographically Weighted Regression
IER	Integrated Exposure Risk Function
IHD	Ischemic Heart Disease
LC	Lung Cancer
LL	Log-Linear Function
LR	Linear Regression
LRI	Lower Respiratory Infections
LUR	Land Use Regression
MAE	Mean Absolute Error
MBE	Mean Bias Error
MEM	Mixed-Effect Model
NAQPMS	Nested Air Quality Prediction Modeling System
NBSC	National Bureau of Statistics of China
NHFPCC	National Health and Family Planning Commission of China
NLR	Non-Linear Regression
PBLH	Planetary Boundary Layer Height
PM	Particulate Matter
$PM_{1/2.5/10}$	Particulate Matter (aerodynamic diameter <=1 μm/2.5 μm/10μm)
PRD	Pearl River Delta Region
PWA	Population-Weighted Average
RH	Relatively Humidity
RMSE	Root-Mean-Square Error
RR	Relative Risk

SCHIF	Shape Constrained Health Impact Function
TM5	Tracer Model 5
TSM	Two-Stage Model
VIF	Variance Inflation Factor
WHO	World Health Organization
WRF-Chem	Weather Research and Forecasting Model Coupled with Chemistry
WS	Wind Speed
YRD	Yangtze River Delta Region

Chapter 1
Introduction

1.1 Motivation

As a significant component of air pollution, $PM_{2.5}$ (referring to suspended particulate matter with aerodynamic diameters less than 2.5 μm) can penetrate human defense mechanisms, leading to inflammation and allergic reaction, immune system dysfunction and other adverse impacts (Theophanides et al. 2011; Ren et al. 2016). Smaller $PM_{2.5}$ particles may have higher toxicity since their large number and high surface area may increase the risk of absorbing toxic substances (Hoek et al. 2009; Ostro et al. 2015; Samoli et al. 2016). Exposure to $PM_{2.5}$ can increase mortality risks from cardiovascular and respiratory illnesses, among others (Pope C. Arden et al. 2018; Sacks et al. 2011). The Global Burden of Diseases (GBD) study reported that exposure to ambient $PM_{2.5}$ was associated with 4.2 (95% CI: 3.7, 4.8) million premature deaths in 2015 (Cohen et al. 2017). In particular, low- and middle- income countries account for 91% of global attributable premature deaths.

Economic and industrial development has brought great wealth to China during the past decades. Along with this comes unprecedented air pollution levels and resulting unequal health impacts. The population-weighted average (PWA) $PM_{2.5}$ levels in China increased at a rate of 2.10 (95% CI: 1.74, 2.46) $\mu g/m^3$ per year during 2000-2007, before reaching a plateau during 2008-2012 (Xue et al. 2019a). Accordingly, the $PM_{2.5}$-related mortality in China has dramatically risen during this period (Liu et al. 2017b). China alone contributed more than 30% of global $PM_{2.5}$-attributable premature deaths in 2012 (WHO 2016). The exposure and health burden attributed to $PM_{2.5}$ can disproportionately impact vulnerable populations in China (Yang and Liu 2018; Zhao et al. 2019). For example, groups with lower income may experience greater health effects attributable to air pollution (Yang and Liu 2018). Therefore, it is crucial to estimate long-term $PM_{2.5}$ exposure at population scales and investigate its impacts on health and related disparities in China.

While more than 1400 ground-level air quality monitoring sites were established in China since 2013, a fixed-site network cannot represent average exposure across the whole city population due to its limited spatial continuity and coverage (Bell et al. 2007; Madureira et al. 2016). Satellite remote sensing offers an alternative to continuously monitor air pollutants around the world with relatively high spatial resolution and coverage. These techniques are becoming indispensable in ambient $PM_{2.5}$ estimation, which especially benefits regions where verification sites are limited.

Existing satellite-based $PM_{2.5}$ retrieval is based on two main types of methods: statistical models and numerical simulation models. Statistical models, including statistical models and machine/deep learning models, rely on the quantitative relationship between satellite-observed aerosol optical depth (AOD) and ground-level $PM_{2.5}$ measurements. These models have performed well in predicting $PM_{2.5}$ concentrations in a specific spatiotemporal domain (with a large number of training samples), while their interpretability and portability are limited. Numerical simulation models, such as chemical transport models, afford both predictive and explanatory power through simulating aerosol components and behaviors. While multiple studies show the benefit of using numerical models to reduce error in satellite-retrieved $PM_{2.5}$ (Martin 2008; van Donkelaar et al. 2010), these techniques are resource intensive in terms of data, computational resources, expertise and time. Additionally, the simulation performance is susceptible to the uncertainties from simulated chemical and transport mechanisms, emission inventory, atmospheric conditions (including meteorology and chemical composition) and other initial parameters (Chu et al. 2016; Xiao et al. 2017). These two main types present a tradeoff between mechanistic representativeness and efficiency. Several studies have thus focused on establishing theoretical relationships between remotely sensed observations and $PM_{2.5}$ concentrations. Compared with the statistical and simulation methods, theoretical models consider the optic-mass relationship with less computational burden (Lin et al. 2015; Zhang and Li 2015), while inherent properties of aerosol particles, such as radius and refractive index, have not yet been involved in estimations.

However, estimating these microphysical properties of aerosol particles is important to motivate our understanding of their effects on human health. Previous toxicological and epidemiological studies found that smaller particles may have greater toxicity (Chen et al. 2017; Samoli et al. 2016). Compared to large particles, per unit of mass concentration, the large numbers and corresponding surface area of small particles may absorb more toxic substances (Ostro et al. 2015). While epidemiologic relationships have been established for $PM_{2.5}$ mass concentrations and a variety of health endpoints, particle size may be relevant in informing such relationships, for example, via effect modification, or in identifying new ones. Size-resolved particulate matter observations are thus pertinent for exposure assessment. Nevertheless, few studies so far provide large-scale measurements or estimates of particle size for health purposes. Accordingly, no size-related information on surface exposure estimates was included in existing epidemiological studies, including the GBD studies in which satellite AOD observations, GEOS-Chem estimates, and ground-level measurements were adopted.

Though the epidemiologic relationships between particle size and health endpoints have not yet been quantified due to lack of size-resolved exposure data, $PM_{2.5}$ mass concentrations are known to have close associations with various health outcomes (Maji et al. 2018b; Matus et al. 2012). The health and economic burden associated with $PM_{2.5}$ can disproportionately affect vulnerable populations (Bell and Ebisu 2012; Huang et al. 2019; Muller et al. 2018; Zhao et al. 2019). For example, populations with lower income may experience greater health risks attributable to air pollution, especially in regions with higher concentration levels. The damage attributed to air pollution increases health inequality to various degrees among population groups with different income levels (Yang and Liu 2018). Along with significant economic development over the past decades, China has experienced dramatic rises in $PM_{2.5}$ levels and attributable mortality, which further increased income and health inequalities (Azimi et al. 2019; Fang et al. 2010). To alleviate air pollution, the Chinese government has updated air quality standards and issued pollution control policies since 2013. However, to our best knowledge, although studies have explored the effects of these actions on $PM_{2.5}$ concentrations, fewer have evaluated the consequent health impacts and environmental inequality over recent decades in China (Hajat et al., 2015). Understanding how $PM_{2.5}$-related health impact differs among subpopulations is significant to not only achieve and maintain environmental equality, but also provide scientific support for the formulation of targeted environmental policies.

1.2 Objectives of the Study

Following above mentioned motivations, the overall objective of this research is thus to address the gap in population-scale estimates using satellite remote sensing and inform the understanding of the impact of ambient $PM_{2.5}$ on human health, which can be broken down into three sub-objectives:

1. Develop a ground-level $PM_{2.5}$ retrieval method via aerosol microphysical characteristics using satellite remote sensing.

Although satellite-based approaches have been developed and adopted for estimating the concentration of $PM_{2.5}$ with promising accuracy, few studies have considered mass concentration and particle radius simultaneously, even though particle size is significant for human health impacts. We developed a satellite-based $PM_{2.5}$ retrieval method using optical-mass relationships via aerosol microphysical characteristics. Satellite data from the MODIS instrument, combined with parameters from meteorological reanalysis, were processed to calculate particle radii and retrieve $PM_{2.5}$ mass

concentrations over China in 2017. Particle radius and $PM_{2.5}$ concentrations were estimated and validated with station measurements.

2. Reveal the extent of national $PM_{2.5}$ exposure by particle size in the sub-micrometer range.

Air pollution in China has reached unprecedented levels due to rapid economic and industrial development. More than 90% of the Chinese population experiences higher health risks attributable to ambient fine particulate matter exposure. Although evidence suggests that particle size may be an effect modifier on $PM_{2.5}$-related health risks, few studies have explored this due to lack of size-resolved exposure data. Therefore, taking advantage of the established optic-mass relationship in the first objective, we derived size-resolved particle effective radius of $PM_{2.5}$ using satellite optical measurements to explore the spatial variability and population exposure to ambient particle size.

3. Quantify long-term cause-specific premature mortalities and health disparities attributable to $PM_{2.5}$ exposure over China

Economic trends in China have affected public health and wellbeing, including inequality. In the past decade, $PM_{2.5}$ reached unprecedented levels in China and posed a significant threat to public health. Few studies have explored the long-term trajectory of the PM2.5 attributable health burdens and corresponding environmental inequalities in China. We presented the spatiotemporal variations of $PM_{2.5}$ attributable mortality and investigated the corresponding economic and environmental inequality at provincial and national levels over China from 2005 to 2017. Long-term $PM_{2.5}$ exposures over China derived from satellite-based observations and chemical transport models were employed to quantify the attributable excess premature mortality related to five causes of death using the Global Exposure Mortality Model (GEMM). National and interprovincial health inequalities were characterized through environmental Lorenz curves and Gini coefficients over the study period.

1.3 Thesis Contribution

This dissertation comprises three works that develop a satellite-based $PM_{2.5}$-relevant framework to evaluate $PM_{2.5}$ pollution exposure and its long-term health impacts. The contributions can therefore be summarized in three parts as follows.

First, this thesis makes a methodological contribution to satellite-based $PM_{2.5}$ concentration estimation. The relationship between AOD and $PM_{2.5}$ concentrations is built upon theoretical characteristics of aerosols, through which one of the important physical properties (particle radius) and mass concentrations could be derived simultaneously. The developed estimation method quantifies

$PM_{2.5}$ concentrations without introducing regionally-specific fitting parameters, which can be efficiently applied across various spatial and temporal domains. Compared to statistical and numerical models, it requires fewer resources regarding data, computation and expertise.

Second, this thesis fills a significant gap in population-scale (e.g., national) size-resolved observations of sub-micron atmospheric aerosols, which toxicological studies suggest may be more harmful to human health (Lin et al. 2016; Wichmann et al. 2000). Using the theoretical relationships between aerosol microphysical characteristics and satellite optical measurements, the spatiotemporal variability and population exposure to ambient particle size and mass concentrations were explored over China. In identifying the prevalence of submicron exposures, and the confluence of high mass concentrations with small particles, we raise the importance of understanding the effect of particle size on health, while also presenting new tools with which to explore it using national estimates of aerosol composition and size.

Third, this thesis contributes to understanding the health burden and related disparity attributed to ambient $PM_{2.5}$ exposure over China. During recent decades, China has experienced significant economic growth, along with the consequent increased inequality and air pollution levels. Despite the well-studied significance of this health burden, its national trajectory and distribution across vulnerable populations is not well understood. I fill this gap using recent advances in satellite remote sensing techniques, exposure-response relationships, and metrics of environmental inequality. This work uniquely positions trends in air pollution exposure and health risks within the context of economic equality in China. It yields insights for policymakers regarding the effectiveness of efforts to reduce exposures and can help to formulate and monitor targeted policies to address the resulting public health burden and alleviate inequality.

1.4 Thesis Structure

Given the motivations and objectives mentioned above, six chapters are structured in this manuscript-based thesis (Figure 1.1). The current Chapter 1 highlights the significance and main contribution of this work, outlining the need for large-scale and long-term $PM_{2.5}$ retrieval and its related health impact assessment.

Chapter 2 introduces three types of satellite-based $PM_{2.5}$ retrieval methods, providing a methodological foundation for assessing exposure and mortalities attributable to $PM_{2.5}$ pollution. The

advantages and limitations of each method are discussed to clarify why the methods are employed in this dissertation.

Chapter 3 investigates the theoretical optical-mass relationships via aerosol microphysical characteristics to quantify $PM_{2.5}$ mass concentrations without introducing regionally-specific fitting parameters. Mainland China is applied as the case study to quantitatively assess the performance of the proposed method. The estimates were validated against in-situ measurements obtained from China National Environmental Monitoring Center (CNEMC).

Chapter 4 examines and presents the spatiotemporal pattern and population exposure of the size-resolved $PM_{2.5}$ mass concentrations, which is achieved by using the established application of satellite-based observations and aerosol optical-mass relationships. This chapter aims to explore the potential of remote sensing for large-scale $PM_{2.5}$ estimation, including both mass concentrations and particle radius.

Chapter 5 quantifies long-term and national-scale $PM_{2.5}$-attributable premature mortalities related to five causes of deaths during 2005-2017 using the Global Exposure Mortality Model (GEMM). The corresponding national and interprovincial health inequalities were characterized through environmental Lorenz curves and Gini coefficients.

Chapter 6 concludes the main findings of this dissertation. The limitations and recommendations for future research are also included in this chapter.

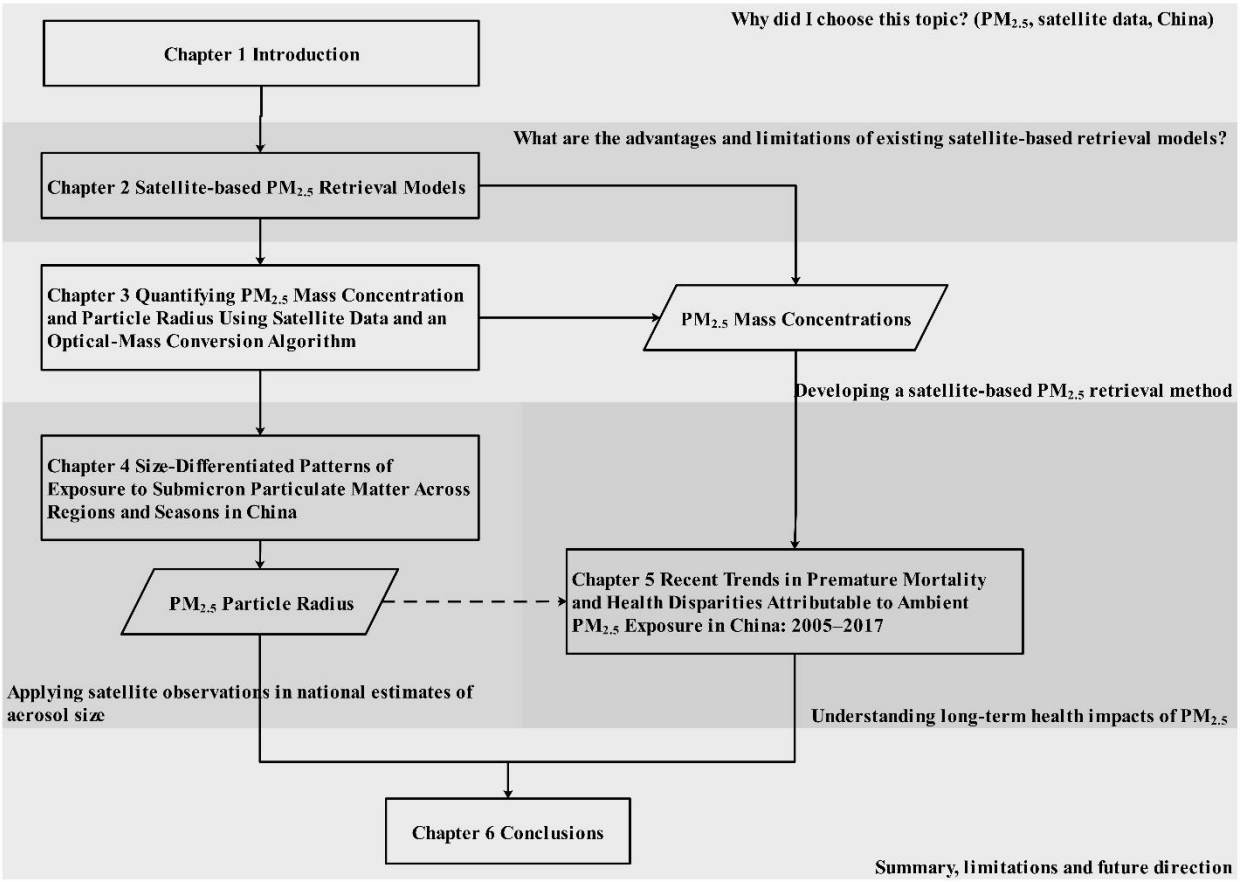

Figure 1.1 Thesis structure

Chapter 2

Satellite-based $PM_{2.5}$ Retrieval

2.1 Basic Principle

2.1.1 Background

Atmospheric particulate matter (PM) refers to a mixture of solid particles or liquid droplets suspended in the atmosphere, which is also known as atmospheric aerosol particles. Since smaller particles are associated with greater health impacts, PM is typically defined by particle size for regulatory and health applications. Particles with aerodynamic diameter less than 2.5μm ($PM_{2.5}$), which can penetrate into the alveoli and even blood stream, are known to have significant adverse health impacts on human health than coarser particles. The chemical composition of $PM_{2.5}$ includes carbonaceous compounds (organic and elemental carbon), water-soluble inorganic ions (e.g. sulfate, nitrate, ammonium etc.), crustal elements (e.g. silicon, aluminum, iron, calcium, sodium, magnesium etc.), heavy metals (e.g. cadmium, arsenic, lead, nickel, copper etc.) and secondary aerosols formed from gaseous precursors (e.g. sulfur dioxide, nitrogen oxide, ammonia and volatile organic compounds) (Huang et al. 2014; Liu et al. 2014; Song et al. 2017; Yin et al. 2012).

The most common approach to measuring ambient $PM_{2.5}$ is through the use of ground-based monitoring stations. Though station-based air quality monitors can provide $PM_{2.5}$ mass with high accuracy and temporal resolution, these in-situ measurements can only represent the concentration in a relatively small area, which cannot reflect the large-scale population exposure and size-resolved observations. Meanwhile, before the Chinese government expanded their air quality monitoring network in 2013, the ground-level measurements from stations were sparse and unbalanced, which makes continuous spatial monitoring difficult, especially for rural and sparsely populated areas.

Satellite remote sensing addresses these drawbacks and provides a possibility to monitor continuously $PM_{2.5}$ with high spatial coverage using Aerosol optical depth (AOD). AOD, which refers to the aerosol extinction (absorption and scattering) in the total vertical column of atmosphere at a given wavelength, has proven to be highly associated with $PM_{2.5}$ concentrations (Chen and Tian 2010; Feng et al. 2018; You et al. 2015). The fact that ground-level $PM_{2.5}$ contributes to satellite-derived AOD provides a significant premise and theoretical foundation to estimate $PM_{2.5}$ concentrations using satellite-derived AOD. Nonetheless, there are many factors that affect the AOD-$PM_{2.5}$ relationship,

such as humidity, the height of the planetary boundary layer, and size fraction (Yang et al. 2019). Specifically, surface $PM_{2.5}$ refers to the mass concentration near the ground, while AOD measures the extinction in the total column of atmosphere; $PM_{2.5}$ refers to the concentration of fine particles under dry condition, while AOD measures the aerosol extinction influenced by water vapor and coarse particles. The aerosol size distribution and chemical composition may also affect the AOD-$PM_{2.5}$ relationship to varying degrees in different spatial and temporal domains. Therefore, it is pertinent to understand the aerosol physical properties related to satellite remote sensing. This information is introduced in the following sections..

2.1.2 Aerosol Optical Properties

Aerosol optical properties are important because they provide insights for aerosol-related measurements. Solar radiation is affected by atmospheric aerosol particles in different ways depending on the relationship of its wavelength to the particle size. Incident radiation on atmospheric aerosols can be absorbed, scattered and reflected, depending on the aerosols' chemical composition and geometric properties (Hatzianastassiou et al. 2007). The combination of aerosol absorption and scattering is known as aerosol extinction.

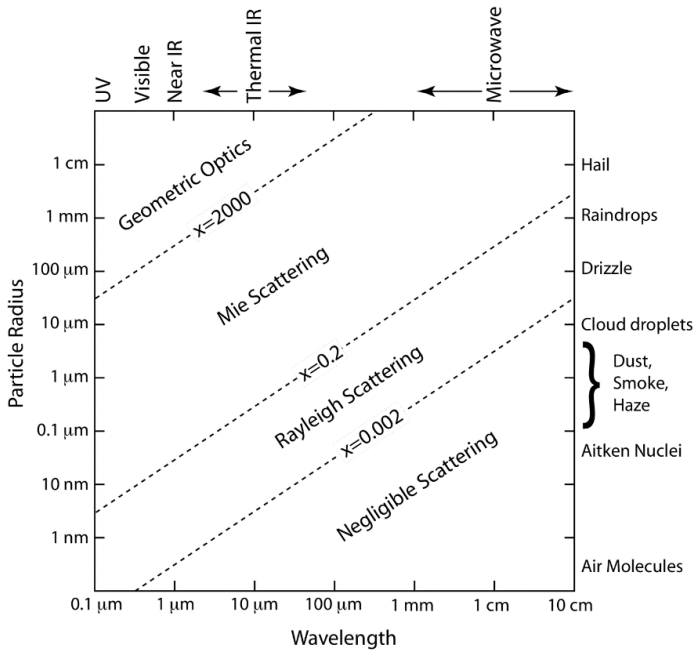

Figure 2.1 Aerosol Scattering Regimes (Pincus 2004)

For one spherical aerosol particle, aerosol extinction characteristics are related to three key parameters: wavelength, complex refractive index and particle size. Complex refraction index ($m=n+ik$) is determined by the aerosol chemical composition. The real part n and the imagery part k are responsible for scattering and absorption, respectively. The "particle size parameter" ($x=2\pi r/\lambda$) is used to describe the size of particles. If $x<<1$, the scattering from molecules (~10^{-4} μm) dominates which follows the Rayleigh scattering regime; if x~1, Mie scattering dominates. Typically, the size of aerosols ranges from 10^{-3} μm to 10 μm, thus the aerosol scattering in the visible and infrared wavelengths primarily follows Mie theory (Figure 2.1). Both m and x depend on wavelength.

According to these three key parameters governing single particle extinction, the aerosol extinction coefficient κ_{ext} can be calculated using Mie theory. The aerosol extinction coefficient is defined as the path length (i.e. the distance passed through the absorbing medium) over which the light intensity is decreased to 1/e. Both aerosol absorption and scattering are wavelength dependent (Eq. 2-1) and obey the Lambert-Beer Law (Eq. 2-2),

$$\kappa_{ext}(\lambda) = \kappa_{sca}(\lambda)+\kappa_{abs}(\lambda) \tag{2-1}$$

$$I(h) = I_0 e^{-(\kappa_{abs}+\kappa_{sca})h} = I_0 e^{-\kappa_{ext}h} \tag{2-2}$$

where κ with subscripts of "ext", "sca" and "abs" are the coefficients of extinction, scattering and absorption; I and I_0 are the light intensity after and before extinction; h is the path length. For the aerosol layer, AOD (τ_a) is defined as the integrated extinction coefficient in the total vertical column, which measures the extinction of solar radiation by aerosol extinction in the total column of atmosphere.

$$\tau_\lambda = \int_0^H \kappa_{ext}(h,\lambda)dh \tag{2-3}$$

where H is the height between surface and top of atmosphere (TOA); Typically, AOD at 0.55 μm ranges from 0 to 2 or higher during episodes of severe air pollution.

In addition to AOD, aerosol optical properties, such as scattering phase function $P(\Theta)$, asymmetry factor (g), and single-scattering albedo (SSA) are also important for aerosol radiative effects assessment (Figure 2.2). $P(\Theta)$ describes the angular distribution of light scattered by aerosol particles, which shows the probability of scattering into angle φ (relative to the incident light) at a certain wavelength. The first moment of $P(\Theta)$ is the asymmetry factor, which is defined as the intensity-weighted average of the cosine of the scattering angle ($g =< cos\Theta >$). The symbol g describes the shape of $P(\Theta)$, ranging from -1 to 1. Typically, the atmosphere is treated as uniform in the horizontal direction while

upward and downward radiation are different. In this case, g is used to approximate the backward and forward scattering direction of radiation. When g<1, this indicates backscattering dominates while g>1 indicates forward scattering dominates. For the most part, satellite sensors capture the backscattering of aerosols and molecules. SSA (ω_0) is a unitless value that describes the ratio of scattering to total extinction, which can be calculated using Mie theory, and is a function of wavelength. ω_0 is an important optical property as it is strongly related to the aerosol direct radiative effect. For example, particles which are lighter in color (like sulfate aerosols) reflect visible light and thus cool the atmosphere, while dark particles (such as black carbon) tend to absorb it, warming the atmosphere. The detailed assumptions and calculations of atmospheric scattering are introduced in (Hansen J E 1974).

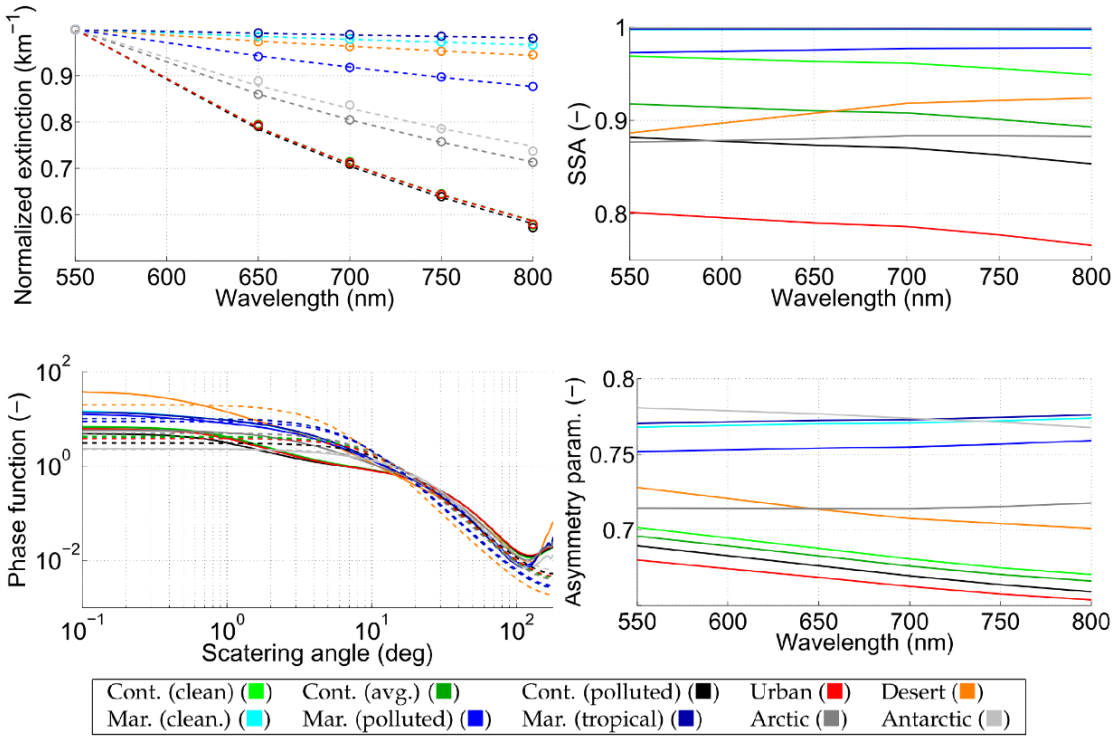

Figure 2.2 Aerosol optical properties in different atmospheric environments (Vicent et al. 2017). (Upper left) normalized $\boldsymbol{\kappa_{ext}}$ and (Upper right) $\boldsymbol{\omega_0}$ by wavelength $\boldsymbol{\lambda}$ of visible light; (Bottom left) phase function at 700nm and (Bottom right) asymmetry parameter with different $\boldsymbol{\lambda}$.

2.1.3 Aerosol Measurement from Passive Satellite Sensors

The extinction by atmospheric aerosols illuminated by the solar beam varies with particle size and composition, which directly impacts the atmospheric radiation budget. In contrast to sun photometers

which measure the downward direct-beam radiation at distinct wavelengths, satellite sensors retrieve aerosol information by observing upward reflected radiation (Kaufman et al. 1997). Satellite remote sensing techniques retrieve aerosol loading and properties at large scale by calculating the variations in radiance caused by atmospheric aerosols, providing reliable observational constraints on global aerosol simulation models. Here, we only discuss radiative transfer in passive remote sensing techniques.

The spectral information captured by a satellite is determined by both atmospheric extinction and surface reflection. In other words, the satellite-derived aerosol information relies on the relationship between observed radiance at the TOA (apparent reflectance, ρ_λ^*) and the surface bidirectional reflectance properties ρ_λ^s. If we assume the Earth surface is a uniform Lambertian surface, the apparent reflectance can be expressed as:

$$\rho_\lambda^*(\theta_0,\theta,\varphi) = \rho_\lambda^a(\theta_0,\theta,\varphi) + F_\lambda(\theta_0)T_\lambda(\theta)\rho_\lambda^s(\theta_0,\theta,\varphi)/\left(1 - s_\lambda\rho_\lambda^s(\theta_0,\theta,\varphi)\right) \quad (2\text{-}4)$$

where $\theta_0, \theta, \varphi$ are solar zenith angle, view zenith angle and the scattered radiation azimuth from solar beam, respectively (Fig. 3); ρ_λ^a is the path radiance; F_λ and T_λ are the normalized downward radiation flux for surface reflectance (downward transmission) and the upward transmission, respectively; s_λ is the ratio of atmospheric backscattering to total light scattering; ρ_λ^s is the surface reflectance.

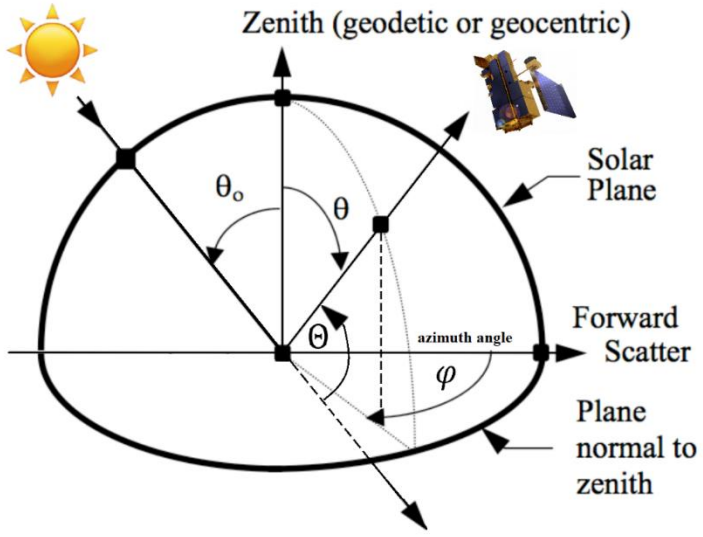

Figure 2.3 Geometry of aerosol radiative transfer

The scattering angle $\Theta = arccos\,(-cos\theta_0 cos\theta + sin\theta_0 sin\theta cos\varphi)$. In the context of single-scattering, the path radiance ρ_λ^a can be calculated based on aerosol optical depth τ_a, phase function $P_a(\theta_0, \theta, \varphi)$ and single scattering albedo ω_0.

$$\rho_\lambda^a(\theta_0, \theta, \varphi) = \rho_\lambda^m(\theta_0, \theta, \varphi) + \omega_0 \tau_a P_a(\theta_0, \theta, \varphi)/4\mu\mu_0 \quad (2\text{-}5)$$

where ρ_λ^m is the path radiance for molecular scattering (Rayleigh scattering); μ and μ_0 are the cosines of the view and solar incident angles, respectively. Substituting this expression into Eq. (2-1),

$$\rho_\lambda^*(\theta_0, \theta, \varphi) = \rho_\lambda^m(\theta_0, \theta, \varphi) + \frac{\omega_0 \tau_a P_a(\theta_0, \theta, \varphi)}{4\mu\mu_0} + \frac{F_\lambda(\theta_0) T_\lambda(\theta) \rho_\lambda^s(\theta_0, \theta, \varphi)}{1 - s_\lambda \rho_\lambda^s(\theta_0, \theta, \varphi)} \quad (2\text{-}6)$$

The molecular Rayleigh scattering and absorption is readily calculated based on radiative transfer calculations for each band. The apparent reflectance ρ_λ^* observed by satellite sensors is a function of aerosol reflectance and surface reflectance. Therefore, the aerosol information is retrieved by distinguishing the aerosol contribution to apparent reflectance. This radiation transfer equation is the theoretical foundation of most aerosol retrieval algorithms.

2.2 $PM_{2.5}$ Estimation Models

With growing attention to air quality and sufficient ground-level observations, various models are subsequently applied in China. I compared the performance of major satellite-based $PM_{2.5}$ retrieval methods applied in China, see Table 2.1**.** These models can be categorized into three main types: statistical models, simulation models, and theory-based models. Each type has its advantages and limitations. Following the objective of each manuscript in this dissertation, all these three types of models were adopted for $PM_{2.5}$ estimation. Specifically, a theory-based model was developed to retrieve $PM_{2.5}$ concentrations via particle radius in Chapter 3. While promising, the accuracy of concentration estimates is limited due to the paucity of particle size samples. Therefore, to achieve a better performance, the statistical model, i.e. a geographically weighted regression (GWR) model was used in Chapters 4 and 5, respectively, for $PM_{2.5}$ concentration estimation. However, the statistical models exhibited a sub-optimal performance before 2013 because of the limited number of historical $PM_{2.5}$ measurements. The simulation results were thus used to investigate long-term health mortalities attributable to $PM_{2.5}$ pollution before 2013 in Chapter 5, which can predict $PM_{2.5}$ without ground-level observations.

Table 2.1 Comparison of major satellite-based $PM_{2.5}$ estimation models in China (n=20)

Types	Method	Study area	Satellite AOD	Resolution (km)	R^2 (N)	Reference
Statistical	LR	Regional (Beijing)	MODIS	30	0.55^{d} (337) - urban; 0.47^{d} (304) - suburb	(Kong et al., 2016)
		Regional (North China)	MODIS	10	0.57^{d} (244); 0.75^{m} (24)	(Xin et al. 2014)
	NLR	Regional (Xi'an)	MODIS MISR	10; 17.6	0.67^{d} (1073) – MODIS; 0.72^{d} (385) - MISR	(You et al. 2015)
	GAM	Regional (Xi'an)	MODIS	10	0.69^{d} (4236)	(Song et al. 2015)
		Regional (Beijing)	MODIS	10	0.61^{d} (126)	(Liu et al. 2012)
	GWR	Regional (PRD)	MODIS	10	0.74^{d} (315)	(Song et al. 2014)
		Regional (YRD)	MODIS	10	0.77^{d}- 0.84^{d} (422-1237) in four seasons	(Jiang et al. 2017)
		National	MODIS	3	0.79^{d} (27813)	(You et al. 2016)
		National	MODIS	10	0.64^{d} (58164)	(Ma et al. 2014)
		National	MODIS	10	0.69^{d} – 0.87^{d} (---)	(Yang et al. 2019)
		Regional (Beijing)	MODIS	3	0.83^{d} (1435)	(Xie et al. 2015)
	MEM	Regional (BTH, YRD, PRD)	MODIS	10	0.77^{d} in BTH, 0.80^{d} in YRD, 0.80^{d} in PRD (~300) 0.71^{a} in BTH, 0.76^{a} in YRD, 0.71^{a} in PRD (~50)	(Zheng et al. 2016)
	TSM	National	MODIS	10	0.41^{d} (79989); 0.73^{m} (5584); 0.79^{s} (2238)	(Ma et al. 2016b)
	ANN	Regional (East China)	MODIS	10	0.30^{d} (---)	(Wu et al. 2012)

Types	Method	Study area	Satellite AOD	Resolution (km)	R^2 (N)	Reference
Simulation	GEOS-chem	National	MODIS MISR	~10	0.55^{m} (~70); 0.72^{m} (~70) in Jan-May 2013	(Geng et al. 2015)
	GEOS-chem	Global	MODIS MISR SeaWiFS	~10	0.66^{a} (210) – excluded Canada, U.S. and Europe	(van Donkelaar et al., 2015)
	GEOS-chem & GWR	Global	Same with above	~10	0.81^{a} (1855)	(van Donkelaar et al. 2016)
Theory-based		Regional (Beijing)	MODIS	10	0.25^{d} (421)	(Zhang and Li 2015)
		Regional (North China)	MODIS	1	0.58^{m} (5557); 0.81^{a} (565)	(Lin et al. 2015)
		Regional (Beijing)	MODIS	10	0.62^{d} (39)	(Tao et al. 2012)

Note: *1) n is the number of selected literature; R^2 is determination coefficient of the methods; N is the number of validation samples; $^{h\ d\ m\ a}$ denote R^2 on an hourly, daily, monthly, annual basis. 2) LR: Linear Regression; NLR: Non-linear Regression; LUR: Land Use Regression; GAM: Generalized Additive Model; GWR: Geographically Weighted Regression; MEM: Mixed-Effect Model; TSM: Two-Stage Model; ANN: Artificial Neural Networks; CTM: Chemical Transport Model; GEOS: Goddard Earth Observing System; WRF: Weather Research and Forecasting Model; CMAQ: Community Multi-scale Air Quality Model; NAQPMS: Nested Air Quality Prediction Modeling System. 3) BTH: Beijing-Tianjin-Hebei Metropolitan region; YRD: Yangtze River Delta region; PRD: Pearl River Delta region.*

2.2.1 Statistical Models

Statistical models rely on the quantitative relationship between satellite-observed aerosol optical depth (AOD) and ground-level $PM_{2.5}$ measurements through diverse statistical models, such as linear regressions (LR) (Kumar et al. 2007; Liu et al. 2005), land use regressions (LUR) (Di et al. 2016; Yang et al. 2017), geographically weighted regression (GWR) models (Jiang et al. 2017; Luo et al. 2017; You et al. 2016), mixed effects models (MEM) (Hu et al. 2014a; Ma et al. 2016b; Yao et al. 2019), generalized additive models (GAM) (Liu et al. 2009, 2012) and artificial neural networks (ANN) (Li 2020; Xue et al. 2019a; Zang et al. 2019; Zhao et al. 2016).

LR was the most popular method in early studies (Liu et al. 2007; Tsai et al. 2011). However, these early retrievals might be biased because of the few covariates and low spatial resolution of input parameters used. Compared with LR, LUR is informative for fine-scale studies with land-use information integration, but it cannot reflect the temporal variance of pollutants since land-use tends to be stable at short time scales while pollutants in the atmosphere are changeable. Therefore, MEM became a dominant method after 2010 because of its flexibility and good performance. Lee et al. (2011) employed MEM, which allows daily variability in AOD-$PM_{2.5}$ relationships to estimate $PM_{2.5}$, with R2 of 0.92 (N=576). Ma et al. (2016) developed a nested linear MEM on a monthly, weekly and daily basis, with R^2 of 0.72 (0.67) using 10km (3km) MODIS AOD. Considering the spatial variation of atmospheric aerosols, GWR and its extended models are increasingly applied for $PM_{2.5}$ retrieval. You et al. (2016) estimate $PM_{2.5}$ concentrations in China through GWR using MODIS 3km AOD (R^2=0.79). Guo et al. (2017) developed a Geographical and Temporal Weighted Regression (GTWR) model in consideration of temporal variation based on the classic GWR and found that this improved model performed better when the number of daily samples was lower than five.

In addition to the models mentioned above, machine learning (ML) and deep learning (DL) techniques have shown considerable potential in PM retrieval in recent years (Gupta and Christopher 2009; Hu et al. 2017b; Li et al. 2017a; Yu et al. 2017; Yuan et al. 2020). Compared to the traditional statistical models, ML/DL models exhibit remarkable capability for establishing nonlinear relationships and require fewer assumptions on data distribution. Xue et al. (2019a) proposed a ML model using multiple variables (including satellite-derived AOD, meteorological parameters, and numerical model results) to estimate and hindcast historical $PM_{2.5}$ concentrations during 2000-2016. Sun et al. (2019) developed a deep neural network (denoted as PM25-DNN) to retrieve hourly $PM_{2.5}$ concentrations in Beijing-Tianjin-Hebei region. In addition to satellite-derived AOD, satellite top-of-atmosphere (TOA) reflectance was also employed as the DL model input to reduce the uncertainty from AOD retrieval.

Shen et al. (2018) established a deep belief network (denoted as Ref-PM) to estimate regional $PM_{2.5}$, demonstrating that TOA-reflectance-derived $PM_{2.5}$ has an edge over AOD-derived $PM_{2.5}$ in terms of spatial resolution and coverage.

Not only can model structure affect performance, but so can aerosol-sensitive factors. Koelemeijer et al (2006) identified that AOD combined with the planetary boundary layer height (PBLH) and relative humidity (RH) shows a strong correlation with $PM_{2.5}$. Meteorological parameters (such as wind direction and cloud cover) (Guo et al. 2017a; Li et al. 2015; Zhang et al. 2015a), land use data (Chen et al. 2016; Yang et al. 2017) and socioeconomic data (Hao and Liu, 2016; Li et al., 2017) are found to be associated with $PM_{2.5}$ as well, and thus employed as the input parameters of retrieval models (Han et al. 2016b; Luo et al. 2017).

These models performed well in estimating $PM_{2.5}$ concentrations, while the model performances are susceptible to the quantity and quality of training data. The empirical parameters in these models vary across spatial and temporal domains, which is difficult to extend to other regions. Additionally, the characteristics of aerosols are not considered in statistical models due to its weak mechanism.

2.2.2 Simulation Models

Compared with statistical models, simulation models have stronger geophysical mechanisms, which offer an alternative to predict $PM_{2.5}$ without ground-based measurements through chemical transport models (CTMs). CTMs can simulate aerosol components and behavior with relatively high spatial (horizontal and vertical) and temporal resolution (Di et al. 2016; van Donkelaar et al. 2015). The basic principle of this approach is to constrain CTMs with "real" (i.e. satellite) AOD observations ($PM_{2.5} = \frac{surface\ simlated\ PM_{2.5}}{simulated\ AOD_{column}} * satellite\ AOD$). Tang et al. (2015) assimilated surface measurements and MODIS AOD into the Community Multiscale Air Quality (CMAQ) model for ozone and $PM_{2.5}$ simulation. van Donkelaar et al. 2010) determined global $PM_{2.5}$ concentrations using GEOS-chem (CTM driven by meteorology from the Goddard Earth Observing System), with R=0.77 (decadal average) in North America. Nevertheless, the performances vary by region and are relatively low. A recent study from Dalhousie University demonstrated that the combination of CTMs and statistical model could improve accuracy. van Donkelaar et al. (2016) employed AERONET (AErosol RObotic NETwork)-calibrated AOD products retrieved from three sensors and CALIOP (Cloud-Aerosol Lidar with Orthogonal Polarization)-corrected AOD simulated from GEOS-Chem to improve AOD accuracy; $PM_{2.5}$ concentrations were then calculated based on the simulated geophysical AOD-$PM_{2.5}$ relationships

from GEOS-Chem. The final $PM_{2.5}$ results were corrected with GWR model and ground $PM_{2.5}$ measurements, with R^2 (0.81) higher than their previous studies (van Donkelaar et al. 2006, 2015).

While multiple studies show the benefit of using CTMs to reduce error in satellite-retrieved $PM_{2.5}$ (Martin 2008; van Donkelaar et al. 2010), these techniques are resource intensive in terms of data, computational resources, expertise and time. Additionally, the performance of simulation results is susceptible to the uncertainties from simulated chemical and transport mechanisms, emission inventory, atmospheric conditions (including meteorology and chemical composition) and other initial parameters (Chu et al. 2016; Xiao et al. 2017).

2.2.3 Theory-based Models

Among the aforementioned two main types of models, there is a tradeoff between mechanism and efficiency. Several studies focused instead on establishing the theoretical relationship between remotely sensed observations and $PM_{2.5}$ concentrations. Compared with the statistical and simulation methods, the theoretical method considers the optic-mass nexus with less computational burden. Typically, theory-based models assumed that atmospheric aerosols are spherical homogeneous particles. An ensemble of aerosols can thus be represented by the distribution of particle size, which can be used to abstract and infer aerosol microphysical properties. The theoretical foundation of these models is selecting an appropriate size distribution that can approximate the actual situation. Among various potential distributions (such as normal and gamma distribution), the logarithmic normal distribution is commonly used for aerosol size characterization. Lin et al. (2015) proposed an indicator describing the synthetic influence of the hygroscopic growth instead of using fixed humidity effect to estimate $PM_{2.5}$ concentration. (Zhang and Li 2015) defined a "particle columnar volume-to-extinction ratio (VE_f)" to establish a $PM_{2.5}$ retrieval algorithm with satellite-derived parameters. Li et al. (2018c) involved multiple datasets to explore the AOD-$PM_{2.5}$ theoretical relationship, considering both size fraction and vertical correction. Their studies contributed to understanding optical-mass physical relationships but still rely on statistical correlations or assumptions, such as the empirical correlation between fine mode fraction (FMF) and VE_f. Therefore, the current theoretical methods can be considered as semi-empirical models which integrate physical mechanisms into regression models. However, regional fitting is still involved, which limits their application across various domains. The aerosol inherent particle properties, such as particle radius and components, have also not been estimated in current theoretical methods.

Chapter 3

Quantifying $PM_{2.5}$ Mass Concentration and Particle Radius Using Satellite Data and an Optical-Mass Conversion Algorithm

In Chapter 3, we present a novel derivation of a theoretical method using satellite-derived parameters for $PM_{2.5}$ retrieval that relies on aerosol microphysical characteristics. This approach, by avoiding a reliance on ground-level $PM_{2.5}$ observations, affords the possibility of greater generalizability to data-poor regions. We fill missing pixels in MODIS products and perform calibration to achieve greater coverage and accuracy. The spatial distribution of mean particle aerodynamic diameters over China is illustrated for the first time according to the proposed method, depicting a clear bifurcation across the country in certain seasons. Based on the derived particle size, daily $PM_{2.5}$ mass concentrations over China in 2017 are then retrieved at a spatial resolution of 3km. Good agreement is found between satellite-retrieved and ground-observed concentrations. This study provides a resource efficient approach to obtain $PM_{2.5}$ concentrations. Additionally, it yields information about particle size, which could potentially fill an important gap in estimating exposure to ultrafine particles, which are thought to be more toxic, but for which large-scale, high-resolution measurements are lacking.

This chapter is structured as follows. Section 3.1 introduces the motivation of this chapter and reviews the previous $PM_{2.5}$ retrieval studies. Sections 3.2 and 3.3 provide the adopted datasets and the main retrieval method, respectively. Section 3.4 demonstrates the model performance and spatiotemporal pattern of $PM_{2.5}$ estimates in China. Section 3.5 discusses the attribution of $PM_{2.5}$ concentration and model uncertainty. Section 3.6 concludes the chapter.

3.1 Introduction

Suspended particulate matter with aerodynamic diameter less than 2.5 μm ($PM_{2.5}$) poses a serious threat to public health through increased risks to mortality, cardiovascular, and respiratory illnesses, among others (de Hartog et al. 2009; Pope C. Arden et al. 2018; Sacks et al. 2011). It is the single greatest global environmental health risk factor identified in the Global Burden of Disease (Cohen et al. 2017). China has experienced severe $PM_{2.5}$ pollution with its recent economic and industrial development. Since 2013, the Chinese government has released air pollutant concentrations to the public. More than 1400 stations provide hourly $PM_{2.5}$ concentrations, which makes $PM_{2.5}$ retrieval and validation feasible (Lin et al. 2015). However, a fixed-site monitoring network restricts the spatial resolution and coverage

of pollutant measurements for the benefit of high accuracy and temporal resolution. In order to obtain the spatial coverage required for full country-level exposure estimates, satellite data are increasingly indispensable in studies of $PM_{2.5}$.

Aerosol optical depth (AOD) observed by satellites is closely associated with $PM_{2.5}$ and often employed to retrieve mass concentrations (You et al. 2015). There are two main methods employed for satellite-based $PM_{2.5}$ retrieval: statistical methods and simulation methods, each with advantages and limitations. Statistical models developed including statistical or artificial intelligence methods have been applied to derive quantitative AOD-$PM_{2.5}$ relationships. Examples include general linear regression models (Kumar et al. 2007; Liu et al. 2005), mixed effects models (Hu et al. 2014b; Yao et al. 2019), generalized additive models (Liu et al. 2009, 2012), land use regression models (Di et al. 2016; Yang et al. 2017), geographical weighted regression models (He and Huang 2018; Li et al. 2017b; Luo et al. 2017; You et al. 2016) and artificial neural networks (Ma et al. 2019; Zhao et al. 2016). In addition to AOD, meteorological parameters, such as planetary boundary layer height (PBLH), relative humidity (RH) and wind speed (Guo et al. 2017a; Zhang et al. 2015a), land use data (Chen et al. 2016; Yang et al. 2017) and socioeconomic data (Hao and Liu 2016) have been found to be associated with $PM_{2.5}$, and were employed as input parameters of various statistical models. Such statistical models have performed very well in representing the variation of ground-level $PM_{2.5}$ concentrations in a specific spatial and temporal domain. However, while their predictive power is high, they do not rely explicitly on scientific relationships, which limits their interpretability. Process-driven numerical simulation models, such as chemical-transport models (CTMs), offer an alternative to obtain mass concentrations that simulate physical and chemical relationships, which afford both predictive and explanatory power (Steyn and Galmarini 2008). CTMs have been shown to simulate aerosol behavior with relatively high spatial (horizontal and vertical) and temporal resolution (Di et al. 2016; Tang et al. 2015). However, the accuracy of simulation results relies on emissions, atmospheric conditions (including meteorology and chemical composition), and simulated chemical and transport mechanisms.

An alternative to statistical and numerical simulation models has been developed to achieve reasonable predictive power and add some explanatory power without the computational expense of a full numerical simulation. With this aim, several methods have been developed focusing on converting optical properties to mass (herein called “optical-mass conversion”). (Lin et al. 2015) proposed an indicator describing the synthetic influence of hygroscopic growth instead of using a fixed humidity effect to estimate $PM_{2.5}$ concentration. Ying Zhang and Li (2015)defined a “particle columnar volume-to-extinction ratio (VE_f)” to establish a $PM_{2.5}$ retrieval algorithm with satellite-derived parameters.

Their studies contributed to the understanding of optical-mass physical relationships, but still relied on model fitting or statistical assumptions in the retrieval, such as the empirical relationship between fine mode fraction (FMF) and VE_f, and fitted parameters for aerosol integrated effect quantification. Additionally, inherent particle properties, such as particle radius, have not been estimated previously. Recent studies suggest that most of the health impacts of $PM_{2.5}$ are caused by particles with a radius less than 2.5μm, such as PM_1 (Chen et al. 2017; Ostro et al. 2015; Samoli et al. 2016). Therefore, understanding size distribution of particles at finer scales is essential for mass concentration retrieval, which then can be applied to better understand the health impacts of $PM_{2.5}$.

This study presents a $PM_{2.5}$ retrieval method with a theoretical basis using satellite observations, meteorological information and ground-level $PM_{2.5}$ measurements, which can simultaneously estimate particle radius. Mainland China is applied as the case study to quantitatively assess the performance of the proposed algorithm. The particle radius and $PM_{2.5}$ concentrations are estimated and validated with station measurements. The advantages and uncertainty of our retrieval method are also discussed.

3.2 Data Collection

3.2.1 Ground Measurements

Hourly average $PM_{2.5}$ observations in 2017 were obtained from the "China National Environmental Monitoring Center (CNEMC) (http://www.cnemc.cn/)". Monitoring stations are mainly situated in southeastern China, reflecting the population distribution. All measurements were calibrated and processed with quality control according to "China's National Ambient Air Quality Standards (GB3095-2012)" and "Environmental Protection Standards (HJ618-2011)" (China 2012). $PM_{2.5}$ concentration was measured by Thermo Fisher 1405 using the "Filter Dynamic Measurements System" and "Tapered Element Oscillating Microbalance". Daily $PM_{2.5}$ concentrations were calculated from hourly measurements during 10:00-14:00 local time.

The Aerosol Robotic Network (AERONET) Version 3 Level 2.0 AOD from 2013 to 2016 were downloaded from http://aeronet.gsfc.nasa.gov/ to calibrate MODIS AOD products in 2017 in order to increase the available calibration samples. AERONET AOD at 0.55 μm were interpolated by AOD at 0.44 μm, 0.67 μm and 0.87 μm, respectively. Many studies (He and Huang 2018; Yang and Hu 2018) used Angstrom's empirical expression, which is related to the Junge distribution (Junge 1955), to interpolate AOD at 550 nm. However, King and Byrne (1976) indicated that particle size distributions

do not follow the Junge distribution and the radii do not extend from zero to infinity. Therefore, we employed the 2nd-order polynomial equation (Eck et al. 1999):

$$\ln \tau_a = a_0 + a_1 \ln \lambda + a_2 (\ln \lambda)^2 \quad (3\text{-}1)$$

where τ_a is AOD at the wavelength of λ. a_0, a_1 and a_2 are the coefficients, which can be fitted by the measurements.

The AERONET data within ± 30 min of satellite overpass time (Terra UTC 2:00-3:00; Aqua UTC 5:00-6:00) were selected and averaged to match the pixel values of MODIS products. There are eight AERONET sites available in 2017 over China, including AOE_Baotou, Beijing, Beijing_PKU, Beijing_RADI, Bejing_CAMS, QOMS_CAS, XiangHe, and XuZhou_CUMT.

3.2.2 Satellite Data

3.2.2.1 MODIS

MODIS is the key instrument aboard the Terra and Aqua satellites, which provides information on aerosol abundance and characteristics at relatively high resolution. The entire Earth surface can be detected by these two satellites every one to two days. There are five bands designed for aerosol retrieval, as shown in Table 3.1. Currently, MODIS provides three retrieval algorithms for aerosol properties over land globally: the "Dark Target (DT)" algorithm, the "Deep Blue (DB)" algorithm and the "Multi-Angle Implementation of Atmospheric Correction (MAIAC)" algorithm (Hsu et al. 2013; Li et al. 2014; Lyapustin et al. 2018). Taking advantage of the high spatiotemporal resolution and relatively long-term observations, MODIS became the most widely used instrument in air quality monitoring. However, because of the limitation of these retrieval algorithms, the accuracy of MODIS AOD is restricted over desert and coastal regions due to the high reflectance and the water-mixed pixels (Chen et al. 2009). Cloud and ice/snow contamination also affect AOD coverage and accuracy (Abdou et al. 2005; Gupta et al. 2006).

With a resolution of 1 km, the MAIAC AOD is informative for local-scale studies. However, considering the geophysical coverage in this study, 3 km DT and 10 km DB AOD Collection 6.1 products from both Terra and Aqua were adopted for $PM_{2.5}$ retrieval. Because of the large uncertainty of MODIS FMF products (Levy et al. 2007), fine mode fraction (FMF) retrieved by the LUT-SDA algorithm was adopted for fine mode AOD. The LUT-SDA algorithm is described and evaluated in previous studies (Yan et al. 2019). The intermediate parameter, Angstrom exponent (AE), was calculated with MODIS AOD at 470 nm and 660 nm.

Table 3.1 MODIS bands used for aerosol properties

Band	Wavelength (nm)	Resolution (m)
3	459–479	500
4	545–565	500
5	1230–1250	500
6	1628–1652	500
7	2105–2155	500

3.2.2.2 Data Preprocessing

Before modelling, AOD products in 2017 were calibrated and gap-filled. Five preprocessing steps were performed for AOD calibration and daily coverage improvement, following (He and Huang 2018; Ma et al. 2016). First, the relationships between MODIS AOD retrievals and AERONET AOD measurements from 2013 to 2016 were established. This timeframe was employed to establish the accuracy of MODIS AOD data due to the limited number of collocated MODIS-AERONET observations in 2017. The relationships are shown in Figure A1, with the correlation coefficients higher than 0.91. Since this relationship shows strong seasonality (Remer et al. 2013), four linear regressions were built for each season and adopted for MODIS AOD calibration in 2017. MODIS AOD includes 3 km DT and 10 km DB products from the Terra and Aqua (Table A1). Next, the MODIS 10 km DB AOD was resampled into 3 km using the cubic convolution resampling algorithm. Then, a linear regression analysis between Terra and Aqua DT (DB) was performed and the regression coefficients obtained were employed to calculate the missing pixels in Terra DT (DB) if there are values in Aqua DT (DB), and vice versa. Furthermore, the variances per satellite per algorithm per season were calculated and used for combining AOD data with an inverse variance weighting (IVW) approach:

$$\mathrm{AOD} = \frac{AOD_{Aqua}/Var_{Aqua_s} + AOD_{Terra}/Var_{Terra_s}}{1/Var_{Aqua_s} + 1/Var_{Terra_s}} \quad (3\text{-}2)$$

where AOD is the satellite-combined DT/DB AOD with IVW; AOD_{Aqua} and AOD_{Terra} are the DT/DB AOD values in Aqua and Terra after calibration and gap filling, respectively; Var_{Aqua_s} and Var_{Terra_s} are the variances of Aqua and Terra AOD in season *s*, respectively. Finally, satellite-combined DB AOD images were used to fill the missing pixels of satellite-combined DT images. The validation and coverage improvement results are shown in Figure A2 and Figure **A3**.

3.2.3 Meteorological Data

Surface meteorological data, including RH, PBLH and visibility (VIS) data, were obtained from the NCEP/NCAR dataset. The "NCEP GDAS/FNL 0.25˚ Global Tropospheric Analyses and Forecast Grids (https://rda.ucar.edu/datasets/ds083.3/)" were downloaded for RH and PBLH, and the "NCEP ADP Global Surface Observational Weather Data (http://rda.ucar.edu/datasets/ds461.0/)" were utilized for VIS, which include more than 1500 stations over China received via the Global Telecommunication System. The NCEP dataset includes 6-hourly analysis products and the products at 12:00 were selected and used in this study.

3.2.4 Data Integration

Both the satellite and the meteorological data were unified with respect to the coordinate system (WGS84), data format, and image size. Daily VIS were interpolated using the inverse distance weighted (IDW) interpolation approach. Following the geophysical coverage of study area and spatial resolution of MODIS AOD, all meteorological data were masked by the extent of China before resampling to 3 km using the cubic convolution interpolation algorithm.

3.3 Methodology

3.3.1 Ground-Level $PM_{2.5}$ Retrieval

The purpose of our work is to retrieve ground-level dry $PM_{2.5}$ mass concentration with an optical-mass conversion algorithm. Several corrections and calculations were thus performed to convert satellite columnar observations into ground-level mass concentrations. The framework of this study is shown in Figure 3.1.

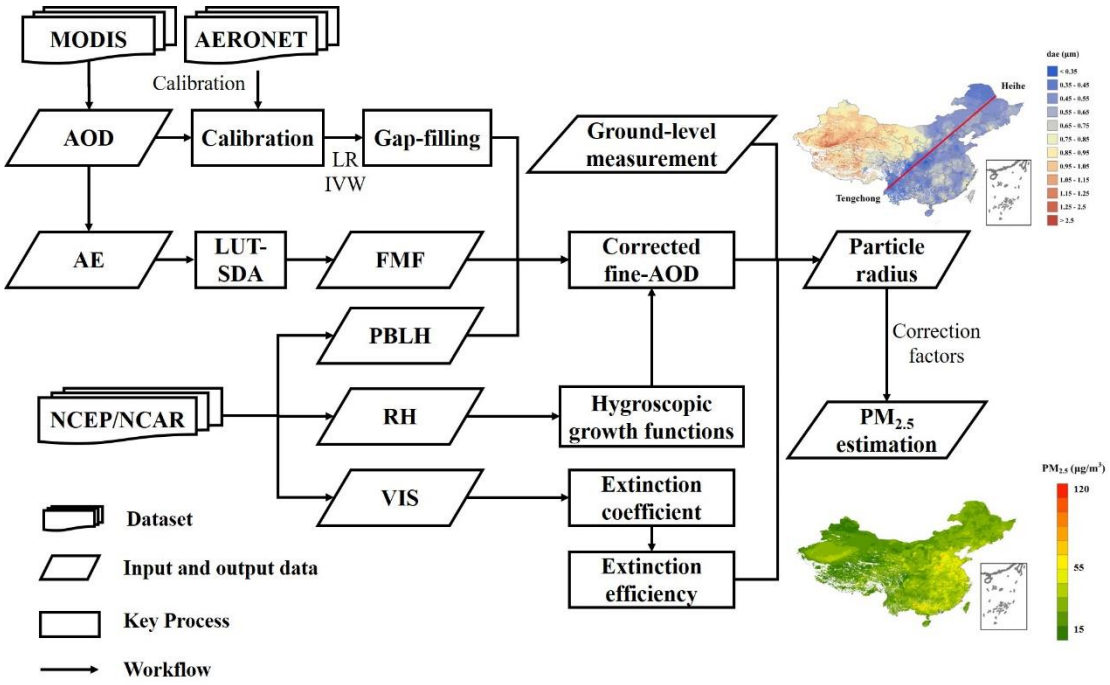

Figure 3.1 Framework of $PM_{2.5}$ retrieval with optical-mass conversion algorithm

AOD, which refers to the aerosol extinction (absorption and scattering) in the total vertical column of atmosphere, must be corrected into the extinction near the ground under dry conditions. According to previous studies (Hansen 1974; Schuster et al. 2006), atmospheric aerosols present a bimodal distribution and the accumulation mode aerosol is superior for use in $PM_{2.5}$ retrieval. Therefore, the FMF was adopted for fine mode AOD calculation:

$$\mathrm{AOD_f} = \mathrm{AOD} * \mathrm{FMF} \tag{3-3}$$

where $\mathrm{AOD_f}$ is the fine mode AOD.

According to (Koelemeijer et al. 2006), both AOD and PM show negative correlations with precipitation (i.e. humidity), but the effect is stronger on AOD. Hence, it is necessary to remove the effect of humidity and boundary layer height on the PM retrieval. Fine 'meteo-scaled' optical depth, $\mathrm{b_{ext,dry}}$ is defined as:

$$\mathrm{b_{ext,dry}} = \frac{\mathrm{AOD_f}}{\mathrm{PBLH} * \mathrm{f(RH)}} \tag{3-4}$$

where f(RH) is the hygroscopic growth function, a function of relative humidity. The formulas of this function are based on three previous studies to diminish the effects of spatial heterogeneity (Appendix A-2) (Chen et al. 2014a; Liu et al. 2008; Zhang et al. 2015b).

According to the physical definition:

$$b_{ext,dry} = \int_0^{\infty} Q_{ext} \pi r^2 \frac{dN}{d \ln r} d \ln r \tag{3-5}$$

where $\frac{dN}{d \ln r}$ is the lognormal particle size distribution, which is described by Eq. (3-6); Q_{ext} is the extinction efficiency through the area distribution, which is defined by Eq. (3-8).

The lognormal particle size distribution was used for accumulation mode aerosols (Hansen 1974):

$$\frac{dN}{d \ln r} = \frac{1}{\sqrt{2\pi}} \cdot \frac{1}{r \ln \sigma_g} \exp\left(- \frac{\left(\ln r - \ln r_g \right)^2}{2 \ln^2 \sigma_g} \right) \tag{3-6}$$

where r_g is the lognormal geometric particle radius and σ_g is the geometric standard deviation. σ_g was set at 2 μm, which refers to the general range (1.75 - 2.25) measured for different types of fine particles (Hobbs et al. 1991; Hofmann and Rosen 1983; Reid et al. 2003; Steele et al. 2006). Since the aerosol extinction properties are proportional to r^2, r_g is not the optimal parameter to represent the distribution. Therefore, the effective radius r_e (a weighted average of particle size distribution) is defined and deduced according to the rule of lognormal distribution (Hansen 1974).

$$r_e = \frac{\int_0^{\infty} r^3 \frac{dN}{d \ln r} d \ln r}{\int_0^{\infty} r^2 \frac{dN}{d \ln r} d \ln r} = r_g \exp(\frac{5 \ln^2 \sigma_g}{2}) \tag{3-7}$$

Similarly, extinction efficiency is defined as

$$Q_{ext} = \frac{\kappa_{ext}}{\int_0^{\infty} \pi r^2 \frac{dN}{d \ln r} d \ln r} = \frac{\kappa_{ext}}{\pi (r_g)^2 \exp(2 \ln^2 \sigma_g)} \tag{3-8}$$

where κ_{ext} is the extinction coefficient, which is inversely proportional to VIS. κ_{ext} can be calculated based on the empirical relationship $\kappa_{ext} = 3.912/\mathrm{VIS}$ (Koschmieder 1924).

Based on these definitions, fine particulate mass concentration under dry conditions at ground level can be derived as:

$$PM_f = \frac{4}{3} \pi \rho \int r^3 \frac{dN}{d \ln r} d \ln r \tag{3-9}$$

where PM_f refers to the fine particulate matter, ρ is the particle mass density, which is assumed to be 1.5 g/cm^3 (Clarisse et al. 2010; Li et al. 2016).

Substituting these expressions into the above equations yields,

$$\mathrm{AOD}_{\mathrm{f}}^{*} = \mathrm{PM}_{\mathrm{f}} * \frac{3\mathrm{Q}_{\mathrm{ext}}}{4\rho r_e} = \mathrm{PM}_f * \frac{3\kappa_{ext}}{4\pi\rho\left(r_g\right)^3 \exp(9/2\ln^2\sigma_g)} \quad (3\text{-}10)$$

Therefore,

$$\mathrm{PM}_{\mathrm{f}} = \frac{\mathrm{AOD} * \mathrm{FMF}}{\mathrm{PBLH} * \mathrm{f(RH)}} * \frac{4\pi\rho\left(\mathrm{r_g}\right)^3 \exp(9/2\ln^2\sigma_{\mathrm{g}})}{3(3.912/\mathrm{VIS})} \quad (3\text{-}11)$$

In Eq. (3-11), AOD, FMF, PBLH, f(RH) and VIS are obtained from satellite and NCEP/NCAR datasets; ρ and σ_g are the constants, and r_g is calculated using ground-based $PM_{2.5}$ measurements. Additionally, we assumed that PM_f derived by AOD_f is equal to $PM_{2.5}$. However, the truncation diameter of AOD_f is smaller than that of $PM_{2.5}$, which could introduce errors into the retrieval (O'Neill et al. 2003). Hence, a correction factor 0.86 was applied to minimize this bias (Li et al. 2016).

3.3.2 Particle Aerodynamic Diameter Calculation

We relate Eq. (3-5) and (3-9) to ground-level r_g in Eq. (3-10), deriving both $PM_{2.5}$ mass concentration and ground-level r_e simultaneously, primarily from satellite-retrieved AOD and meteorological parameters. Ground-level particle radius is purposefully preserved rather than eliminated so that it may also be retrieved, yielding additional insight relevant to understanding exposure to fine and ultrafine particulate matter. Ground-based measurements used in the estimation of r_g were not used to validate retrieved $PM_{2.5}$ mass concentrations, with details as follows.

The particle size of $PM_{2.5}$ was expressed in terms of aerodynamic diameter, d_{ae}, as per the definition of $PM_{2.5}$. To do this, first, all matched samples for each day were randomly divided into five equal size subgroups. A single subgroup was adopted as the validation sample set and the remaining four were employed to calculate particle radius (r_g) using Eq. (3-11). This process was iterated five times, with each of the five subgroups used exactly once for validation. The station-based daily mean particle radius was interpolated using the IDW method with 3 km spatial resolution. We masked the pixels where the corresponding AOD values were not available to reduce bias. The daily particle radius was then averaged to obtain the seasonal spatial distribution. Finally, the seasonal average geometric particle radius was used to find the equivalent aerodynamic diameter. To relate the aerodynamic diameters (d_{ae}) to the geometric diameter (d_g), the volume equivalent diameters d_e is introduced. Assuming that aerosols in the atmosphere are spherical particles, $d_e = d_g$ and $d_g = 2r_g$. Therefore, according previous studies (Hand and Kreidenweis 2002; Raabe 1976):

$$d_{ae} = d_e(\rho/\rho^*)^{1/3} = d_g(\rho/\rho^*)^{1/3} = 2r_g(\rho/\rho^*)^{1/3} \quad (3\text{-}12)$$

where ρ* is the standardizing density equal to 1 g/cm^3.

3.3.3 Method Correction and Validation

There are more than 1500 VIS stations over China, which is comparable with the number of $PM_{2.5}$ sites. The $PM_{2.5}$ concentrations estimated by interpolated VIS are difficult to validate if the VIS stations are close to the PM mass monitoring sites. Therefore, the daily VIS data from the stations near the $PM_{2.5}$ monitoring stations were removed to show the extendibility of the proposed method. A leave-one-out cross validation was conducted to assess accuracy.

Satellite-observed AOD values can be biased or missing due to high surface reflectance or cloud and high aerosol loading, resulting in $PM_{2.5}$ underestimation (Guo et al. 2017b). A correction factor C_i calculated using Eq. (3-13) were adopted to correct these errors:

$$C_i = \frac{PM_{2.5,obs\_i}}{PM_{2.5,est\_i}} \quad (3\text{-}13)$$

where $PM_{2.5,obs\_i}$ and $PM_{2.5,est\_i}$ are the average observed and estimated $PM_{2.5}$ mass concentration at pixel i. The factors were extrapolated to all pixels over the study are using IDW algorithm. The final $PM_{2.5}$ estimation at annual and seasonal scale is calculated by correction factors and uncorrected estimated values.

Five metrics, including Pearson coefficient (R), root-mean-square error (RMSE), mean absolute error (MAE), mean bias error (MBE) and relative percentage error (RPE), were used to assess the retrieval bias.

$$\mathrm{RMSE} = \sqrt{\frac{1}{N}\sum_{i=1}^{N}(est_i - obs_i)^2} \quad (3\text{-}14)$$

$$\mathrm{MAE} = \frac{1}{N}\sum_{i=1}^{N}|est_i - obs_i| \quad (3\text{-}15)$$

$$\mathrm{MBE} = \frac{1}{N}\sum_{i=1}^{N}(est_i - obs_i) \quad (3\text{-}16)$$

$$\mathrm{RPE} = \frac{1}{N}\sum_{i=1}^{N}\left|\frac{est_i - obs_i}{obs_i}\right| \quad (3\text{-}17)$$

where obs_i and est_i are the observed and estimated value of sample i, respectively. $\overline{obs}$ and $\overline{est}$ are the average observed and estimated value. N is the number of validation samples.

3.4 Results

3.4.1 Estimation of Particle Size

Figure 3.2 depicts the mean aerodynamic particle diameter of $PM_{2.5}$, calculated using Eq. (3-12). The mean particle size is larger in the northwest than in the southeast, especially in summer (Figure 3.2b). The division coincides with the Heihe–Tengchong line, which is an imaginary line dividing the territory of China into western and eastern parts (Hu 1935). The results indicate that people living in eastern China (with 43% of the area and 94% of the population in 2015) are exposed to PM with smaller diameters. Although the proportion of smaller particles in summer is higher than that in the other three seasons, the area with the largest particle size (the Taklamakan Desert) also occurred in summer. The AE in the Taklamakan Desert presents larger values in spring and summer compared with that in the other two seasons (Wang et al. 2013). Our results show a similar pattern since AE is inversely associated with particle size. The seasonal variations are also noted by previous studies (Chubarova et al. 2016; Tian et al. 2015). The statistical characteristics of the retrieved particle size are shown in Table 3.2.

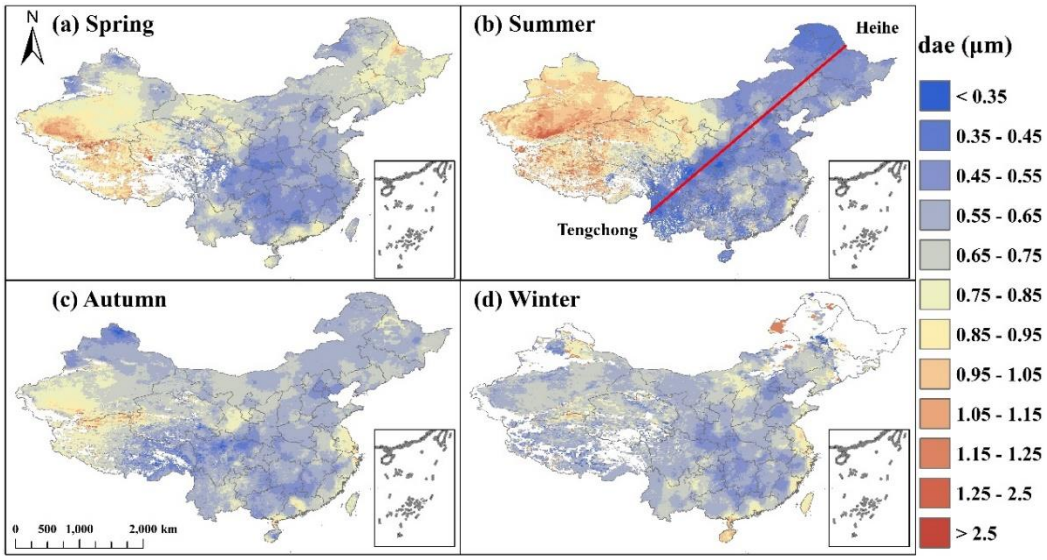

Figure 3.2 Spatiotemporal distribution of aerodynamic diameters over China

The retrieved r_g was also compared with measured values. Effective radius at four AERONET stations (Version 3 Level 2.0) in China were downloaded and calculated for validation. Although there are only 87 retrieved-measured r_g samples in total due to the availability of collocated Level 2.0 data,

this is a good start for large-scale particle size estimation over land, with RMSE of 0.11 μm, which enables diverse particle sizes to be distinguished (Figure 3.3). The relationship is statistically significant at the 0.05 significance level. However, it should be noted that the r_e obtained from AERONET is in the total atmospheric column, while the radius retrieved in our study is at ground level (Prats et al. 2011). The small, positive value of MBE in Figure 3.3 shows that the ground-level radius is larger than the columnar value, which is consistent with the evidence that the aerosol radius decreases slightly with altitude (Baars et al. 2012).

Table 3.2 Statistical characteristic of aerosol aerodynamic diameters (μm)

Season	Minimum	Maximum	Mean	Standard deviation
Spring	0.23	3.23	0.69	0.15
Summer	0.19	6.87	0.69	0.23
Autumn	0.18	4.37	0.64	0.10
Winter	0.20	3.60	0.65	0.11
Annual	0.21	2.86	0.67	0.11

Spring: DOY 60~149; Summer: DOY 150~241; Autumn: DOY242~332; Winter: DOY1~59;333~365; DOY: Day of Year.

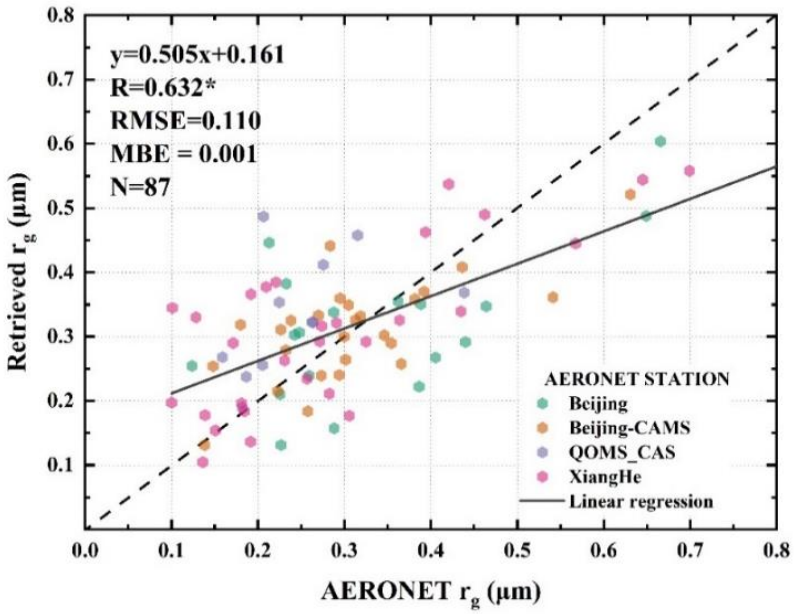

Figure 3.3 Validation of satellite-retrieved and AERONET measurement-retrieved radius in 2017

3.4.2 Temporal Variation of Retrieved $PM_{2.5}$

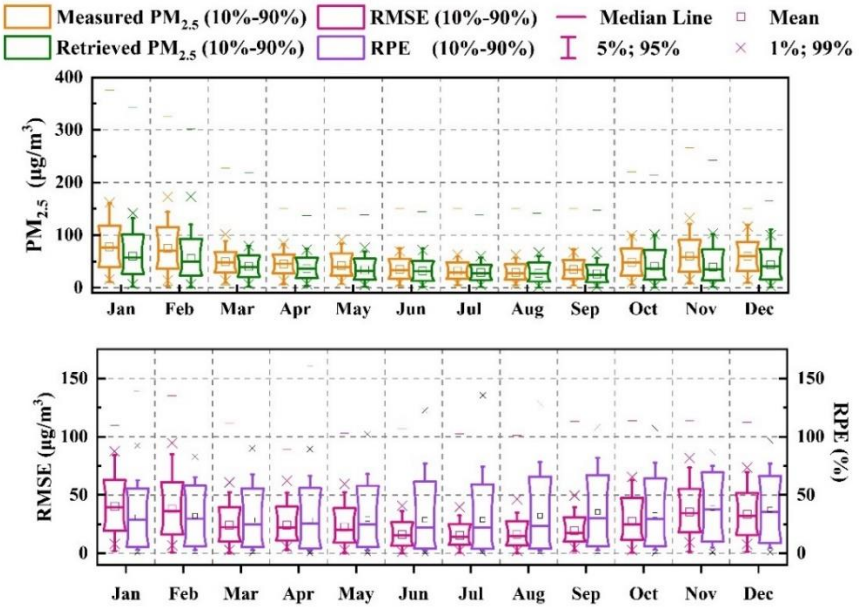

Figure 3.4 Temporal variation of (a) measured and estimated $PM_{2.5}$ concentrations, and (b) RMSE and RPE across China

The monthly variation of measured and estimated $PM_{2.5}$ concentrations across China is shown in Figure 3.4a. As shown, heavily polluted periods are more likely to occur between Jan-Feb and Nov-Dec when heating systems are operating in Northern China. The $PM_{2.5}$ concentration differences among stations in Mar-Sep (spring and summer) are lower than those in other months. These results are consistent with the seasonal distribution of $PM_{2.5}$ (Figure 3.6). Summertime has the lowest $PM_{2.5}$, with seasonal means of 27 $\mu g/m^3$, while winter is the most polluted season with mean concentrations equal to 59 $\mu g/m^3$ in 2017. The highest RMSE also occurred in winter, followed by autumn, spring and summer (Figure 3.4b). The monthly variation of RPE is stable, with an average of 31 %. Additionally, the performance of the proposed method is also evaluated at the seasonal scale (Table 3.3). The highest correlation coefficient is 0.91 in winter, with RMSE of 20$\mu g/m^3$ and RPE of 27%.

Table 3.3 Correlation between seasonal-mean retrieved and in-situ $PM_{2.5}$ concentration.

Season	R	RMSE ($\mu g/m^3$)	RPE	N
Spring	0.77	13	23%	1255
Summer	0.72	9.4	23%	1245
Autumn	0.83	15	27%	1242
Winter	0.91	20	27%	1193

Based on the spatial pattern of annual $PM_{2.5}$ concentrations, five regions, including Beijing-Tianjin-Hebei Metropolitan region (BTH), Yangtze River Delta (YRD), Pearl River Delta (PRD), Sichuan Basin (SB) and Taklamakan Desert (TD), were selected to present regional monthly variation (Figure 3.5). The overall variations among these five areas are similar with that across China and the highest $PM_{2.5}$ values were observed in the BTH region.

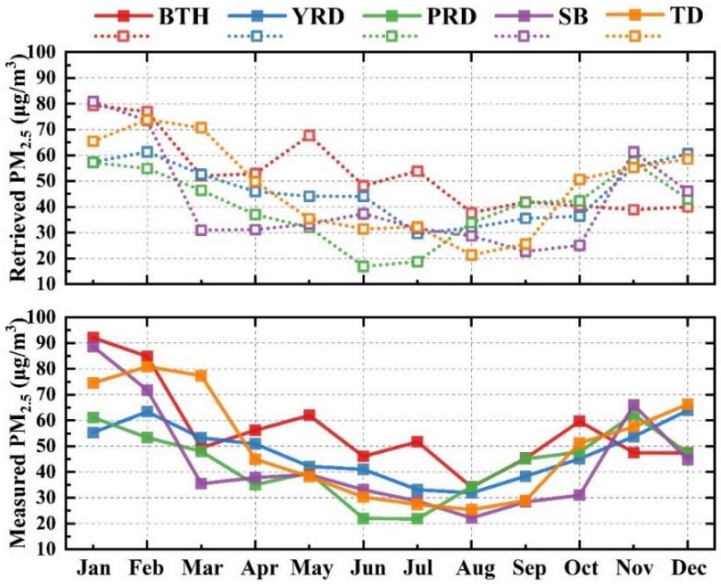

Figure 3.5 Monthly variation of retrieved and measured $PM_{2.5}$ concentrations in the BTH, YRD, PRD, SB and TD region

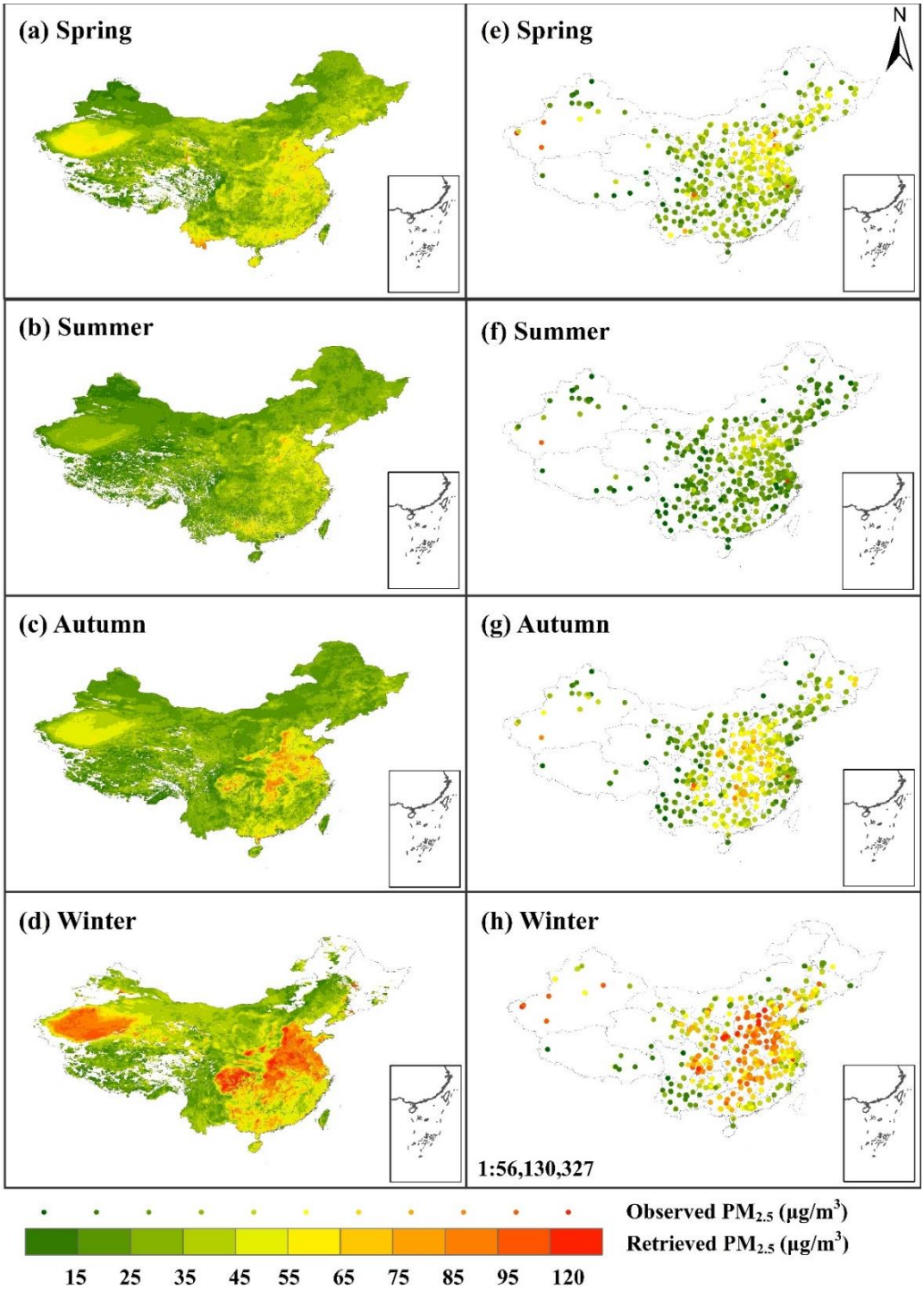

Figure 3.6 Seasonal mean satellite-retrieved $PM_{2.5}$ concentrations

3.4.3 Spatial Distribution of Retrieved $PM_{2.5}$

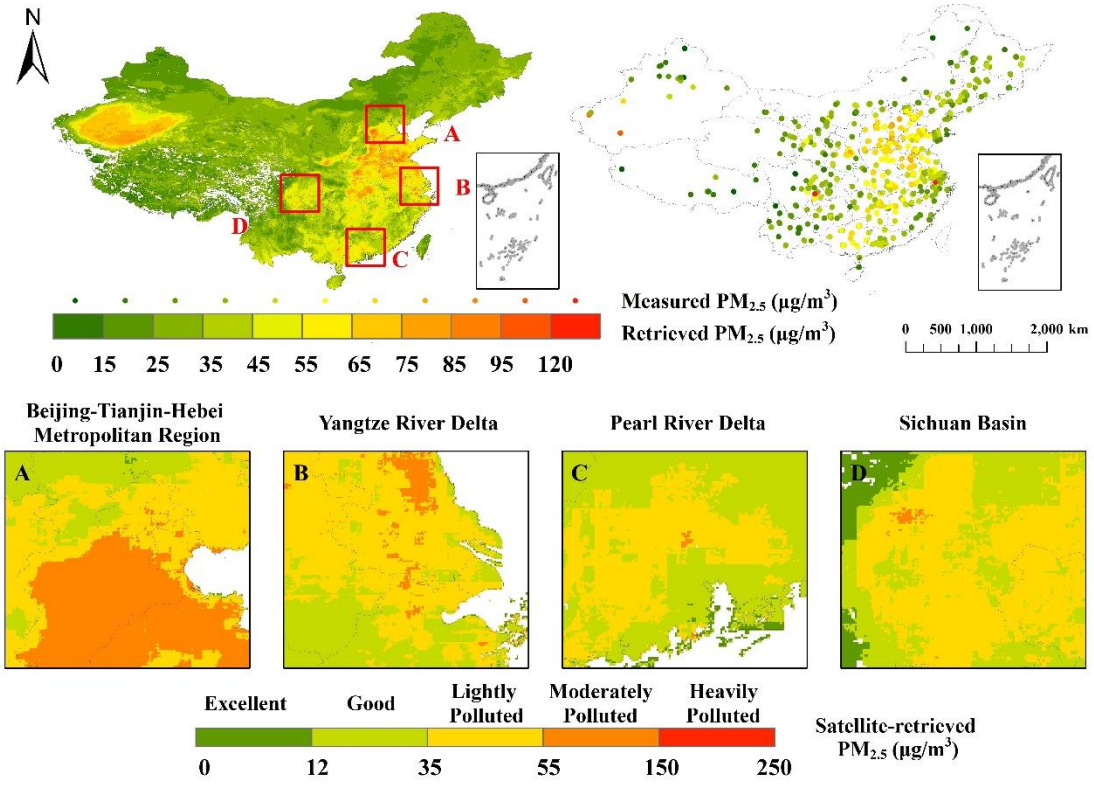

Figure 3.7 Spatial distribution of annual mean satellite-retrieved and ground-based $PM_{2.5}$ concentrations with four hotspots

The annual mean of satellite-retrieved $PM_{2.5}$ concentrations over China was estimated to be 47 μg/m^3. The spatial pattern of the retrieved $PM_{2.5}$ appears to be consistent with that of ground measurements and other studies (van Donkelaar et al. 2010). The BTH region experienced high $PM_{2.5}$ exposures in 2017, with concentrations higher than 55 μg/m^3. Among the four hotspots highlighted in Figure 3.7, the BTH region had the highest annual mean concentrations, followed by the SB, the YRD and the PRD region. Except for the above four regions, high $PM_{2.5}$ levels were also observed in the Taklamakan Desert.

The evaluation of uncorrected estimates is shown in Figure 3.8, which illustrates the underestimation of $PM_{2.5}$ mass concentration. The possible reason is that high aerosol loading might be misclassified into cloud, leading to missing values in satellite images under severe air pollution. Therefore, $PM_{2.5}$ estimates were improved with correction factors and evaluated using ground measurements. The

promising accuracy for annual (R = 0.82, RMSE = 9.2 μg/m^3, MAE=7.0 μg/m^3, MBE=-2.0μg/m^3, RPE = 18%, N = 1270) and seasonal (R = 0.81, RMSE = 12 μg/m^3, MAE=9μg/m^3, MBE=-0.4μg/m^3, RPE = 24%, N = 4932) means are reported in Figure 3.9. The bias of the corrected results might be due to the limited spatio-temporal coverage and uncertainties of input data. Since DT has limited capability of bright surface AOD retrieval, the AOD from 10 km DB could cause uncertainty due to spatial heterogeneity. Meanwhile, sparsely distributed monitoring sites and reduced satellite coverage affected the $PM_{2.5}$ retrieval by reducing the accuracy of the retrieved particle radius.

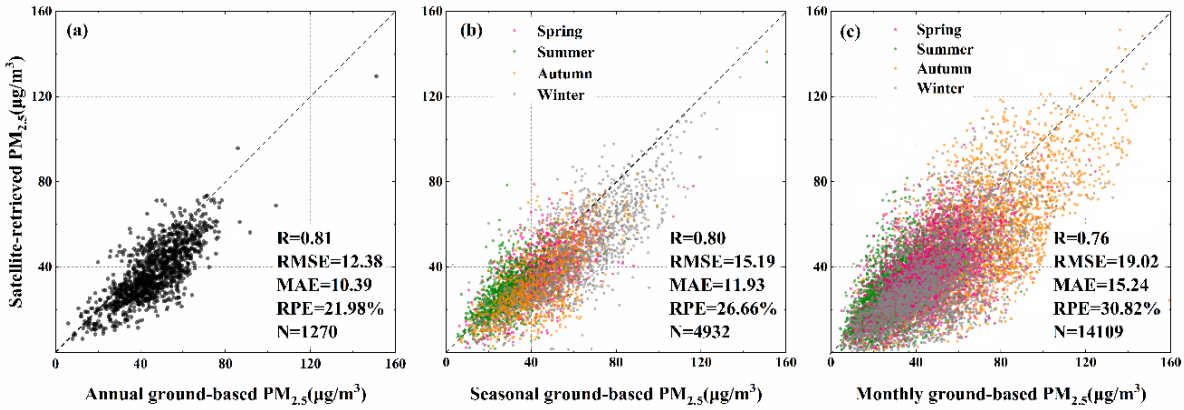

Figure 3.8 Validation of $PM_{2.5}$ retrievals without correction over China

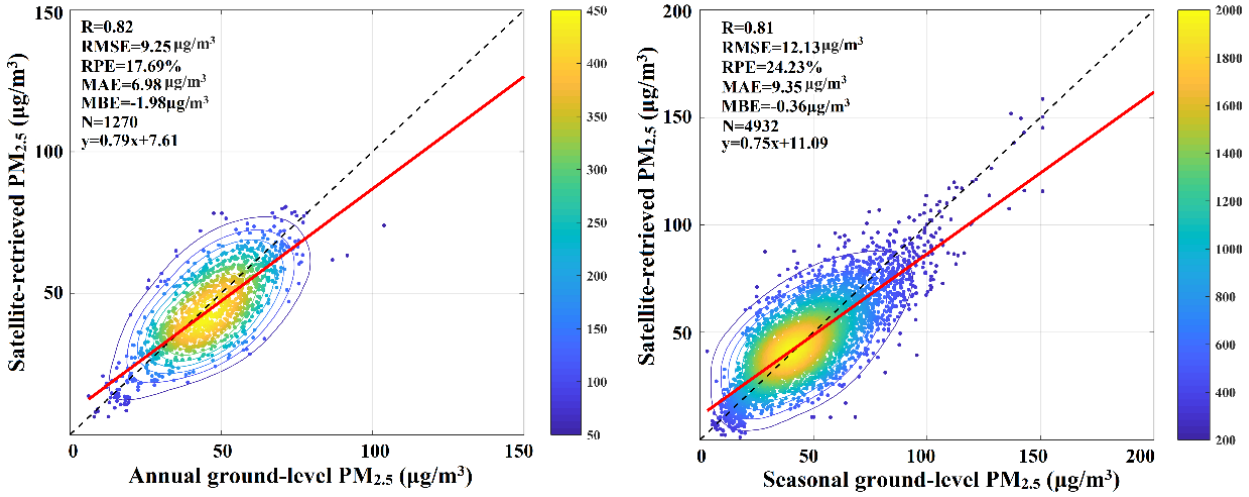

Figure 3.9 Validation of $PM_{2.5}$ retrievals over China at annual and seasonal scales

3.5 Discussion

An optical-mass conversion algorithm was established to quantify $PM_{2.5}$ concentrations using satellite-observed data. The particle diameters and $PM_{2.5}$ concentrations were estimated and validated over China. Our aerosol diameter results show that the mean particle size in eastern China was smaller than in other regions, which might be attributed to differences in topography, meteorology, land use, and population density, affecting the properties of emitted aerosols as well as their fate and transport. According to previous studies (Qian and Liu 2018; Wang et al. 2004), due to land use and topography in China, aerosol loading to the east of the Heihe-Tengchong line is high, which is likely attributed to human activity. Values in the west are relatively low, which might be influenced by natural sources (such as sand and dust). These findings are consistent with our size results. This observed pattern does show some seasonality, though 90% of pixels have diameters less than 1 μm throughout all seasons. Across the domain, particle sizes were generally larger in the spring and summer, and smaller in the autumn and winter. This seasonality may be attributed to variations in the sources, fate, and transport of fine particulate matter (Zhang et al. 2013).

A similar spatial pattern was also observed in mass concentration. The heavy pollution in the BTH region is likely attributable to unfavorable topography, regional transport and anthropogenic activities associated with urbanization and industrialization (such as fossil fuel consumption) (He and Huang 2018; Zheng et al. 2015a). The pollution in the SB region was likely due to relatively low elevations and stagnant air circulation (You et al. 2016) and the polluted air in the TD region was mainly attributed to dust and sand (Ma et al. 2014). In the PRD, $PM_{2.5}$ concentrations were predominantly rated "lightly polluted" or "good", though some coastal regions showed "excellent" levels, which could indicate an underestimation in coastal areas, where surface reflectance can be more challenging to characterize (Anderson et al. 2013). Temporally, the highest $PM_{2.5}$ concentrations occurred in winter while summer had the lowest concentrations. Heating-related emissions and adverse weather are two possible reasons for higher pollution in winter (He and Huang 2018; Ma et al. 2014). The $PM_{2.5}$ retrievals were validated at 1270 stations in China in more than 350 available days, with acceptable correlation between annual-mean retrieved and measured $PM_{2.5}$ concentrations. These results provide evidence to support the reliability of this conversion algorithm for retrieving ground $PM_{2.5}$ concentrations with an explicit mechanism.

Compared with other retrieval methods (Lin et al. 2015; Zhang and Li 2015), the AOD-$PM_{2.5}$ relationship in our study builds upon aerosol microphysical characteristics without introducing regional

fitting parameters, making it easier to apply across spatial and temporal domains. However, the performance of this method is affected by two main sources: input data and retrieval assumptions. Spatial heterogeneity affects the processes of data retrieval, gap-filling and interpolation, which could lead to random and systematic errors. Although MODIS AOD is one of the most widely used and well-validated products for $PM_{2.5}$ retrieval, biases remain because of the retrieval algorithm and cloud contamination. High aerosol loading might be misclassified into cloud, leading to missing values during periods of severe haze. Meanwhile, the input data might be also biased due to algorithm errors, interpolation errors and systematic errors. For example, the separation of MODIS retrieval algorithms over land and ocean may lead to inaccuracy over pixels containing land and ocean (Anderson et al. 2013). Consistent with the satellite transit time, the retrieved $PM_{2.5}$ in this study corresponds to values between 10:00am and 14:00pm instead of a daily average. This potential bias should be addressed prior to use as a daily average, for example, in health studies.

In addition to the uncertainty caused by input data, the retrieval method in our studies could also introduce errors. Although particle radius could be determined with the model, high precision was difficult to achieve with the limited ground-based measurements. Compared to the observed data acquired from AERONET, the relative error of particle radius in this study is approximately 7%; however, this needs to be further tested, especially in the regions where verification sites are limited. It is more problematic to adopt an empirical constant as the radius due to the spatiotemporal variance of aerosols. Therefore, future work should seek to address this using the micro-properties of aerosols from a mechanistic prospective at large scale. Furthermore, assumptions used in our study could also introduce bias. Previous studies have indicated that particle density and distribution vary in the columnar atmosphere (Liu et al. 2015a; Yan et al. 2017). The assumptions of constant values for ρ and σ_g and uniform vertical distribution can lead to an error of 18% and 16.6%, respectively (Li et al. 2016; Zhang and Li 2015). The total uncertainty of related to assumptions in our optical-mass conversion algorithm is approximately 29%. Additionally, there are several other factors regarded to be causally associated with $PM_{2.5}$ concentration and the mechanism of how these parameters impact observations was not fully understood, which offers a fertile field for study.

3.6 Conclusion

A satellite-based optical-mass conversion algorithm was established in this chapter to quantify $PM_{2.5}$ mass concentrations based on aerosol microphysical characteristics, which can simultaneously estimate particle size. The estimated particle radius was quantified against the available ground-based columnar

measurements, with RMSE = 0.11μm. The validation result shows that the ground-level radius is slightly larger than the corresponding columnar value on average, which is consistent with the findings that aerosol radius decreases slightly with altitude. The spatial distribution shows that particle diameters in eastern China are smaller than those in other regions, which might be due to differences in features such as topography, meteorology, land use and population density in China. Additionally, the estimated $PM_{2.5}$ concentrations were corrected and validated using ground measurements at annual and seasonal scales, with RMSE = 9.3 μg/m^3, MAE=7.0 μg/m^3, MBE=-2.0μg/m^3, RPE = 18% (N = 1270). The spatiotemporal distribution of satellite-retrieved $PM_{2.5}$ agrees with the in-situ data and findings from previous studies. Highly polluted periods are more likely to occur between Jan-Feb and Nov-Dec, while summertime has the lowest $PM_{2.5}$ concentrations. Spatially, the BTH regions experienced a higher $PM_{2.5}$ pollution compared with other major metropolitan areas. This approach builds on previous optical-mass studies by avoiding regional fitting and retrieving particle size. It can thus potentially fill an important gap in estimating exposure to ultrafine particles (which are thought to be more toxic, but lack large-scale, high-resolution measurements). Further work is needed to increase the accuracy of this method, which would benefit from the improvement of sensors and algorithms.

Chapter 4

Size-Differentiated Patterns of Exposure to Submicron Particulate Matter Across Regions and Seasons in China

To motivate the understanding of the impact of particle size on human health, in this chapter, we present the spatiotemporal distributions and population exposure to ambient particle size and mass concentration of $PM_{2.5}$ at the national level in China using a satellite-based theoretical optical-mass relationship. We find that most of the Chinese population was exposed to $PM_{2.5}$ in the sub-micrometer range. Less than 1% lived in regions where concentrations met the annual WHO guideline (10 $\mu g/m^3$) and annual-mean particle effective radii above 0.7μm (i.e. PM_1) in 2017. High mass concentrations and small particle sizes were observed in the east of China where has high GDP and population density. The study reveals the pattern of size-resolved $PM_{2.5}$ exposure and indicates the potential of remote sensing techniques for population-scale $PM_{2.5}$ estimation, including concentrations and sizes. The limitations of this work, resulting from the dearth of large-size measurements and the uncertainty of input data, are discussed to facilitate further improvements on the effect of particles on PM2.5 attributable health risk.

This chapter is structured as follows. Section 4.1 states the background and motivation of the study. Sections 4.2 introduces the adopted datasets and the estimation method. Section 4.3 demonstrates the population exposures to $PM_{2.5}$ mass and particle radius in China. Section 4.4 analyzes the possible attribution of $PM_{2.5}$ mass and size. Section 4.5 discusses the uncertainty sources in this chapter. Section 4.6 concludes the main findings.

4.1 Introduction

Exposure to ambient atmospheric pollutants, especially fine particulate matter ($PM_{2.5}$), has been shown to significantly increase the risk of mortality from cardiovascular and respiratory illnesses (Pope et al. 2018; Sacks et al. 2011). China has suffered from severe $PM_{2.5}$ pollution with its rapid economic development and industrialization. In 2017, approximately 0.85 million premature deaths and 19.8 million disability-adjusted life-years (DALYs) lost were reported to be attributable to ambient $PM_{2.5}$ exposure in China, accounting for 29% of the $PM_{2.5}$-related premature deaths and 24% of the DALYs worldwide (Cohen et al. 2017). While epidemiologic relationships have been established for $PM_{2.5}$ mass concentrations and a variety of health endpoints, other particulate characteristics, like composition and

size, may be relevant in informing such relationships, e.g., via effect modification, or in identifying new ones. Size-resolved particular matter observations are thus pertinent for exposure assessment. Here, we aim to provide national population-scale size-resolved exposures to $PM_{2.5}$.

Using various exposure methods, previous toxicological and epidemiological studies found that particles with different size ranges have independent effects on human health (Esposito et al. 2012; Gerlofs-Nijland et al. 2009). Small particles can penetrate into the airways and alveoli, and finally into the bloodstream and cardiovascular system, leading to inflammation and oxidative stress (Delfino et al. 2005; Mills et al. 2009). Smaller particles may have higher toxicity since the relatively large number and surface area of small particles may increase their risk of absorbing toxic substances (Hoek et al. 2009; Ostro et al. 2015; Samoli et al. 2016).

Despite such work indicating the significance of size, the scale of current size-resolved exposure and epidemiological studies is limited in terms of the exposed population, as well as spatial and temporal domains. This is due primarily to typical exposure measurement techniques, including fixed ground-based stations (Chen et al. 2017; Hu et al. 2018) and personal portable monitors (Gulliver and Briggs 2007; Pacitto et al. 2018; Yu et al. 2012). Personal exposure monitors provide crucial individual-level detail and insights. Nonetheless, supplementary population-level exposures can inform individual-level studies, and may offer their own unique insights given the nature of environmental exposures (Pekkanen and Pearce 2001). Population-scale studies that involve some size-resolution in the fine fraction are primarily limited to station-based measurements, the spatial continuity and coverage of which are limited due to their high costs of station construction, operation and maintenance (Kumar et al. 2015). Wichmann *et al*. (2000) used measurements from a single monitoring station to assess particle exposure in Erfurt, Germany, with a population of approximately 200,000 people, indicating that exposure to ambient concentrations of fine and ultrafine particles had comparable effects. (Lin et al. 2016) found the excess risk of cardiovascular mortality with PM_1 was 6.48% (95% CI: 2.10%, 11.06%), higher than those associated with PM_{10} and $PM_{2.5}$ reported in their study, demonstrating that PM_1 might be an important characteristic of particulate matter pollution attributable to cardiovascular mortality in Guangzhou, China. Two monitoring stations were used in this study.

The distribution of ambient particles shows variability, reflecting regional variations in aerosol emissions, transport and physicochemical processes (Pinto et al. 2004; Wang et al. 2013; Yang et al. 2018). Chen *et al.* (2018) showed the station-based spatial distributions of PM_1 and $PM_{2.5}$ concentrations and the seasonal variations of the $PM_1/PM_{2.5}$ ratio the provincial level, demonstrating

the spatial and temporal variability of size-fractioned particulate matter particles. Thus, exposure estimates based on in-situ measurements in a sparse monitoring network cannot fully represent the average exposure of the whole city population, especially, perhaps, for ultrafine particles (Pekkanen and Kulmala 2004), potentially limiting their use for population-based studies. Kodros et al. (2018, 2016) indicated that particle size measurements in polluted areas, such as India and China, are especially limited, leading to uncertainties.

Many techniques are used to address the limited spatial coverage of fixed site measurements of particulate matter exposure based on multiple data sources. Ground-based measurements may be used to validate alternative estimates from numerical simulation and empirical models (Knibbs et al. 2018; Ma et al. 2014; Xiao et al. 2018). These approaches differ in their current level of application to size-resolved exposure estimates. Numerical chemical transport models offer an approach to obtain aerosol components and behavior with a relatively high spatiotemporal resolution and coverage (Brauer et al. 2012; Saari et al. 2019). Further, they are capable of providing size-resolved exposures, as in Kodros et al., (2018); however, the application thereof remains limited as the use of size-resolved aerosol schemes greatly increases computational cost of simulations (Kodros and Pierce 2017). Statistical models are beginning to offer size-related information through the advent of novel and relatively low-cost particle-counting sensors. While such sensors do not provide size-resolved mass concentrations, particle number concentration can be related to the mass distributions. Recent work, reviewed and advanced in Saha *et al.*, (2019), employed short-term fixed-site measurements to develop land use regression models of particle number concentration – a proxy for ultrafine exposure. Satellite remote sensing techniques have been applied to obtain concentrations of air pollutants with relatively with high spatial coverage (van Donkelaar et al. 2016; Yan et al. 2017). Zhang and Li (2015) established a theoretical relationship between fine particulate mass and satellite measurement based on aerosol microphysical behaviors. However, these methods have less commonly been applied to derive particle size (Hilboll et al. 2013; Larkin et al. 2017). Aside from the Angstrom Exponent (AE), which is inversely related to aerosol size (Qi et al. 2013; Wang et al. 2013), there is little information available on particle size, especially for submicron exposures at a population scale.

In this study, we sought to provide national population-scale size-resolved estimates of $PM_{2.5}$ mass concentration. To achieve this, we combined aerosol microphysical characteristics with satellite optical measurements to estimate the ground-level particle effective radius of $PM_{2.5}$. We applied this to examine the geographic variability and population exposure of the $PM_{2.5}$ size-resolved mass

concentrations over China in 2017. This study reveals the extent of $PM_{2.5}$ exposure by particle size in the sub-micrometer range, identifies the importance of additional size-resolved measurements, and motivates further research to examine the effects of particle size on health outcomes.

4.2 Materials and Methods

4.2.1 Satellite-retrieved $PM_{2.5}$ Estimation

Ground-level $PM_{2.5}$ concentrations were estimated based on satellite and meteorological data using a Geographically Weighted Regression (GWR) model which were widely adopted for $PM_{2.5}$ concentrations retrievals. Prior to GWR modelling, we corrected satellite-observed columnar aerosol optical depth (AOD) at the wavelength of 550nm into ground-level extinction (b_{ext}) based on an assumption that the majority of atmospheric aerosols evenly suspend in the planetary boundary layer (PBL) due to the active mixing (Kaufman et al. 2003). Fine mode AOD was adopted based on an look-up table–spectral deconvolution algorithm, which was found to be closely related to $PM_{2.5}$ (Yan et al. 2017; Zhang and Li 2015). Hygroscopic growth functions were employed since aerosol hygroscopic characteristics affect extinction by changing the particle size. The correction formula is given below:

$$b_{ext,dry} = \frac{\eta b_{ext}}{f(RH)} = \frac{\eta\tau}{Hf(RH)} \quad (4\text{-}1)$$

where $b_{ext,dry}$ refers to extinction coefficient of fine particles under dry conditions; η refers to fine mode fraction; τ refers to satellite-derived AOD at 550nm; H refers to the height of PBL; f(RH) refers to a hygroscopic growth function with independent variables of relative humidity (RH), which are calculated based on the previous studies (Chen et al. 2014a, 2015; Liu et al. 2019a; Yan et al. 2017).

In addition to aerosol extinction, we include meteorological parameters expected to be associated the generation, accumulation, and removal of aerosols, including air temperature (T) (Day and Pandis, 2011; Liu et al ., 2007), surface wind speed (WS) (Zhou et al., 2015), horizontal visibility (V) (Xiao et al., 2018; You et al., 2016b) and elevation (DEM) (Wang et al., 2018). These variables have been employed previously in studies with acceptable performance (He and Huang, 2018b; Kloog et al., 2012; Liu et al., 2009; Ma et al., 2016, 2014). We considered and excluded additional variables, such as pressure, that did not independently improve performance (details in Appendix A-3). We employ these variables to estimate $PM_{2.5}$ across China using the GWR model, according to the following model structure:

$$PM_{2.5(i,j)} = \beta_{0(i,j)} + \beta_{b_{ext,dry\,(i,j)}} b_{ext,dry\,(i,j)} + \beta_{T(i,j)} T_{(i,j)} + \beta_{WS(i,j)} WS_{(i,j)} + \beta_{V(i,j)} V_{(i,j)} +$$

$\beta_{DEM(i,j)}DEM_{(i,j)} + \varepsilon_{(i,j)}$ (4-2)

where $PM_{2.5(i,j)}$ is the ground-level $PM_{2.5}$ concentration at location (i, j); β_0 is the intercept; β with different subscripts denote the slope of corresponding variables. $\varepsilon_{(i,j)}$ is the error term at location (i,j). Gaussian distance decay functions were adopted to determine the weights. Considering spatial autocorrelation, 10-fold block cross validation (CV) was adopted to evaluate the model performance (Roberts et al. 2017). Four metrics, including the determination coefficient (R^2), root mean square error (RMSE), mean absolute error (MAE) and mean bias error (MBE), were used to compare the retrieved and measured values. The variance inflation factor (VIF) was employed to measure the collinearity of the adopted variables (Table A3). It was less than 3 for all variables, indicating low collinearity.

The detailed description of adopted parameters in above formulas is shown in Table 4.1. All independent data were masked before resampling to 3 km using the cubic convolution algorithm and were unified with respect to the coordinate system (WGS84) and data format, following the geophysical coverage of China and spatial resolution of MODIS AOD.

Table 4.1 Detailed data description

Data (Unit)	Spatial resolution	Descriptive statistics of collocated data		
		Min	Max	Mean
$PM_{2.5}$ (μg/m^3)	---	1.00	736.25	45.55
AOD (Unitless)	3km; 10km	0.03	3.86	0.47
T (K)	0.25˚	260.81	309.67	289.04
WS (m/s)	0.25˚	0.16	15.82	3.49
RH (%)	0.25˚	9.04	96.83	56.93
PBLH (m)	0.25˚	25.90	6328.97	1837.02
V (km)	---	0.26	49.99	9.45
DEM (m)	1km	-13.46	4553.22	370.51

Note: Ground-level $PM_{2.5}$ concentrations were obtained from China National Environment Monitoring Center; AOD images obtained from NASA Atmosphere Archive and Distribution System; T, WS, RH, and PBLH were obtained from NCEP GDAS/FNL 0.25 Degree Global Tropospheric Analyses and Forecast Grids; V was obtained from NCEP ADP Global Surface Observational Weather Data; DEM was obtained from Resources and Environmental Science Data Center.

4.2.2 Particle Size Calculation

The aerosol radius was calculated with ground-level mass concentrations based on optical-mass theoretical relationships (Liu et al. 2019b). We assumed aerosol particles were homogeneous spheres to statistically describe an ensemble of particles due to the aerosol complexity in terms of composition

and geometry (Holben et al. 1998; Nakajima et al. 1996). The lognormal distribution was adopted to express the particle size distribution, which can be described by two parameters: geometric mean radius (r_g) and geometric standard deviation (σ_g). Since aerosol extinction is proportional to r^2, we used the effective particle radius (r_e), a weighted mean of size distribution, to represent the particle size according to the rule of lognormal distribution.

$$r_e = \frac{\int_0^\infty r^3 n(r)\mathrm{d}r}{\int_0^\infty r^2 n(r)\mathrm{d}r} = r_g \exp(\frac{5\ln^2\sigma_g}{2}) \tag{4-3}$$

where $n(r)$ is the lognormal size distribution of accumulation mode aerosol; σ_g was set at 2, which refers to the general range of different fine particles (Reid et al. 2003; Steele et al. 2006).

Consequently, the columnar particle mass concentration (M) and $\mathrm{b_{ext,dry}}$ can physically be defined and deduced:

$$\mathrm{M} = \frac{4}{3}\pi\rho\mathrm{H}\int \mathrm{r}^3\mathrm{n(r)dr} = \frac{4}{3}\pi\rho\mathrm{H}r_g{}^3 \exp\left(\frac{9\ln^2\sigma_g}{2}\right) \tag{4-4}$$

$$\mathrm{b_{ext,dry}} = \frac{\eta}{f(RH)}\int_0^\infty \mathrm{Q_{ext}}\pi\mathrm{r}^2\mathrm{n(r)\,dr} \tag{4-5}$$

where ρ is the mean bulk density of atmospheric particles, with a constant value of 1.5 g/cm^3 (Clarisse et al. 2010; Li et al. 2016), $\mathrm{Q_{ext}}$ is the extinction efficiency, which is related to visibility (Koschmieder, 1924),

$$\mathrm{Q_{ext}} = \frac{3.912/\mathrm{V}}{\pi(r_e)^2\exp(-3\ln^2\sigma_g)} \tag{4-6}$$

Equating with Eqs. (1), (3) – (6) yields,

$$\mathrm{r}_e = (\frac{3\mathrm{M}(3.912/\mathrm{V})}{4\pi\rho\tau\exp(-3\ln^2\sigma_\mathrm{g})})^{1/3} \tag{4-7}$$

In Eq. (4-7), M was calculated based on the GWR model in Section 2.1; τ and V are spatial variables acquired from satellite and re-analysis datasets. The ρ and σ_g were treated as constants, the effect of which is examined in Section 4.5. Since large-scale ground-level radius measurements are limited, we validated the radius estimates against the available columnar effective radius retrievals and the Angstrom Exponent (AE) data (using wavelengths 0.44 and 0.87 μm) provided by eight Aerosol Robotic Network (AERONET) stations. The spatial pattern of estimated particle radius was visually compared to MODIS AE products for each season.

4.2.3 Population Data

Gridded population data with a spatial resolution of 1km were obtained for 2015 from "Resource and

Environmental Science Data Center of the Chinese Academy of Sciences (RESDC) (http://www.resdc.cn/)". This dataset provided 1km gridded population using multi-factor weighting based on county-level demographic data, considering land use type, nighttime light intensity and residential density (Xu 2017). The annual population in 2017 in each province was also acquired from the "Chinese National Bureau of Statistics (http://www.stats.gov.cn/tjsj/ndsj/)" to project the gridded 2015 population to 2017. To project the gridded data, the ratio of the gridded population to the whole population in each province in 2015 was first calculated. The gridded population in 2017 was then obtained by multiplying this ratio in each province by the whole population in the corresponding province in 2017. The final gridded population was resampled to 3km to match the spatial resolution of estimated $PM_{2.5}$ concentrations and sizes.

4.3 Results

4.3.1 Ground-Level $PM_{2.5}$ Concentration Estimation

As mentioned in Section 4.2.1, the GWR model was established using ground-based $PM_{2.5}$ measurements with a total of 176,385 available samples. Table 4.2 shows the results of model fitting and cross validation based on the GWR model. The model fitting R^2 between the estimated and measured $PM_{2.5}$ mass concentration is 0.82, with RMSE of 15.7μg/m^3 and MAE of 10.1 μg/m^3. A negative MBE suggests $PM_{2.5}$ concentrations were underestimated by -6.6μg/m^3. Compared to the model fitting results, the CV R^2 (0.80) decreases by only 0.04 and the CV RMSE increases by 2.3μg/m^3, indicating that there is no substantial overfitting in the model. Both overall R^2 and CV R^2 are higher than 0.80, showing that the accuracy of $PM_{2.5}$ estimation results are acceptable. In addition, as shown in Figure 4.1(a), the spatial pattern of annual mean $PM_{2.5}$ estimation appears to be visually consistent with that of ground observations in 2017. The concentrations in eastern China are generally higher than those in the west, except for the Taklamakan Desert. As designated by Chinese National Bureau of Statistics (http://www.stats.gov.cn/tjsj/ndsj/2017/indexeh.htm), we divided the entire study area into four regions (East, West, Northeast and Centre) based on their economic development (Figure 4.1(b)). The East is the most developed region in China, contributing 52.6% of overall GDP, while the Northeast has the smallest GDP, accounting for 6% of the total. The highest annual-mean growth rates of GDP and industrial added value occurred in the Centre region, with respective values of 10.8 % and 12.5%, respectively (2006-2017).

Table 4.2 Validation of daily $PM_{2.5}$ estimates

	R^2	RMSE ($\mu g/m^3$)	MAE ($\mu g/m^3$)	MBE ($\mu g/m^3$)	N	Equations
Model-fitting	0.82	16	10	-6.6	176,385	y=0.81x+14.32
CV	0.80	18	12	-6.0	176,385	y=0.80x+15.89

Note: N: sample numbers; R^2: determination coefficient; RMSE: root-mean-square error; MAE: mean absolute error; MBE: mean bias error.

Results in Figure 4.1 show that the highest annual-mean $PM_{2.5}$ levels were observed in the Centre, with a mean concentration of 54 $\mu g/m^3$, followed by the West, the East, and the Northeast region. Although the East had the second lowest $PM_{2.5}$ levels, hotspots in the Beijing-Tianjin-Hebei (BTH) metropolitan region experienced high $PM_{2.5}$ exposures, with concentrations exceeding 55$\mu g/m^3$. Elevated $PM_{2.5}$ concentrations in the West were located in the Tarim Basin (Taklamakan Desert), the Guanzhong Plain, and the Sichuan Basin. The seasonal variations of $PM_{2.5}$ concentrations are shown in Figure 4.2, indicating that winter was the most polluted season in 2017, with a mean value of 61$\mu g/m^3$. Following van Donkelaar et al. (2016), exposed population counts and cumulative distributions of $PM_{2.5}$ concentrations by population for different regions are shown in Figure 4.3. The national population-weighted average (PWA) of ambient $PM_{2.5}$ is estimated to have been 52$\mu g/m^3$ in 2017. The highest PWA concentration was observed in the Centre (61$\mu g/m^3$), while the Northeast had the lowest value (38$\mu g/m^3$). The standard deviation (STD) of PWA in these two regions was below 20$\mu g/m^3$, indicating a mean separation of at least one STD between them. The PWA concentrations in the West (47$\mu g/m^3$) were lower than those in the East (54$\mu g/m^3$), although this order is reversed for mass concentrations. The West and East had significantly higher STDs than the other regions, with the respective values of 96$\mu g/m^3$ and 40$\mu g/m^3$, indicating highly variable exposures.

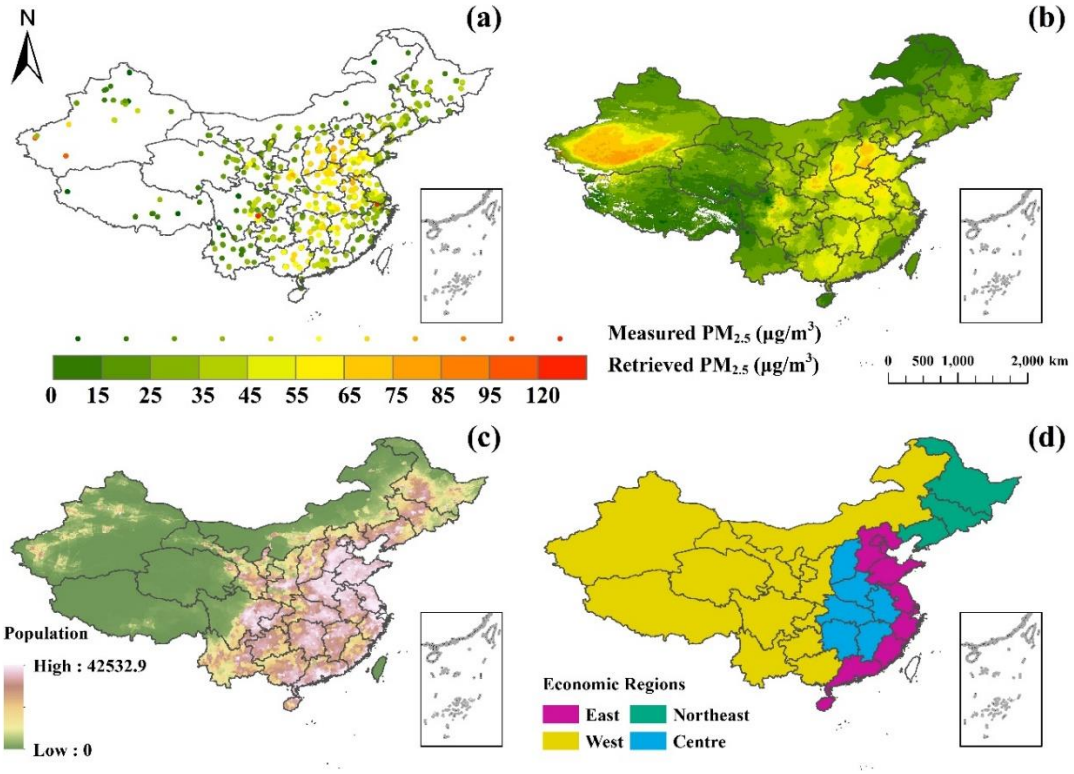

Figure 4.1 Spatial patterns of (a) ground-based $PM_{2.5}$ concentrations (b) satellite-estimated $PM_{2.5}$ concentrations (c) population (d) economic regions in 2017 (Note that the following analysis did not take into account Taiwan because of the lack of population data)

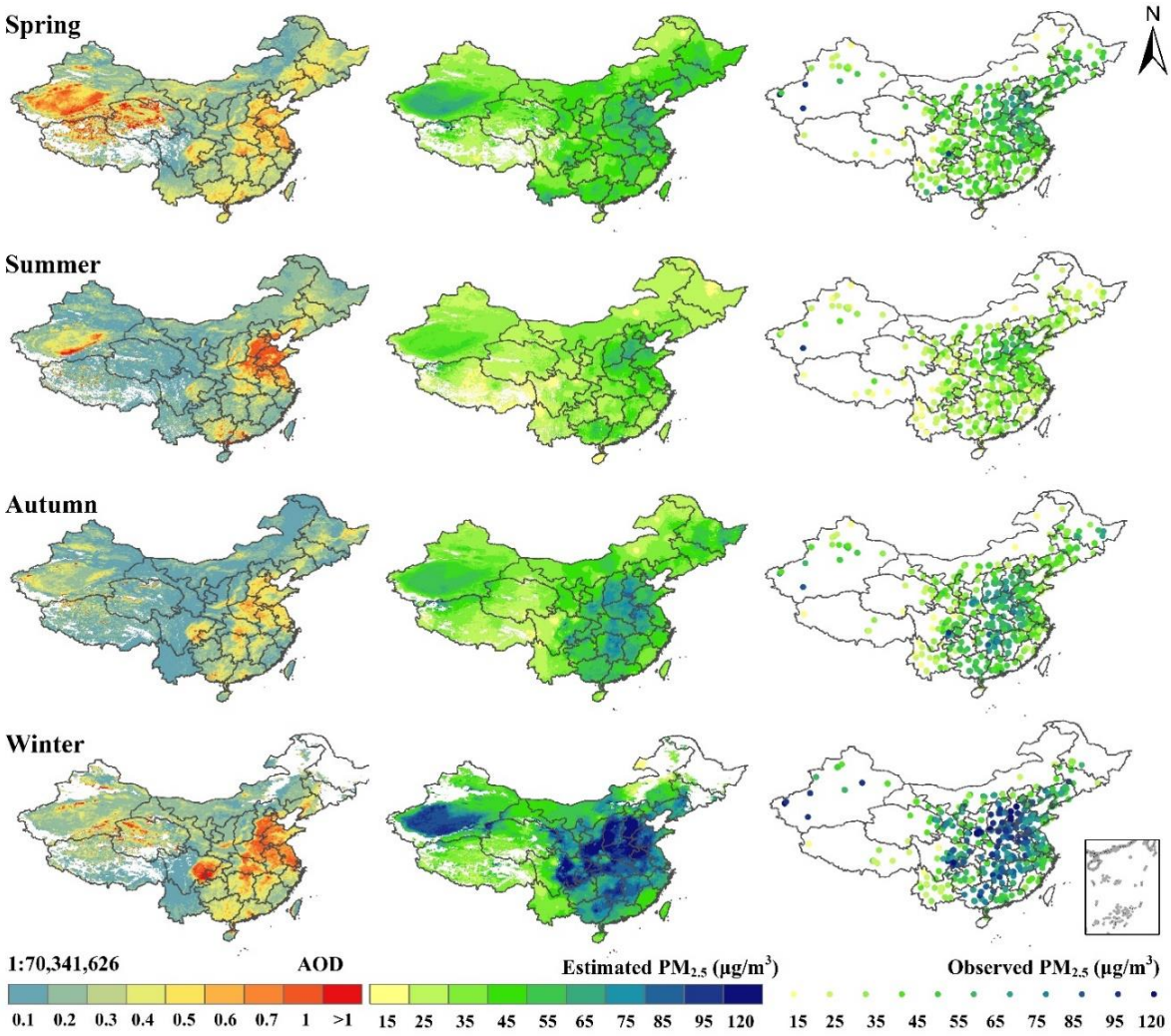

Figure 4.2 Spatial patterns of seasonal mean MODIS AOD (left), estimated $PM_{2.5}$ concentration (middle) and observed $PM_{2.5}$ concentration (right)

The cumulative distribution of population exposure to mass concentrations was also explored to describe the percentage of population experiencing high $PM_{2.5}$ levels (Figure 4.3b). The results show 12% of the Chinese population living where concentrations meet the China national ambient air quality standards (GB 3095-2012) (35 μg/m^3) and less than 20,000 people living in regions with concentrations lower than 10 μg/m^3 (WHO guideline) in 2017. Regionally, 1% of the Northeast population was exposed to $PM_{2.5}$ concentrations exceeding 50μg/m^3, compared to 90% of the Centre population. Typical ambient concentrations in the East and West regions range from 20-80μg/m^3, while a larger percentage of the population in the East (56%) experienced $PM_{2.5}$ concentrations higher than 50μg/m^3

than that in the West (36%), although the mean concentrations in the East are slightly lower than those in the West.

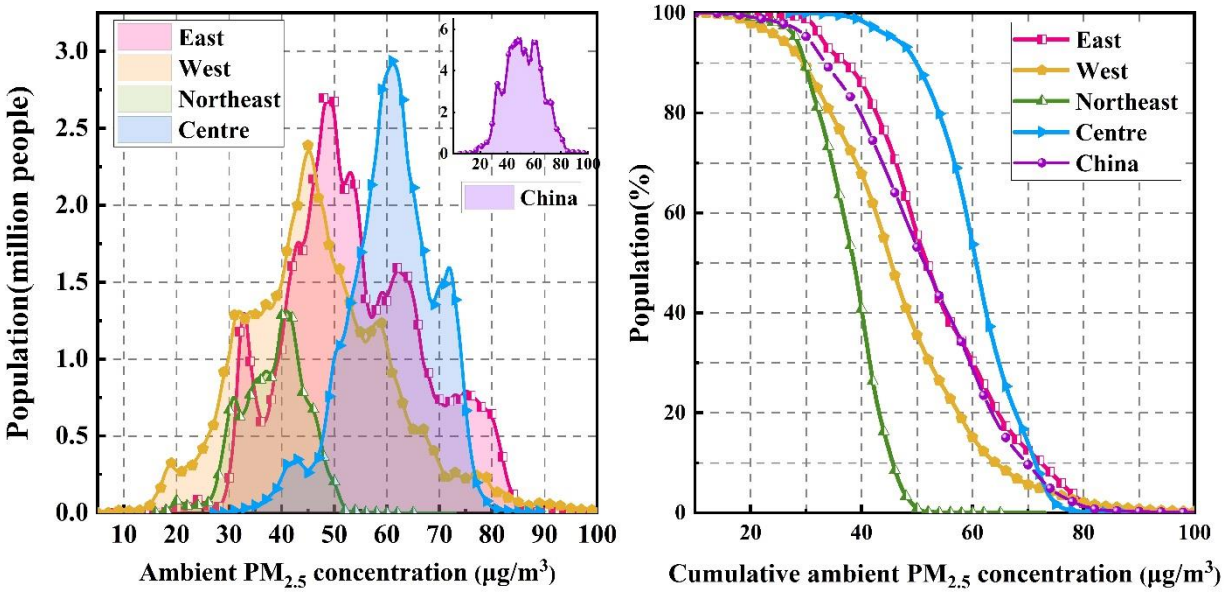

Figure 4.3 Distribution of 2017 $PM_{2.5}$ concentrations by population for four economic regions and China

4.3.2 Ground-Level Particle Radius Estimation

The atmospheric aerosols over China were dominated by $PM_{2.5}$ particles with radius less than 1.0μm in 2017. The estimated particle radius was calculated as described in Section 4.2.2, and validated against the available AERONET columnar radius measurements, with R=0.66 (Figure 4.4a). Both RMSE and MAE were less than 0.2μm, enabling diverse particle sizes to be distinguished. A positive MBE indicates that the ground-level estimated radius was slightly larger than the columnar AERONET retrievals, which could be due to a slight decrease in radius with altitude (Baars et al. 2012). Given that radius measurements are limited, we also plotted our radius estimates against the AERONET AE values in Figure 4.4b. The result shows that the estimated radius decreased with increasing AE and the rate of decline is larger at lower AE values (inset in Figure 4.4b). These findings are consistent with previous studies showing that AE is generally inversely associated with particle size (Giannakaki et al. 2016; Müller et al. 2011; Schuster et al. 2006).

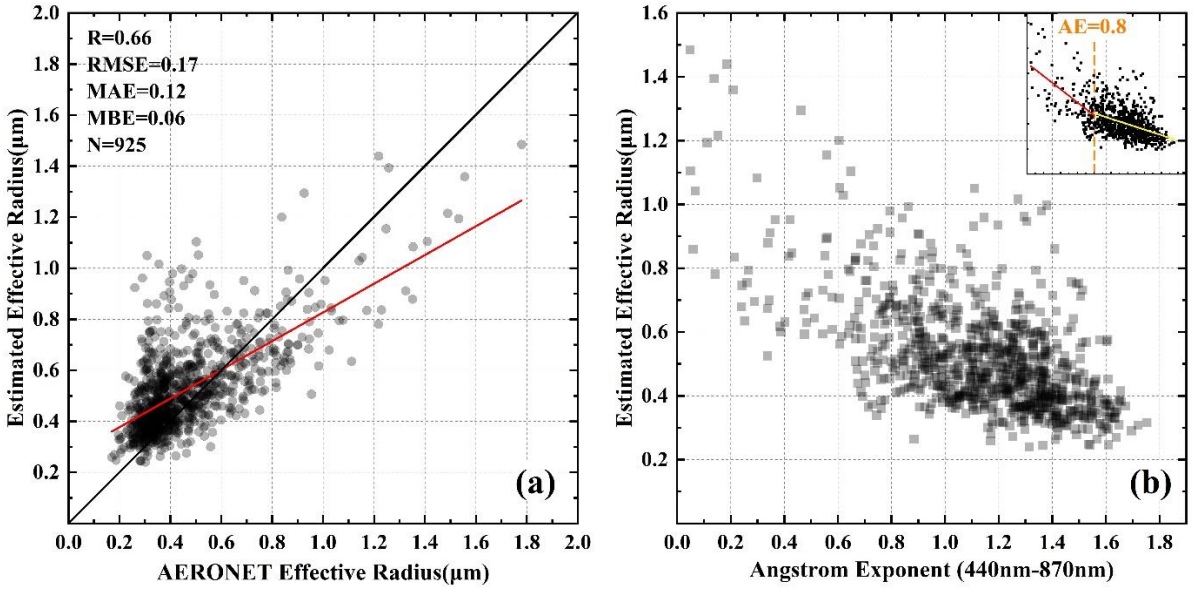

Figure 4.4 Validation of estimated effective radius against AERONET (a) radius retrievals and (b) AE values

The spatial patterns of estimated particle radius are shown for annual and seasonal scales in Figure 4.5. The mean particle size is larger in the West than in the Centre or East. The division coincides with the imaginary line (Heihe-Tengchong) dividing the territory of China into western and eastern parts according to population density (Hu 1935). This result indicates that the population in eastern China is exposed to $PM_{2.5}$ pollution with a smaller mean particle size. The Tarim Basin (where the Taklamakan Desert is located) has the largest particle size in China, especially in the spring and summer. $PM_{2.5}$ with smaller particle size are more likely to occur in the spring and summer in eastern China, while there is less spatial variation in autumn and winter. The seasonal variations and spatial patterns of the estimated particle radius are visually consistent with those of MODIS AE data.

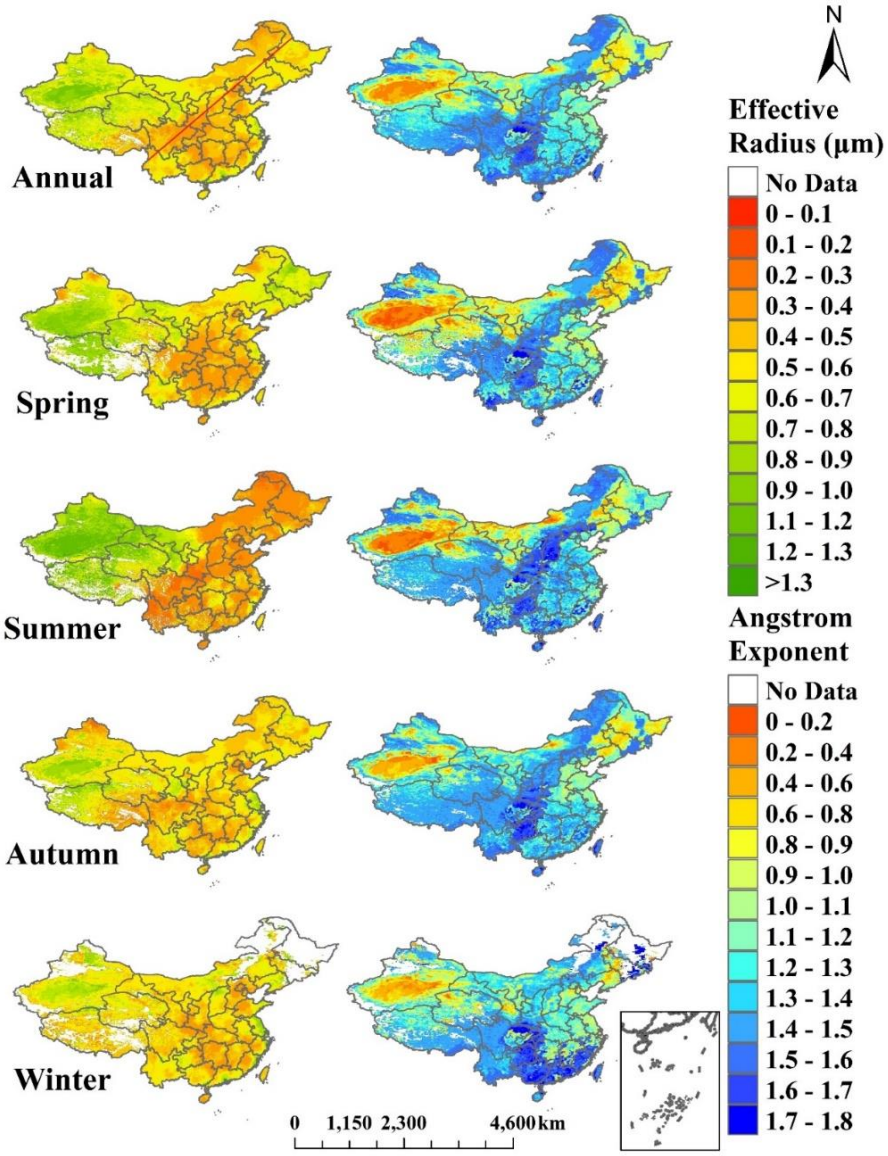

Figure 4.5 Spatial patterns of estimated particle effective radius (left) and MODIS Angstrom Exponent (right)

Figure 4.6 presents the distribution of annual-mean particle effective radius by population and region. Nationally, more than 99% of the Chinese population lived in areas with effective particle radius less than 0.7μm (i.e. aerodynamic diameters lower than 1.0μm under the assumptions in this study) in 2017. The PWA effective radius of $PM_{2.5}$ in China was estimated to be 0.5μm, with STD of 0.5μm. This national mean of Re=0.5μm was used to compare exposures across the different regions. Figure 4.6 shows that 98% of the Centre's population was exposed to particles with annual-mean radius below

0.5μm, compared to 85% of the Northeast. The Centre was consistently exposed to small particles, with PWA radius of 0.4μm. Although Figure 4.5 shows the West had the largest particles, Figure 4.6 shows that most of its population was exposed to relatively smaller ones, with PWA radius of 0.5μm (rounded to the nearest tenth of a micron).

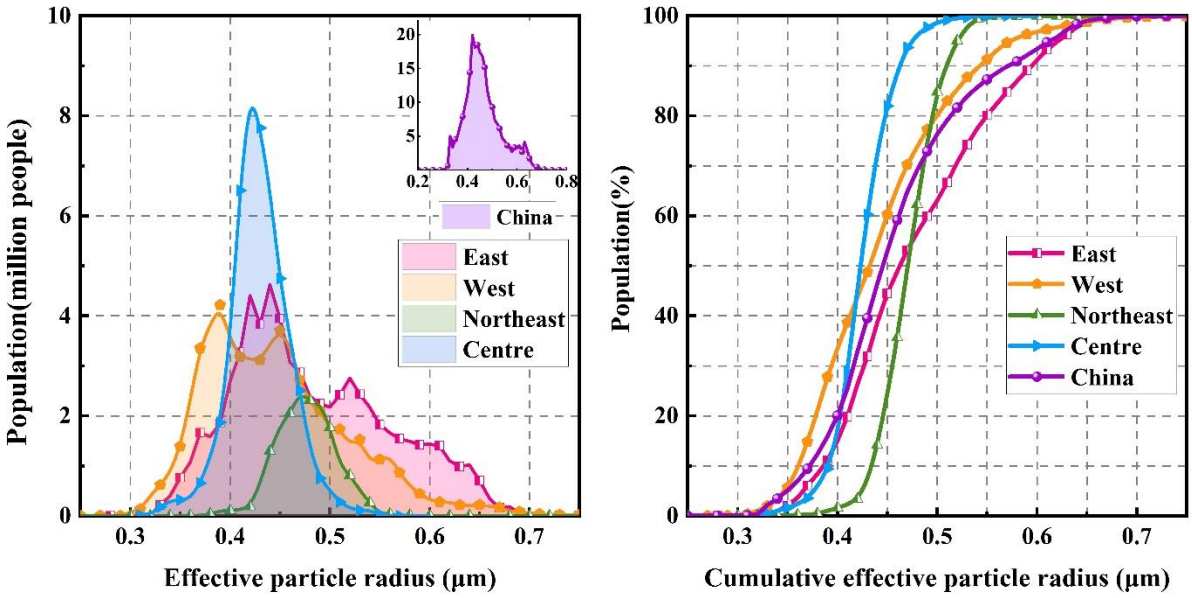

Figure 4.6 Distribution of annual-mean $PM_{2.5}$ effective radius estimation for four economic regions and China

The seasonality of particle size can be observed in Figure 4.7. The biggest difference in the median radius between the four regions occurred in springtime. Half of the Centre population in spring was exposed to $PM_{2.5}$ with radius less than 0.4μm, while half of the Northeast population was exposed to larger particles, with median radius of 0.5μm. Only 1% of the Centre population was exposed to particles larger than 0.5μm in the spring, compared to 84% of the Northeast. Summer is the season with the highest national exposures (86%) to a mean radius less than 0.5μm. The West shows the least seasonal variation in exposures to a mean less than 0.5μm (76%-81%). A relatively large proportion of the East population (42% in autumn and 40% in winter) are exposed to $PM_{2.5}$ (Re>0.5μm), likely due to high population density in the coastal region. The results suggest that population in the Centre region was exposed to not only the highest $PM_{2.5}$ concentration but also the smallest particle size.

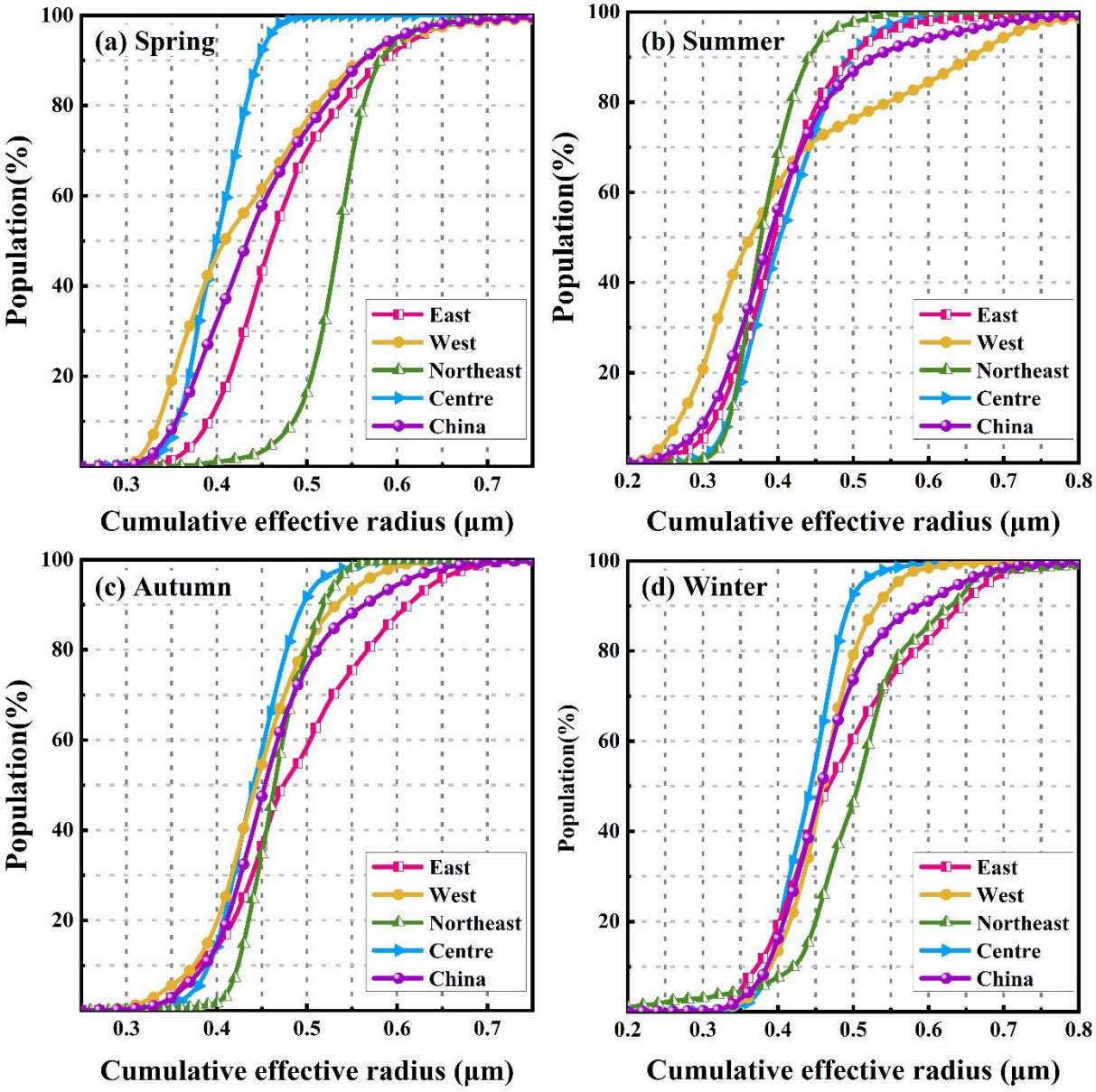

Figure 4.7 Distribution of seasonal-mean $PM_{2.5}$ effective radius estimation for four economic regions and China in (a) Spring (b) Summer (c) Autumn and (d) Winter

4.4 Discussion

Previous studies have shown the potential for particle size to affect outcomes of PM exposure, indicating that smaller sizes may have greater effects on human health (De Haar et al. 2006; Franck et al. 2011). Size-resolved exposures needed to support epidemiologic studies into this effect, however,

are limited by a lack of observations, especially at population scales. Here, we quantified $PM_{2.5}$ concentrations using a GWR model and estimated effective particle radius based on optical-mass theoretical relationships for China in 2017 across regions and seasons.

The national, annual-mean $PM_{2.5}$ mass concentration was estimated to be 46 $\mu g/m^3$. The highest mass concentrations of $PM_{2.5}$ were observed in central and eastern China (east of Heihe-Tengchong population line). These high concentrations were most prevalent in industrialized urban agglomerations, such as the North China Plain (the BTH region), Hubei and Hunan provinces. Higher concentrations were also found to cross into Shanxi and Shaanxi province, areas with abundant coal-fired facilities and coal production. This is consistent with previous attribution studies suggesting that the high $PM_{2.5}$ concentration in these regions is attributable to anthropogenic activities associated with rapid economic development and industrialization, such as fossil fuel consumption (Zhang et al. 2015a, 2013; Zheng et al. 2015a). The hotspot in the Sichuan Basin is related to the unfavorable topography encouraging stagnation in this low-lying area surrounded by mountains (You et al. 2016).

In the fine fraction ($PM_{2.5}$), we observed a range of annual mean effective particle radii from 0.3μm to 1.8μm across China in 2017. On a national, annual scale, we found a mean particle effective radius of 0.5 μm with a STD of 0.5 μm. This is consistent with Wichmann et al. (2000), finding that 78% (14%) of $PM_{2.5}$ mass was found in the diameter range of 0.1 to 0.5μm (0.5 to 1.0μm) in an urban area in Germany. The largest mean effective radii of $PM_{2.5}$ were found in the West. Mean particle radius across the Tarim Basin was much larger than in other areas, ranging from 0.6μm to 1.4μm. This finding is expected given the dust and sand in the Taklamakan Desert, and is in line with studies of $PM_{2.5}$ mass and size in this region (Ma et al. 2014; Shao and Mao 2016). Combining the seasonal spatial patterns of AOD and particle size, we found that high values of both AOD particle radius over the Taklamakan Desert are more prevalent in spring, which is attributed to the frequent dust events during spring (Yu et al. 2015; Zhao 2003). It is interesting to note that large size values were also observed in summer here. This appears to be supported by (Meng et al. 2019), reporting that summer has the lowest ratios of $PM_{2.5}/PM_{10}$, PM_1/PM_{10}, and $PM_1/PM_{2.5}$. Due to a dearth of studies of seasonal patterns of $PM_{2.5}$ composition in this region, however, we can only infer that this observed seasonality could be related to the sources, fate and transport of $PM_{2.5}$, and potential seasonal bias in the input data. Additionally, the Northeast region also experienced relatively high $PM_{2.5}$ concentrations with large particle radii in spring, which has been related to sand and dust storms caused by Siberian and Mongolian cyclones from northern Asia, indicating that the spatial pattern of $PM_{2.5}$ concentrations was also affected by aerosol regional transport (Qian et al. 2004; Wang et al. 2011).

4.5 Sources of Uncertainty

This study attempts to utilize large-scale measurements to explore the spatial variation and population exposure to ambient size-resolved $PM_{2.5}$ exposure. Given the aims of this work, several assumptions have been proposed to simplify the estimation method, leading to uncertainty. The assumption that spherical aerosols were uniformly distributed in the PBL can introduce an error of 16% in aerosol extinction, especially when additional pollution layers above the PBL are present due to emissions and long-distance transport of air pollutants (Li et al. 2016). While we assumed that the physiochemical and optical properties of aerosols are independent of size distribution, which enabled the aerosol hygroscopic properties to be simplified by growth functions, previous studies reported minor errors from this assumption (Li et al. 2016; Zieger et al. 2014). In addition to the above theoretical assumptions, empirical assumptions (such as σ_g and ρ) can also bring errors. Two aerosol properties used in the size estimation were assumed constant, including ρ and σ_g used to define the lognormal distribution. According to previous studies (Gao et al. 2007; Hand and Kreidenweis 2002; Hänel and Thudium 1977; McMurry et al. 2002), the general range of mass density is 1.5-2.1 g/cm^3 in different regions, therefore, the assumption (ρ = 1.5 g/cm^3) can cause an error of about 16.7% (versus the average density of 1.80 g/cm^3 at multiple sites). The average value of σ_g in the OPAC database for most fine aerosol components is 2.14μm (Hess et al. 1998), and the constant value of σ_g (2μm) produces a systematic error of 6% against the average value. The maximum bias (0.01) caused by the constant (3.912) in Koschmieder's equation in extinction occurs when V=0.2km (refer to details in Appendix A-4).

In addition to assumptions, errors in input data affect the accuracy of the concentration and size estimates. Although MODIS AOD has been widely adopted and validated for daily $PM_{2.5}$ concentration retrieval, biases remain because of the algorithm assumptions and cloud contamination. Missing AOD values may arise due to cloud contamination, leading to underestimation, particularly during severe haze. AOD values may also be biased in coastal regions where surface reflectance is more likely to be affected by mixed-pixels and challenging to characterize (Anderson et al. 2013). The validation of MODIS AOD in this study is shown in Figure A2, with R=0.92 and RMSE=0.18. Combining multiple sensors can be an effective way to improve the completeness and accuracy of AOD estimates in the future (Guo et al. 2014; Qi et al. 2013). Other input parameters, for example, meteorological data, can also introduce uncertainty due to model assumptions, coarse resolution and interpolation algorithm. Though the quantitative uncertainty of these parameters was not evaluated in this study due to the dearth of measurements, the good performance of the adopted dataset has been demonstrated in numerous

studies (Deroubaix et al. 2019; Ding et al. 2004; Kalnay et al. 1996). Further, errors in $PM_{2.5}$ concentrations (RMSE= 15.7 $\mu g/m^3$, MAE=10.1$\mu g/m^3$) can propagate to particle size estimates; therefore, as $PM_{2.5}$ estimates improve, so too will the reliability of size estimation results.

Differences in spatial and temporal representativeness between satellite observations and ground-level measurements can also impact the estimation results. The satellite data employed in this study represent an average value for a 3km by 3km pixel, while monitoring stations represent some area around their sites, which are usually located in highly populated regions. Some temporal inconsistency also persists, given differing measurement frequencies and averaging periods between the ground-based and satellite-based observations.

Compared to a laboratory setting, estimating particle radius accurately using satellite data is difficult due to the characteristics of remote sensing (such as coarse resolution and long-distance measurements). Validation is also a challenge because of the limited ground-based measured data. This is why we examined the relationship between estimated particle radius, AERONET columnar retrieved radius, and AE data from AERONET and MODIS. As expected, a decreasing pattern between effective radius and AE was observed. While promising, this interpretation is qualitative, as the relationship between AE and particle effective radius is known to vary with wavelength, size distribution, and composition (Gobbi et al. 2007; Schuster et al. 2006). The observed range of mean effective particle radii, 0.3μm to 1.8μm, is based on an annual average of a single year, and thus cannot fully represent the actual $PM_{2.5}$ size range that may be experienced over time across China. More highly-resolved data with shorter averaging periods over long timescales may reveal a wider range of exposures.

4.6 Conclusion

This chapter presents the first, to our knowledge, national estimates of size-resolved exposures to fine particulate matter. It seeks to address a gap in population-scale estimates that could be used to motivate or inform our understanding of the effect of particle size on human health, which current evidence suggests is important but remains limited by data. In an effort to address this gap, we derive particle effective radius and mass concentration of $PM_{2.5}$ using satellite-derived data and aerosol microphysical properties to explore the spatial pattern and population exposure of $PM_{2.5}$ concentrations and sizes.

We find that most of the Chinese population was exposed to high $PM_{2.5}$ concentrations with small particle sizes. Fewer than 20,000 people in 2017 lived in locations where concentrations met the annual WHO guideline (10 $\mu g/m^3$). Less than 1% lived in regions with a $PM_{2.5}$ mean particle effective radius

above 0.7μm (i.e. aerodynamic diameters lower than 1.0μm) in 2017. The national population-weighted annual average concentration of $PM_{2.5}$ and particle effective radius were estimated to be 52μg/m^3 and 0.5μm in 2017, respectively. Spatially, $PM_{2.5}$ concentrations to the east of the Heihe-Tengchong population line were generally higher than those in the west, while the particle radius was larger in the west, especially in the desert. Specifically, among four economic regions, the Centre region had the highest ambient $PM_{2.5}$ concentrations with the smallest particle radius, where 90% of the population was exposed to $PM_{2.5}$ concentrations higher than 50 μg/m^3 and only 2% was exposed to a mean effective particle radius larger than 0.5μm in 2017. High $PM_{2.5}$ concentrations and small particle sizes were more likely to occur in regions with high GDP and population densities, which is in line with other work suggesting an important contribution from industrial and economic activity. Temporally, summer is the season in which the highest percentage of the national population (86%) lived in areas with a mean effective radius of $PM_{2.5}$ less than 0.5μm. In the Taklamakan Desert, where aerosols are dominated by natural sources (such as dust and sand), large particle radii were more prevalent in spring due to the higher frequency of dust events, despite relatively low $PM_{2.5}$ concentrations during this period.

The validation of particle radius in this work is restricted by the available particle size measurements. Large-scale and long-term particle size measurements in polluted regions, such as India and China, are especially limited. The AERONET columnar radius retrievals and MODIS AE data provide large-coverage observations of a variable linked to aerosol size were used to validate our radius estimates, yielding a MAE of 0.12μm. Sensitivity analysis of retrieval parameters found a potential MAE contribution of 0.1μm. Some of this difference may be attributable to differences in retrieval approaches. Accuracy may be improved with the advent of further ground-based measurements, higher resolution data input, or more detailed information on aerosol properties. This chapter demonstrates the potential of remote sensing techniques for estimating population-scale size-resolved $PM_{2.5}$ exposures, reveals prevalent exposure to sub-micron particles, and motivates further research on the effect of particle size on health outcomes related to particulate matter.

Chapter 5

Recent Trends in Premature Mortality and Health Disparities Attributable to Ambient $PM_{2.5}$ Exposure in China: 2005–2017

In this Chapter, we quantify ambient $PM_{2.5}$ exposure and the resulting public health burden in China across recent decades that saw tremendous change in economic output and air pollution. Despite the well-studied significance of this burden, its national trajectory and distribution across vulnerable populations is not well understood. We fill this gap using recent advances in satellite remote sensing techniques, exposure-response relationships, and metrics of environmental inequality. We provide estimates of population exposure, $PM_{2.5}$ attributable premature deaths (caused by stroke, ischemic heart disease, chronic obstructive pulmonary disease, lower respiratory infection, and lung cancer), and indices of distributional equity across income groups and between provinces. We find that the total public health burden continues to rise despite lower PM2.5 exposures, primarily due to rising population and baseline risks. Stroke and ischemic heart disease (IHD) are the two leading causes of premature death attributable to PM2.5 exposure, though COPD (chronic obstructive pulmonary disease) and LRI (lower respiratory infection) disproportionately affect poorer provinces. Total premature mortality attributable to PM2.5 exposure in China has become more equitably distributed across provinces.

This chapter is structured as follows. Section 5.1 states the background and motivation of the study. Sections 5.2 introduces the adopted datasets and the methods for exposure estimation, excess mortality assessment, and inequality analysis. Section 5.3 provides the long-term trends of $PM_{2.5}$ exposure, attributable mortality, and environmental health inequality during 2005-2017. Section 5.4 discusses the main findings and limitations in this chapter. Section 5.5 concludes the chapter.

5.1 Introduction

The adverse impacts of fine particulate matter ($PM_{2.5}$) on human health are well established, including an estimated 4.2 million (95% CI: 3.7, 4.8) global premature deaths in 2015 (Cohen et al. 2017). Over 30% of these deaths occurred in China in 2012 (WHO 2016), where ambient $PM_{2.5}$ ranked fourth nationally among 67 risk factors for disability-adjusted life-years (DALYs) (Yang et al. 2013) . The most common non-communicable diseases in China, including chronic obstructive pulmonary disease

(COPD), ischemic heart disease (IHD), lung cancer (LC), and stroke, are all associated with $PM_{2.5}$ exposure (Zhou et al. 2016b).

The dramatic rise in $PM_{2.5}$-related mortality in China has coincided with significant economic growth (Liu et al. 2017b). In response, the Chinese government has adopted and updated air quality standards, issued pollution control policies, established expanded monitoring networks, and launched targeted initiatives to mitigate air pollution, particularly in 2013. Although many studies have examined the effect of such actions on $PM_{2.5}$ concentrations (Lin et al. 2018; Xue et al. 2019a), fewer have quantified the resulting changes in the public health impacts over these important recent decades (Zhao et al. 2018). Many others present national mortality estimates for one or more years, but do not provide a long time-series (see Table B2). Some sub-national studies have presented decadal time series of $PM_{2.5}$-related mortality (Lu et al. 2019; Zheng et al. 2015b; Zhu et al. 2019). Few studies present the national mortality burden in China over time (Liu et al. 2017b; Xie et al. 2016a). A decadal time series can inform air quality policies by quantifying changes in the resulting public health burden (Fann et al. 2018). Further, it can be used to evaluate the resulting trends in national and interprovincial equity (Muller et al. 2018).

Changes in the Chinese economy and resulting air pollution can impose unequal impacts across the population. Between 2006 and 2017, measures of economic inequality in China peaked shortly after the Great Recession, followed by a shift towards greater equality (Li and Sicular 2014). Air pollution is known to have significant economic impacts in China, e.g. 5.9% loss in GDP from 1997-2005 (Matus et al. 2012). The health and economic burden associated with $PM_{2.5}$ can disproportionately affect vulnerable populations (Bell and Ebisu 2012; Huang et al. 2019; Zhao et al. 2019). WHO (2018) reported that 91% of global premature deaths attributable to air pollution occurred in low- and middle-income countries. Patterns of environmental inequality, typically quantified by Atkinson Index and Gini Index, vary substantially across spatial domains (Clark et al. 2014; Fann et al. 2018; Muller et al. 2018; Rosofsky et al. 2018). Policies to reduce air pollution can offer substantial economic benefits, though some provinces gain while others lose, potentially exacerbating interprovincial inequality (Xie et al. 2016b). Despite substantial literature on $PM_{2.5}$ exposure and its health impacts in China, to our knowledge, little research has evaluated the consequent environmental inequality (Hajat et al. 2015). Tracking the distribution of $PM_{2.5}$-related health impacts among subpopulations can help to formulate and monitor targeted policies to alleviate inequality.

China's network of air quality monitors has been growing since 2013; however, methods with more complete spatial coverage are still needed for national time series, especially for historical air quality

records and regions with fewer monitors (such as western China). To capture periods before 2013, studies of $PM_{2.5}$ concentrations and related mortality in China have used techniques including artificial intelligence (Li et al. 2019; Xue et al. 2019a), satellite data (Lu et al., 2019; Zheng et al., 2015), chemical transport models (CTMs) (2016b, 2019), or a combination thereof (Geng et al. 2015; van Donkelaar et al. 2016; Xie et al. 2016a) to take remote rural areas with limited air quality measurements into account.

Estimating long-term trends in $PM_{2.5}$-related mortality in China relies on representing exposures and exposure-response (or concentration-response) functions (CRFs). CRFs should be representative of the observed exposure range in the underlying population, ideally applying local, high-quality observations within the relevant range of concentrations (West et al. 2016). In China, $PM_{2.5}$-related risks may be underestimated due to a paucity of cohort studies conducted in high-concentration regions (Maji et al. 2018b; Pope C. Arden et al. 2018). Specifically, the CRFs currently applied in China are mostly derived from epidemiological studies conducted in western Europe and North America, such as the Integrated Exposure-Response (IER) function employed in the Global Burden Diseases study (Maji et al. 2018a; Zhao et al. 2018). Yin et al. (2017) reported higher hazard ratio estimates from a national Chinese cohort study than IER estimates. A recent CRF, the Global Exposure Mortality Model (GEMM) introduced by Burnett et al. (2018), is based on cohort studies (including one conducted in China) of outdoor $PM_{2.5}$ exposure. It covers 97% of the global population to assess the $PM_{2.5}$-related health outcomes, including COPD, IHD, LC, lower respiratory infections (LRI), and stroke.

Here, we quantify long-term $PM_{2.5}$ exposure, cause-specific mortality and environmental inequality over China. We leverage satellite-based and CTM estimates of exposure, and the GEMM CRF to estimate $PM_{2.5}$-related premature mortality. We quantify the corresponding health inequalities at the provincial and national levels using a modified Gini coefficient based on mortality. This paper seeks to answer the following questions: (1) How do $PM_{2.5}$ levels and related health burdens vary spatially and temporally over China during 2005-2017? (2) How equitably is the $PM_{2.5}$-related health burden distributed across populations in different regions and with different socioeconomic characteristics (i.e. GDP per capita)? (3) How does this pattern of environmental inequality change over the study period?

5.2 Data and Methods

5.2.1 Ground-level $PM_{2.5}$ Estimation

Two retrieval strategies were adopted to estimate ground-level $PM_{2.5}$ concentrations over China from 2005 to 2017 using satellite and meteorological data: a previously developed fused surface (van Donkelaar et al. 2015, 2019), and a new semi-geographical weighted regression (semi-GWR) model developed herein. The fused surface is used for its superior performance in the years 2005-2012 owing to the limited number of $PM_{2.5}$ measurements in this period. These surfaces, combining multi-sensor satellite AOD, the GEOS-Chem CTM, and surface observations, is provided by "Atmospheric Composition Analysis Group" at Dalhousie University (van Donkelaar et al. 2016). They have been used in previous environment and health impact studies (Peng et al. 2016; Sherbinin et al. 2014; Xue et al. 2019b).

Taking advantage of the published air pollutant measurements from the Chinese government, we established and trained a semi-GWR model based on the hygroscopic growth- and vertical-corrected aerosol optical depth (τ) data and auxiliary data, including temperature(T), wind speed (WS), visibility (V) and elevation (DEM). These variables were selected given their expected influence on surface $PM_{2.5}$ (Day and Pandis 2011; Wang et al. 2018b; Xiao et al. 2018; Zhou et al. 2015). Variance inflation factor was calculated to ensure low collinearity of the variables. Compared to the fused surface from 2013 to 2017, the $PM_{2.5}$ concentrations estimated by the GWR model in the corresponding year were more accurate, especially in 2017 (see Figure B1 and Figure B2). Therefore, $PM_{2.5}$ was estimated for 2013-2017 according to the following model structure:

$$PM_{2.5\_GWR(i,j,y)} = \beta_{0(i,j,y)} + \beta_{b_{ext,dry\,(i,j,y)}} b_{ext,dry\,(i,j,y)} + \beta_{T(i,j,y)} T_{(i,j,y)} + \beta_{WS(i,j,y)} WS_{(i,j,y)} + \beta_{V(i,j,y)} V_{(i,j,y)} + \beta_{DEM(i,j,y)} DEM_{(i,j,y)} + \varepsilon_{(i,j,y)} \quad (5\text{-}1)$$

where $PM_{2.5\_GWR(i,j,y)}$ is the annual ground-level $PM_{2.5}$ concentration at location (i, j) in year y; β_0 is the intercept for each year; β denotes the slope of the variable with the corresponding subscript. $\varepsilon_{(i,j,y)}$ is the error term at location (i, j) in year y. Geographic weights were estimated with Gaussian distance decay functions. Since the optical-mass relationship has proven to be related to aerosol hygroscopic growth and the height of planetary boundary layer (HPBL) (Kaufman et al. 2003; Koelemeijer et al. 2006), the satellite-observed τ was corrected to "meteo-scaled" optical depth $b_{ext,dry\,(i,j)}$ using Eq.(5-2) :

$$\beta_{\mathrm{b_{ext,dry}}\,(i,j)}\,\mathrm{b_{ext,dry}}\,(i,j) = \frac{\tau}{\mathrm{HPBL}*\mathrm{f(RH)}} \quad (5\text{-}2)$$

where f(RH) is hygroscopic growth coefficient, which was calculated based on previous studies as in (Liu et al. 2019b) by geographically weighting three different estimates developed in China (Chen et al. 2014a; Liu et al. 2008; Zhang et al. 2015b). To unify the spatial distributions of two concentration sources, the CTM-based fused concentrations from 2013 to 2017 were then corrected by the GWR-based results using linear regressions. The regression coefficients were fitted at the provincial level in each year.

5.2.2 Ground-level $PM_{2.5}$ Concentrations

Air pollutant measurements in China were released to the public in 2013, providing data support to $PM_{2.5}$ modelling and validation. Here, we use the ground-level $PM_{2.5}$ concentrations (2013-2017) from the "China National Environmental Monitoring Center (CNEMC) (http://www.cnemc.cn/)". The collected hourly measurements were averaged to obtain annual $PM_{2.5}$ concentrations. Ground-level measurements before 2013 were collected from previous publications, provided in Table B1. As data before 2013 were limited, these concentrations were only used for validation.

5.2.3 Mortality Assessment

Cause-specific premature mortality (ΔM) attributable to $PM_{2.5}$ exposure over China was estimated using Eq. (5-3).

$$\Delta\mathrm{M} = \mathrm{y}_0\left(\frac{RR-1}{RR}\right)\mathrm{pop} \quad (5\text{-}3)$$

where y_0 represents the baseline incidence rate for each specific disease; pop represents the age-specific population exposed to ambient $PM_{2.5}$. RR represents the corresponding Relative Risk at a given concentration, which is calculated by CRFs. The GEMM, a recent CRF established by Burnett et al. (2018), was adopted in this study to quantify the $PM_{2.5}$ attributable health impacts. This function was chosen because it allows toxicity to vary across the total inhaled dose, and was modeled based on outdoor air pollution cohort studies from 16 countries (including the study in China) that cover much of the global exposure range of ambient $PM_{2.5}$ concentrations. It takes the functional form:

$$\mathrm{RR} = \exp\left(\frac{\theta\ln\left(1+\frac{\Delta\mathrm{C}}{\alpha}\right)}{1+\exp\left(-\frac{\Delta\mathrm{C}-\mu}{\nu}\right)}\right) \quad (5\text{-}4)$$

where ΔC represents the difference between ambient $PM_{2.5}$ concentrations and baseline concentration; α, θ, μ, ν define the shape of the CRF (θ and its SE were estimated using the Cox

proportional hazards model) (Burnett et al. 2018). GEMM includes forms for pooled cohorts and specific cohorts. The disease-specific RR calculations in this study were based on the model parameters for the Chinese cohort study (details in Table B3). The baseline concentration 2.4μg/m^3 is used, as in (Burnett et al. 2018), based on the lowest observed exposure in any cohort. We conducted 1000 Monte Carlo simulations to estimate the 95th confidence interval in the excess mortalities.

5.2.4 Health Data

The baseline incidence rates of five leading causes of death (COD) comprising the Global Burden of Disease (GBD) $PM_{2.5}$-associated mortality estimates , including COPD, IHD, LC, LRI, and stroke, were derived from Zhou et al. (2016) at the provincial scale. The annual variation of mortality rates during the study period in China was generated from the GBD dataset found at http://ghdx.healthdata.org/. The province-level baselines for each year were calculated based on the assumption that the annual variation for each province follows the national trend.

5.2.5 Inequality Analysis

We estimate measures of both economic and environmental inequality. We use the traditional Lorenz curve to characterize the distribution of income (Gastwirth and Glauberman 1976). We build on this concept to also characterize the share of $PM_{2.5}$ attributable mortality. To do this, population and excess premature mortality in each pixel were first ranked by GDP per capita. The cumulative share of mortality was then plotted against the cumulative share of population, ranked by income (see Figure 5.1). We also built the Lorenz curves at the provincial scale to evaluate the distribution of mortality across the provinces as a measure of interprovincial equity. Based on the Lorenz curve, the Gini coefficient can be calculated by dividing the area of A by 0.5 (which equals to A+B in Figure 5.1a). The smaller the Gini coefficient, the closer the distance between Lorenz curve and ideal equality line. Thus, a smaller Gini reflects greater equality.

$$Gini = 1 - \sum_{i=1}^{n}(x_i - x_{i-1})(y_i - y_{i-1}) \quad (5\text{-}5)$$

where n represents the number of pixels/provinces; x_i represents the cumulative percentage of the population to pixel/province i; y_i represents the cumulative percentage of the $PM_{2.5}$-attributable mortalities (Stroke, COPD, IHD, LC, LRIs). Similar metrics were evaluated for each of the five causes of death (5-COD).

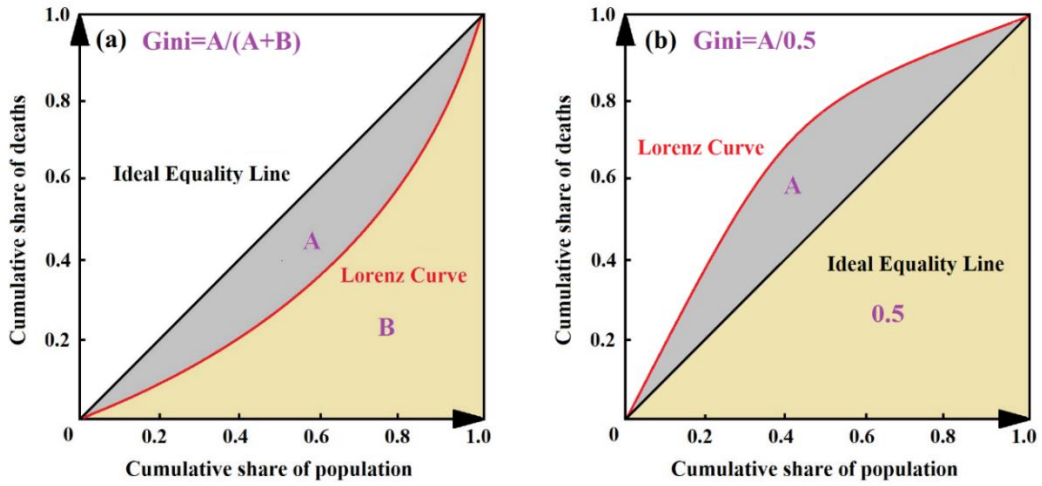

Figure 5.1 Definition of Lorenz curve and Gini coefficient

5.2.6 Socioeconomic Data

Gridded population and GDP data in the base years (2005, 2010 and 2015) were obtained from "Resource and Environmental Science Data Center of the Chinese Academy of Sciences (RESDC) (http://www.resdc.cn/)", with a spatial resolution of 1km (Xu 2017). The gridded population/GDP data for the remaining years were calculated based the assumption that the percentage of each gridded value to the corresponding province-level value remains stable in five years. The province-level annual population, GDP and demographic data from 2005 to 2017 were from "Chinese National Bureau of Statistics (http://www.stats.gov.cn/tjsj/ndsj/)". Both gridded population and GDP data were resampled to 3km to match the spatial resolution of ground $PM_{2.5}$ concentrations.

5.3 Results

5.3.1 $PM_{2.5}$ Exposure Assessment

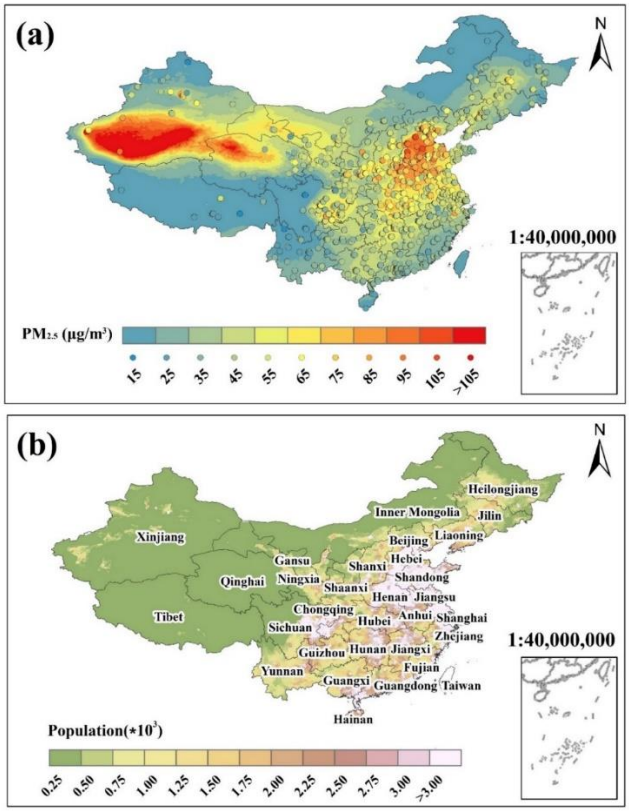

Figure 5.2 Spatial distributions of (a) 13-year mean $PM_{2.5}$ concentrations (b) population in 2017.

Figure 5.2 shows the spatial distribution of 13-year mean $PM_{2.5}$ concentrations across China. The polluted region with the highest $PM_{2.5}$ concentrations is the Taklamakan Desert, where natural particle sources, such as dust and sand, dominate (Huang et al. 2008). The Beijing-Tianjin-Hebei (BTH) region, the Sichuan Basin, and central China (including Shanxi, Henan and part of Shandong, Jiangsu, Anhui, and Shaanxi provinces) are urban agglomerations with both high $PM_{2.5}$ concentrations and population density, in which anthropogenic emissions dominate (Zhang et al. 2015a, 2013; Zheng et al. 2015a). Henan and Hebei are the provinces with the highest exposures, with population-weighted mean PM2.5 concentrations exceeding 72 $\mu g/m^3$ during 2005-2017. The patterns of geographical annual mean and population-weighted mean $PM_{2.5}$ concentrations for each year are provided in Figure B3 and Figure B4. National $PM_{2.5}$ exposure trends downward from 2005 to 2017, with an average of 49 $\mu g/m^3$. Since

China issued the "Air Pollution Prevention and Control Action Plan (APPCAP)" in 2013, population-weighted $PM_{2.5}$ concentrations have fallen by 21% (green line in Figure 5.3b). The improved agreement between our population-weighted (green line) and station-based (cyan line) concentration estimates indicated that the monitoring network has gradually expanded and already covered most of the densely-populated area in 2017. We evaluate this agreement in Figure 5.3a. The overall R^2 is 0.81 and the root mean square error (RMSE) is 8.3μg/m^3. Figure 5.2a shows the spatial pattern of estimates is also consistent with that of ground measurements, indicating that the $PM_{2.5}$ concentrations used are sufficiently reliable for our analysis.

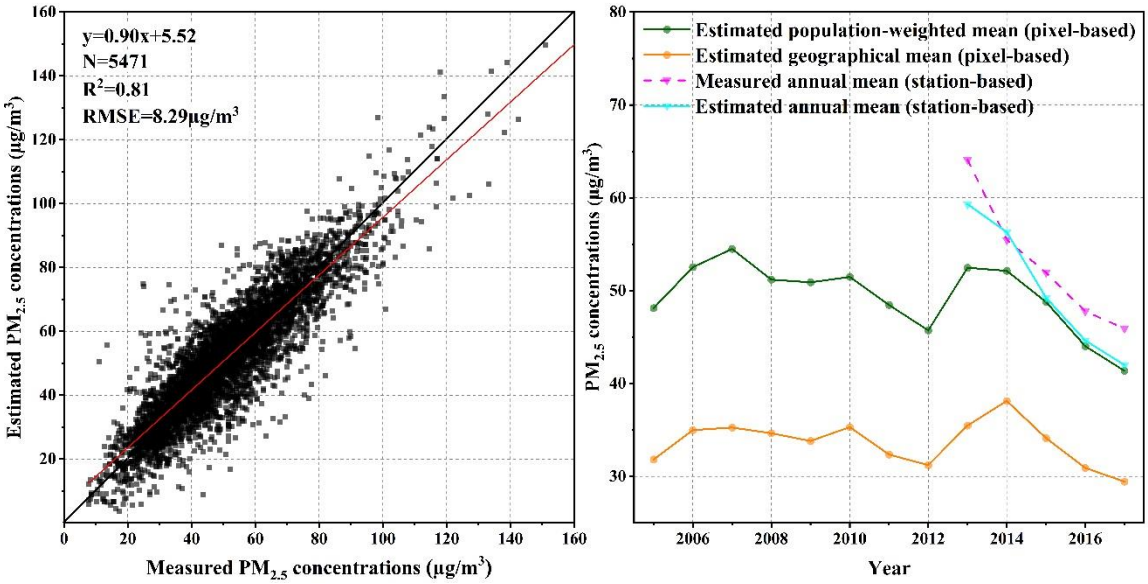

Figure 5.3 (a) Validation results and (b) temporal trends of satellite-based $PM_{2.5}$ estimates in China

5.3.2 Mortality Attributable to $PM_{2.5}$

Premature mortality attributable to chronic $PM_{2.5}$ exposure was estimated using Eq. (5-3) from 2005 to 2017 in China. Total excess deaths were calculated as the sum across five causes of deaths (5-COD), (i.e. COPD, IHD, LC, LRI, and stroke). As shown in Figure 5.4, COPD mortality related to $PM_{2.5}$ exposure decreased from 280 (95%CI: 240, 320) thousand in 2005 to 250 (95% CI: 220, 290) thousand in 2017; IHD mortality increased from 390 (95%CI: 370, 400) thousand in 2005 to 680 (95%CI: 660, 690) thousand in 2017, with a peak of 700 (95%CI: 680, 710) thousand in 2015; LC mortality increased from 94 (95%CI: 85, 100) thousand in 2005 to 160 (95%CI: 140, 180) thousand in 2017; LRI mortality decreased from 120 (95%CI: 100, 130) thousand in 2005 to 98 (95%CI: 85, 110) thousand in 2017; and the 5-COD mortality increased from 1.4 (95%CI: 1.2, 1.5) million in 2005 to 1.9 (95%CI: 1.7, 2.1)

million in 2015, before dropping to 1.8 (95%CI: 1.6, 2.0) million in 2017. Stroke and IHD were the two leading causes of premature deaths attributable to $PM_{2.5}$ exposure over China, with respective 13-year means of 580 (95%CI: 510, 660) and 560 (95%CI: 550, 570) thousand, which contribute approximately 35.5% and 33.8% of cause-specific mortality during 2005-2017 (Figure 5.5). The average mortalities caused by COPD, LC and LRI are 263.6 (95%CI: 225.9,300.1), 132.3 (95%CI: 118.6,145.5) and 106.3 (95%CI: 93.4, 118.4) thousand, respectively, which are 16.2%, 8.0% and 6.5% of the total cause-specific mortality during the study period.

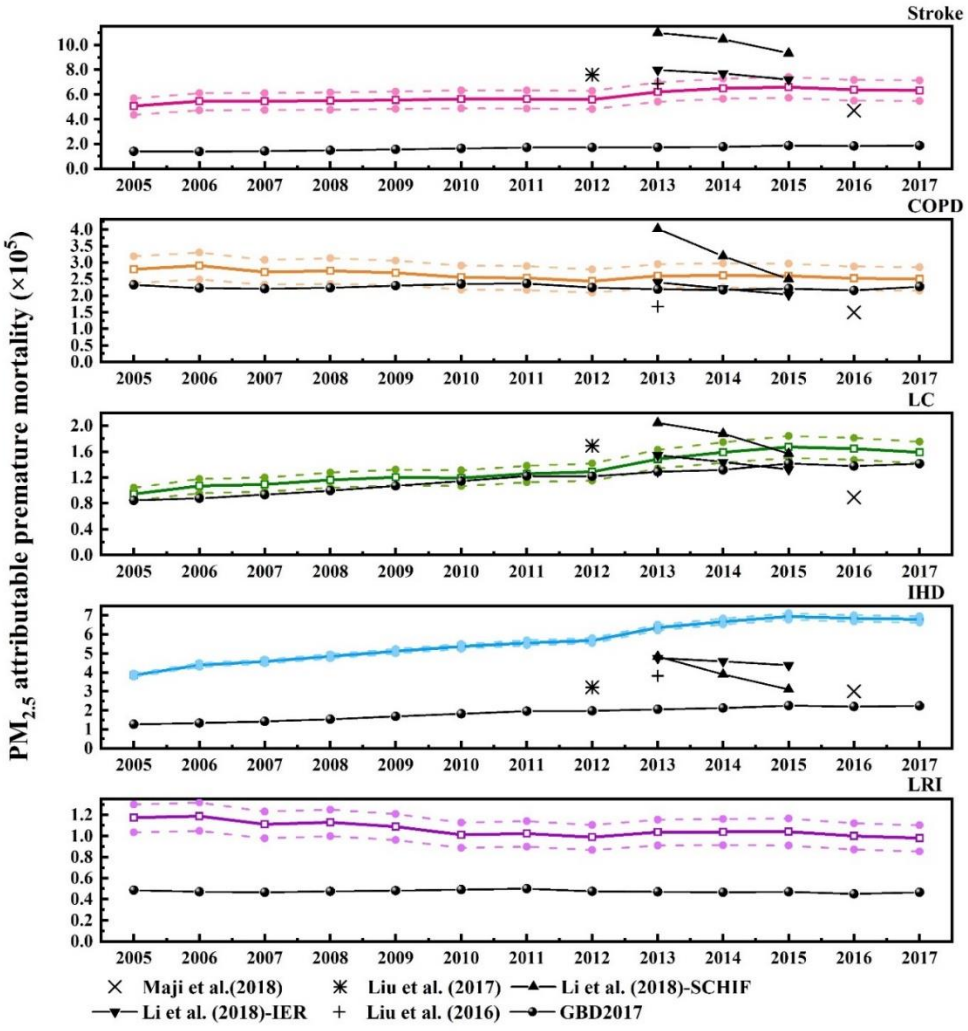

Figure 5.4 Temporal trends of $PM_{2.5}$ attributable mortality from 2005 to 2017

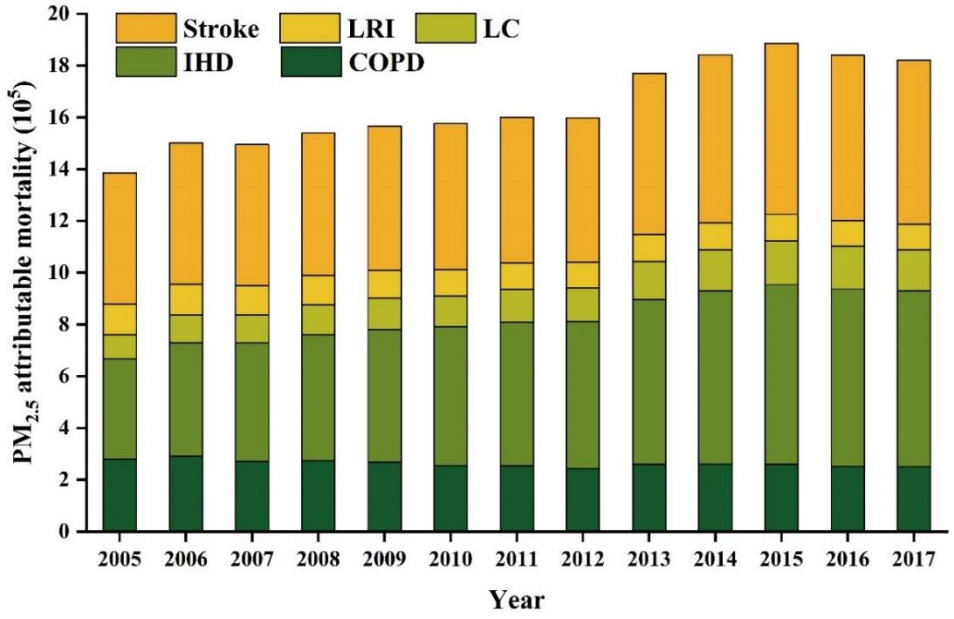

Figure 5.5 $PM_{2.5}$ attributable disease-specific mortality in China by year

Table 5.1 shows the average annual $PM_{2.5}$ attributable premature mortality by cause of death from 2005 to 2017. For the complete time-series of deaths by province and cause of death, see Figure B7. Henan, Shandong, Hebei, and Sichuan have the highest mean values (160, 140, 120, and 110 thousand, respectively) comprising 33% of the national total. Mortality by IHD and stroke are highest in Henan province, with values of 60 (95%CI: 59, 61) and 67 (95%CI: 59, 74) thousand, respectively. $PM_{2.5}$-related mortality caused by COPD and LRIs reach 32 (95%CI: 28, 37) and 8.8 (95%CI: 7.8, 9.8) thousand in Sichuan province. Shandong is the province with the highest 13-year mean LC mortality. The spatial distribution of mortality by cause of death is shown in Figure 5.6.

Table 5.1 Annual $PM_{2.5}$ attributable premature mortality by COD and province (average of 2005-2017)

Province	COPD (10^3)	IHD (10^3)	LC (10^3)	LRIs (10^3)	Stroke (10^3)	5-COD (10^3)
Anhui	14 (12, 16)	27 (26, 28)	7.5 (6.8, 8.3)	4.7 (4.1, 5.2)	35 (31, 40)	89 (80, 96)
Beijing	2 (1.8, 2.3)	12 (12, 12)	2.6 (2.3, 2.8)	1.8 (1.6, 1.9)	9 (7.9, 10)	27 (25, 29)
Chongqing	11 (9.6, 13)	9.6 (9.3, 9.8)	4 (3.6, 4.4)	2.3 (2, 2.5)	12 (11, 14)	39 (35, 43)
Fujian	4.2 (3.5, 4.8)	6.3 (6.1, 6.5)	1.9 (1.6, 2.1)	2.5 (2.1, 2.8)	6.9 (5.8, 7.9)	22 (19, 24)
Gansu	11 (9.2, 12)	9.8 (9.5, 10)	1.2 (1, 1.3)	2.8 (2.5, 3.2)	9.9 (8.5, 11)	34 (31, 38)
Guangdong	13 (11, 15)	30 (29, 31)	6.6 (5.8, 7.3)	7.6 (6.7, 8.6)	25 (21, 28)	82 (74, 90)
Guangxi	12 (9.9, 13)	19 (18, 19)	4.2 (3.8, 4.7)	7.3 (6.4, 8.1)	18 (15, 20)	60 (54, 66)
Guizhou	12 (10, 14)	9.5 (9.2, 9.7)	2.6 (2.3, 2.8)	6.8 (5.9, 7.6)	17 (15, 19)	48 (42, 53)
Hainan	0.69 (0.58, 0.8)	1.2 (1.2, 1.3)	0.25 (0.22, 0.27)	0.26 (0.22, 0.29)	1.1 (0.9, 1.2)	3.5 (3.1, 3.9)
Hebei	8.6 (7.4, 9.8)	46 (45, 47)	8.9 (8.1, 9.8)	4.9 (4.3, 5.4)	52 (45, 57)	120 (110, 130)
Heilongjiang	3 (2.6, 3.5)	20 (19, 21)	3.6 (3.2, 4)	1.8 (1.6, 2)	13 (11, 15)	41 (38, 45)
Henan	21 (18, 24)	60 (59, 61)	11 (9.8, 12)	6.1 (5.4, 6.7)	67 (59, 74)	160 (150, 180)
Hongkong	0.02 (0.01, 0.02)	0.05 (0.05, 0.05)	0.01 (0.01, 0.01)	0.02 (0.01, 0.02)	0.03 (0.03, 0.04)	0.13 (0.12, 0.14)
Hubei	14 (12, 16)	26 (25, 26)	6.9 (6.2, 7.6)	3.5 (3.1, 3.9)	33 (29, 37)	84 (76, 91)
Hunan	14 (12, 16)	29 (28, 30)	6.1 (5.5, 6.7)	6.2 (5.5, 6.9)	27 (23, 30)	82 (74, 89)
Inner Mongolia	3.2 (2.8, 3.7)	12 (12, 13)	1.8 (1.6, 2)	1.3 (1.1, 1.4)	9.7 (8.3, 11)	28 (26, 31)
Jiangsu	14 (12, 16)	23 (23, 24)	8.1 (7.3, 8.9)	4 (3.6, 4.5)	33 (29, 37)	83 (75, 90)
Jiangxi	9.2 (7.9, 11)	17 (17, 18)	4.5 (4, 5)	3.1 (2.7, 3.5)	16 (14, 18)	50 (45, 55)
Jilin	1.9 (1.6, 2.2)	15 (15, 16)	2.4 (2.1, 2.6)	1.9 (1.7, 2.1)	11 (9.3, 12)	33 (30, 35)
Liaoning	3.6 (3, 4.1)	22 (21, 22)	5.3 (4.7, 5.8)	3.1 (2.7, 3.5)	19 (16, 21)	53 (48, 57)
Ningxia	1.1 (0.96, 1.3)	3.3 (3.2, 3.3)	0.43 (0.38, 0.48)	0.64 (0.56, 0.71)	2.2 (1.9, 2.5)	7.7 (7, 8.4)
Qinghai	1.8 (1.5, 2)	2.6 (2.5, 2.7)	0.29 (0.26, 0.32)	0.57 (0.5, 0.64)	2.3 (1.9, 2.6)	7.5 (6.7, 8.2)
Shaanxi	5.4 (4.6, 6.1)	19 (18, 19)	2.7 (2.4, 3)	2.5 (2.2, 2.8)	18 (16, 20)	47 (43, 51)
Shandong	18 (16, 20)	55 (53, 56)	14 (12, 15)	5.2 (4.6, 5.8)	52 (45, 57)	140 (130, 150)
Shanghai	2.5 (2.2, 2.9)	3.8 (3.8, 3.9)	1.8 (1.6, 2)	0.46 (0.41, 0.52)	5.1 (4.4, 5.7)	14 (12, 15)
Shanxi	4.9 (4.2, 5.6)	16 (16, 16)	3.4 (3.1, 3.8)	3.1 (2.7, 3.4)	17 (15, 19)	44 (40, 48)
Sichuan	32 (28, 37)	23 (23, 24)	10 (9.2, 11)	8.8 (7.8, 9.8)	35 (30, 39)	110 (98, 120)
Tianjin	1.6 (1.4, 1.8)	10 (10, 11)	2.3 (2.1, 2.5)	1.9 (1.7, 2.1)	7.2 (6.3, 8)	23 (22, 25)

Tibet	0.1 (0.1, 0.1)	0.24 (0.23, 0.25)	0.01 (0.01, 0.01)	0.13 (0.11, 0.15)	0.23 (0.19, 0.27)	0.69 (0.61, 0.77)
Xinjiang	7.3 (6.3, 8.3)	17 (17, 18)	2 (1.8, 2.2)	2.7 (2.4, 3)	12 (11, 14)	41 (38, 45)
Yunnan	7.9 (6.6, 9.1)	9.3 (9, 9.5)	1.8 (1.5, 2)	4.1 (3.5, 4.7)	7.1 (6, 8.3)	30 (27, 34)
Zhejiang	8.1 (6.9, 9.3)	7.5 (7.3, 7.6)	4.5 (4, 4.9)	4.2 (3.7, 4.7)	12 (11, 14)	37 (32, 40)

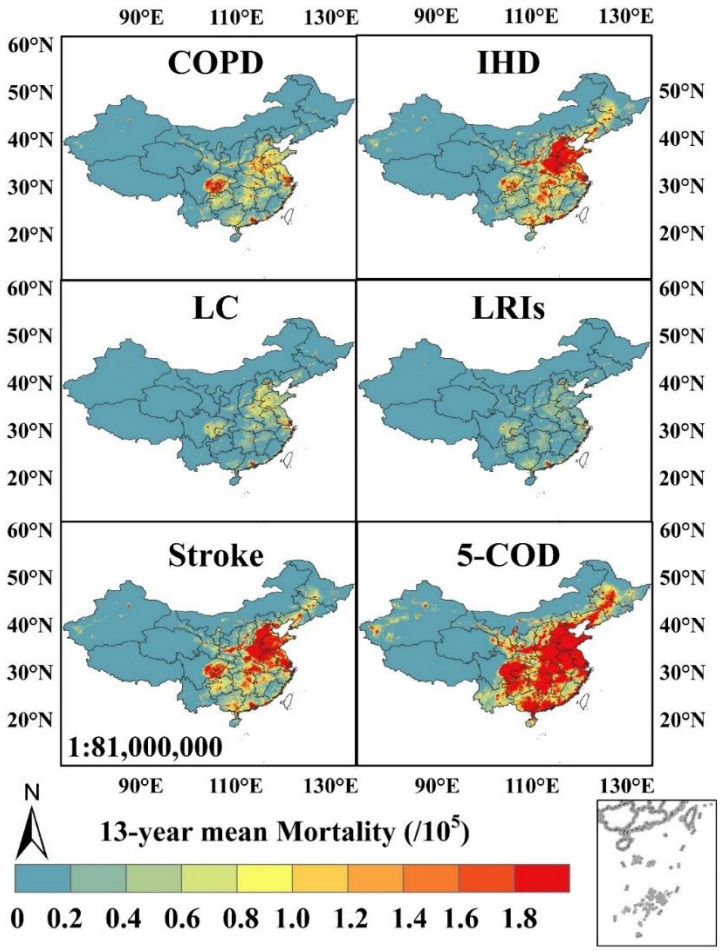

Figure 5.6 Spatial patterns of 13-year annual mean $PM_{2.5}$ attributable mortality by cause of death

5.3.3 Inequality Analysis

We present multiple metrics of inequality including and expanding on the traditional Gini coefficient. First, we distinguish between traditional economic and health indices. We denote the traditional economic Gini by "GDP per capita", which we use as a proxy for income due to data availability. We also calculate a Gini coefficient based on the distribution of deaths, which we denote by its respective

cause of death. Second, we evaluate equity at the national scale, as well as between provinces. We term these metrics as follows: “national Gini” is based on the distribution of GDP per capita across all pixels in the nation; “interprovincial Gini” orders the population in provinces by provincial mean GDP per capita. These national metrics allow for the comparison of changes in economic and health-related equity over the study period. The interprovincial metrics test whether poorer provinces suffer a disproportionate share of the public health burden from $PM_{2.5}$ pollution.

The national Gini traditional coefficient in Figure 5.7(a) trends towards greater equality beginning in 2015, dropping from appropriately 0.42 to 0.31 over the study period. Compared to the economic picture, Gini coefficients calculated based on mortality were low, with all values less than 0.1, indicating the $PM_{2.5}$ attributable mortality was distributed more evenly than GDP per capita. Figure 5.7 (b) shows that the interprovincial GDP per capita Gini declined from 0.31 to 0.19 from 2005 to 2017, denoting an increasing fairness in the distribution of income among provinces in China. A similar pattern was also observed in mortality due to three $PM_{2.5}$ related health outcomes (COPD, LRI, and stroke). The interprovincial Gini coefficients based on IHD and LC had miniscule mean values of 0.01 and 0.02, respectively.

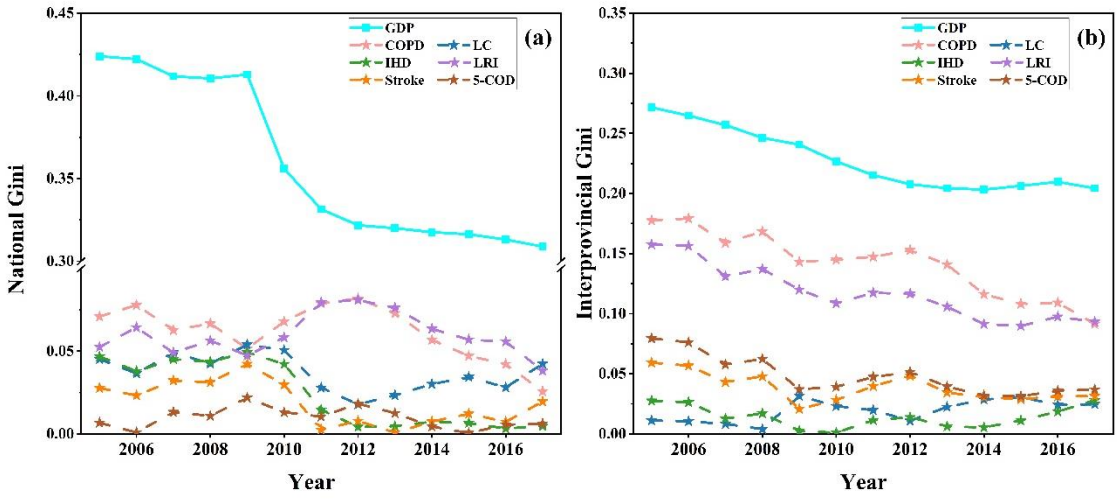

Figure 5.7 Temporal trends of (a) national Gini and (b) interprovincial Gini coefficients for GDP per capita and premature mortality caused by different $PM_{2.5}$ related health outcomes.

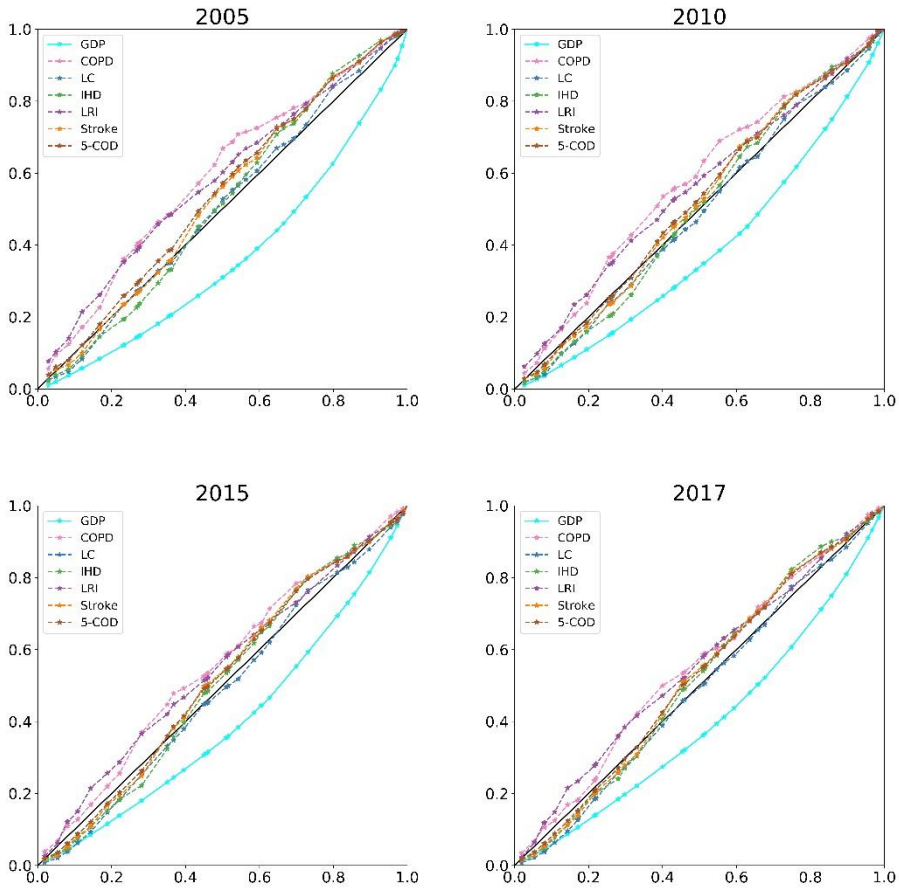

Figure 5.8 Interprovincial Lorenz curves for $PM_{2.5}$ attributable premature mortality and economic inequality during 2005-2017

Figure 5.8 shows the Lorenz curves depicting interprovincial inequality for the years 2005 and 2017 (remaining years in Supplemental Material). As with the mortality-based Gini index, the Lorenz curve shows that COPD and LRI disproportionately affect provinces with low GDP per capita, while LC is distributed evenly. Conversely, the curve for 2005 shows that low income provinces had fewer IHD and stroke than middle to high income regions. This situation generally persists in 2017, though there is less disparity across most outcomes. In 2017, the Chinese population with 40% of the income (as GDP) experienced 43% of $PM_{2.5}$-attributable premature deaths, which is 110 (95%CI: 99,120) thousand higher than corresponding population (richest 40%). National Lorenz curves for 5-COD are provided in Figure B5. The disparate effects of different causes on different income groups balance one another, yielding a more equal picture across all causes of death.

5.4 Discussion

While numerous studies have documented trends in China's air pollution, fewer have examined national long-term premature mortality, and none, to our knowledge, have quantified the resulting health disparities. Here, we find, as in the GBD study (Figure 5.4), that premature mortality associated with $PM_{2.5}$ has continued to rise even after the enactment of significant pollution control policies (APPCAP) in 2013. This rise in premature deaths occurs despite concentrations that have fallen nationally, though concentrations in some provinces rebounded in 2017 (Figure B6). On average, the 13-year mean concentrations are highest in the Taklamakan Desert in the west, and in urban agglomerations such as those found in the North China Plain and the Sichuan Basin. This pattern is consistent with long-term means found in previous studies over an earlier period (Ma et al. 2016a; van Donkelaar et al. 2015).

These concentrations result in total cause-specific mortality that peaked in 2015, with 1.9 (95%CI: 1.7, 2.1) million annual premature deaths, an increase of 500,000 since 2005. Similar trends were also reported by GBD studies, showing that 5-COD mortality rose by 30% from 2005 to 2015 before decreasing to 0.83 million in 2017 (Naghavi et al. 2017). While estimates vary widely, total deaths in this study are generally above the means of previous estimates (Table B2). The discrepancy of results can be explained by various $PM_{2.5}$ exposure sources (such as estimation methods, spatial resolution and coverage), CRFs, and other input data sources (such as baseline incidence rates and demographics). In particular, the use of GEMM in this study could explain much of its higher estimates, especially compared to previous studies using the IER (Table B2), since GEMM RR were larger than IER estimates, especially for LRIs, IHD, and stroke (Burnett et al. 2018). Pope C. Arden *et al.*, (2018) pointed out that the IER approach adopted for GBD studies might underestimate health impacts attributable to $PM_{2.5}$ in regions with high ambient concentrations. The GEMM CRF used here is based on the Chinese cohort study (Yin et al. 2017), and results in higher estimates than the IER (Burnett et al. 2018). Aside from differences in magnitude, the trends by COD generally match those of the GBD within errors, with deaths generally flat (stroke, COPD), increasing until 2015 then falling (LC, IHD), or decreasing (LRI). As for the other national, multi-year trends, R. Xie et al. (2016) also shows a similar pattern between its common years (2005 and 2010), though Li et al. (2018) has a decreasing pattern over the common years of 2013-2015, though this is less steep with the use of IER as compared to SCHIF. This difference between Li et al. (2018) and the other studies, including ours, for these years, appears to be primarily attributed to different $PM_{2.5}$ exposure estimates. They reported a higher $PM_{2.5}$ exposure than estimates from other studies in 2013, which accordingly revealed a greater reduction in

subsequent years. Despite the variations and uncertainty in death estimates across studies, there seems to be clear agreement that deaths have either increased, or, at a minimum, not decreased nearly as steeply as concentrations.

Such $PM_{2.5}$-related premature deaths can disproportionately harm populations of lower socioeconomic status (Hajat et al. 2015). Here, we examined the disparity of incidences across GDP per capita based on differences in ambient concentrations. We place this in the context of economic inequality. At the national scale, China appears to be trending toward greater economic equality, starting primarily with a steep drop in 2010. This pattern appears to agree with previous studies (Han et al. 2016a) as well as national statistics (China's National Bureau of Statistics, http://www.stats.gov.cn/), though the latter appears to show a small recent uptick. Compared to economic inequality, total premature mortality associated with $PM_{2.5}$ is distributed relatively equally across GDP per capita, though the trend towards equality is not consistent for all causes of death.

We found that GDP per capita was more related to COPD and LRI than other causes of death. This is in line with previous studies showing that COPD-related death has the strongest relationship with socioeconomic status (Pleasants et al. 2016). We show no clear association between GDP per capita and LC and IHD premature mortality attributable to ambient $PM_{2.5}$ exposure over China, which we attribute to widespread active smoking (Hiscock et al. 2012; Polak et al. 2019; Yusuf et al. 2004). Temporally, the interprovincial Ginis for different $PM_{2.5}$-related deaths show downward trends, demonstrating that the $PM_{2.5}$-related mortality risks are distributed more equally between provinces from 2005 to 2017. Muller et al. (2018) showed a similar pattern among US regions using an adjusted Gini index that accounted for $PM_{2.5}$-related premature mortality.

These findings have several implications for policymakers interested in air pollution and health equity. While policies have helped alleviate ambient pollutant concentrations, the health burden continues to rise. This burden could be alleviated through policies to prevent pollution, exposure, and disease. In particular, baseline risks of stroke and IHD lead to an increased burden from these causes (Figure B9). Conversely, COPD and LRI may disproportionately affect poorer provinces, which could warrant a more targeted intervention to address these health disparities. However, any targeted policies to address inequality warrant further specific study to account for the effect of a specific intervention using the appropriate metric (Harper et al. 2013).

This study is subject to several limitations. First, the baseline mortality rates were obtained and projected at the provincial level due to data availability, which could mask some of the inequality

revealed by the fine resolution of other data sources (including $PM_{2.5}$ exposure, population and GDP data). A long-term record of city-level mortality baselines would offer greater accuracy for both the inequality and magnitude of mortality (Maji et al. 2018b). Second, we account for only part of the total $PM_{2.5}$ related exposure and burden, neglecting indoor air pollution exposure, childhood exposure, differences in individual health effects, other potential causes of death, and morbidity (Lee et al. 2019; Lelieveld et al. 2018; Qi et al. 2017; Steinle et al. 2015). Additionally, we apply the GEMM Chinese CRF outside of the observed range of concentrations of the Chinese Male Cohort study on which it is based (15.4 to 83.7 $\mu g/m^3$), which may introduce extrapolation errors. We observed 13-year mean concentrations that exceed the maximum observed concentration of 83.7 $\mu g/m^3$, beyond which GEMM may not apply. Similarly, our counterfactual concentration of 2.4 $\mu g/m^3$ is significantly lower than the minimum observed for the Chinese Male Cohort study (15.4 $\mu g/m^3$); however, evidence from other cohorts, including those in GEMM, suggest that exposure risks remain at low concentrations. Third, we do not account for $PM_{2.5}$ characteristics (such as chemical composition, size distribution, and sources) and the confounding effects of gaseous pollutants co-varied with $PM_{2.5}$ on human health (such as ozone and nitrogen dioxide), which may also bias the mortality estimates in this study (Konishi et al. 2014; Ostro et al. 2015; Pope C. Arden et al. 2018). Fourth and finally, previous studies suggest that differences in exposure alone may represent a small fraction of the disparity in the economic impacts across income groups due to air pollution (Muller et al. 2018; Saari et al. 2017). The characteristics of the exposure, e.g., particulate composition, may be relevant (Bell and Ebisu 2012). Income, location, and insurance status may affect baseline health status, health care access, outcomes, and economic impacts (Jones et al. 2011; Schoen et al. 2013; Van Ourti et al. 2009; Viscusi and Aldy 2003; Wilper et al. 2009).

5.5 Conclusion

In recent decades, China has seen significant economic development and increasing health risks from air pollution. Here, we examine how equally these impacts are distributed across the nations and between provinces. We present $PM_{2.5}$ exposure, attributable health burdens, and corresponding environmental inequalities over China from 2005 to 2017. We find that, though $PM_{2.5}$ concentrations declined overall, the number of premature deaths attributable to $PM_{2.5}$ exposure grew. The 5-COD mortality rose from 1.39 (95%CI: 1.24, 1.52) million in 2005 to 1.82 (95%CI: 1.65, 1.98) million in 2017. Stroke and IHD were the two leading causes of deaths, contributing to approximately 36% and 34% of total cause-specific mortality during 2005-2017, respectively. These causes dominate due to

their prevalence in the population, which could be alleviated not only through environmental policy to further reduce air pollution, but also broader programs for prevention and treatment of such public health risks. More targeted programs may be warranted for poorer provinces (based on low GDP per capita), as they endure a disproportionate share of $PM_{2.5}$-related premature deaths due to COPD and LRI. Overall, total premature mortality associated with $PM_{2.5}$ is distributed relatively equally across the population regardless of GDP per capita, and has been steady or becoming more equitable over time. However, this result captures only differences in ambient concentrations, which does not reflect all differences in exposure, baseline incidence rates, vulnerability or access to care, all of which could contribute to inequality.

These findings highlight the need for formulating targeted air quality policies in China to consolidate air quality improvement and safeguard the population in the deprived areas sharing an equitable environment. Though advances in this research field are limited by inadequate data and estimation methods, our study takes a step toward achieving that goal by providing information on spatiotemporal characteristics of health burden and environmental inequality attributable to $PM_{2.5}$ exposure that can be applied to inform future research assessing impacts of $PM_{2.5}$ exposure from a comprehensive perspective.

Chapter 6
Conclusions and Recommendations

This dissertation establishes a theoretical optic-mass relationship without introducing regionally-specific fitting parameters, enabling both $PM_{2.5}$ mass concentrations and particle sizes to be estimated across various spatial and temporal domains, which makes a methodological contribution to satellite-based $PM_{2.5}$ concentration estimation. Following the established relationship, this dissertation presents the first national estimates of size-resolved $PM_{2.5}$ exposure using established theoretical and statistical models, revealing the prevalent exposure to submicron particles over China, which fills a significant gap in population-scale size-resolved observations of sub-micron atmospheric aerosols, which toxicological studies suggest may be more harmful to human health. Finally, this dissertation explores the spatiotemporal variation of $PM_{2.5}$ attributable mortality and corresponding health disparity from 2005 to 2017, suggesting that more targeted policies may be warranted for poorer provinces (i.e. with low GDP per capita), which contributes to understanding the public health burden and related disparity attributed to ambient $PM_{2.5}$ exposure over China.

The main findings and limitations are summarized in Chapters 6.1 and 6.2, respectively. Section 6.3 recommends the future directions for further research.

6.1 Summary

This dissertation has developed a theoretical optic-mass relationship through aerosol microphysical parameters in Chapter 3. This makes a methodological contribution to reveal the spatial and temporal patterns of $PM_{2.5}$ over China, including both concentrations and particle sizes. The estimates were validated against observations from AERONET. The results show that mean particle size over eastern China is smaller than that in the west, depicting a clear bifurcation across the country, especially in summertime. This finding is attributed to variations in topography, meteorology, land use and population density, which affects the properties of emitted aerosols as well as their fate and transport. A statistically significant correlation (R=0.82) was observed between estimated and measured annual $PM_{2.5}$, with the RMSE=9.25 $\mu g/m^3$, MAE=6.98 $\mu g/m^3$, MBE=−1.98 $\mu g/m^3$ and RPE=17.69% (N=1270). The spatiotemporal distributions of resulting $PM_{2.5}$ are consistent with previous findings, indicating the effectiveness and applicability of the proposed method. This method quantifies $PM_{2.5}$ mass concentrations without introducing regionally-specific fitting parameters, which can be efficiently applied across various spatial and temporal domains.

To address the need for size-resolved $PM_{2.5}$ exposure data, $PM_{2.5}$ concentrations derived from the GWR model were employed to estimate particle size using the established theoretical relationship in Chapter 4. Annual mean effective radii between 0.3 to 1.3 μm with a mean average error of 0.1μm was observed. The findings show that 1% or less of the Chinese population was exposed to annual $PM_{2.5}$ concentrations less than 10 $\mu g/m^3$ and a mean particle effective radius greater than 0.7μm (i.e. aerodynamic diameter of PM_1). Spatially, the Centre economic region had the highest annual-mean $PM_{2.5}$ exposures, where 90% of the population was exposed to concentrations higher than 50 $\mu g/m^3$ and 98% was exposed to particles with mean radius below 0.5 μm. Temporally, although the highest $PM_{2.5}$ concentrations were more likely to occur in winter, summertime was the season during which the highest percentage of the national population (86%) lived in the regions in which the fine fraction had the smallest mean particle radii (<0.5 μm). This study demonstrates the potential of remote sensing techniques to enable large-scale $PM_{2.5}$ estimation, including concentrations and sizes. The revealed prevalence of exposure to PM_1, and lack of particle size validation data, motivate further research to better understand size-resolved exposures and impacts of $PM_{2.5}$ at population scales.

To better understand the $PM_{2.5}$ pollution in China, not only large-scale $PM_{2.5}$ estimation, but also impacts on public health and environmental inequality are crucial. Chapter 5 presents the spatiotemporal variation of $PM_{2.5}$ attributable mortality and investigated the corresponding economic and environmental inequality at provincial and national levels over China from 2005 to 2017. Long-term $PM_{2.5}$ exposures over China derived from satellite-based observations and chemical transport models were employed to quantify the attributable excess premature mortality related to five causes of death using the GEMM. National and interprovincial health inequalities were characterized through environmental Lorenz curves and Gini coefficients over the study period. The results show that mortality attributable to $PM_{2.5}$ exposure increased by 31% over China from 2005 to 2017, contributing to 1.82 (95%CI: 1.65, 1.98) million premature deaths in 2017. Approximately 70% of $PM_{2.5}$ attributable deaths are caused by stroke and ischemic heart disease, though COPD and LRI have more influence in poorer provinces. While economic gains and $PM_{2.5}$-related deaths are concentrated in a few provinces, we find that both gains and health outcomes are shared more equally over time. As a nation, however, trends toward equality are more recent and less clear across causes of death. The premature mortalities attributed to $PM_{2.5}$ exposure has increased during 2005-2017 and are unevenly contributed by populations with low/middle GDP per capita over China. It is argued that strict air pollution control policies is still needed in China to alleviate the health burden and environmental inequality, especially targeting subpopulations in the developing provinces.

6.2 Limitations

A comprehensive dataset of $PM_{2.5}$ observations (including mass concentration and particle radius) is needed to establish a more robust model and to quantify the uncertainties of exposure estimates. Regarding particle radius, columnar effective radius retrieved by the AERONET operational algorithm was adopted for quantitative validation; however, in addition to limited samples, the AERONET radius retrievals cannot be considered as the ground truth data because of uncertainties caused by the algorithm assumptions (Dubovik et al. 2006; Holben et al. 2006). Accordingly, some of the difference between estimates and size retrievals from AERONET may be attributed to differences in retrieved quantities (surface vs. column) and retrieval approaches. The MODIS AE product was also used in validation and a declining pattern between radius and AE was revealed, as expected. While promising, this interpretation is qualitative, as the relationship between AE and particle effective radius is known to vary with wavelength, size distribution, and composition (Gobbi et al. 2007; Schuster et al. 2006). Therefore, to achieve a better performance, large-scale measurements on aerosol properties (such as particle radius) are still needed to improve exposure estimation and uncertainty evaluation.

Additionally, this work was conducted based on the assumption that the ground-level $PM_{2.5}$ observations, employed for model establishment and validation, are the ground truth; however, measurement errors exist. All PM concentration data in China has been measured at standard temperature and pressure (0°C, 101.325 kPa) according to China national ambient air quality standards (GB 3095-2012). The observations measured with these fixed state parameters cannot reflect the actual air quality over China. For instance, $PM_{2.5}$ pollution in the west Tibet Plateau region was overestimated using the national standard measurement approach because of low air pressure caused by high altitude. Additionally, meteorological conditions affect the deposition rate of PM. Particle size screening and mass concentration calculations are thus influenced by spatial differences in temperature and humidity between northern and southern China. To address this, beginning in 2019, the Ministry of Ecology and Environment (MEE) has revised the GB 3095-2012 standard, requiring that particulate matter and its components shall be measured at actual (local) temperature and pressure.

6.3 Recommendations for Future Research

This dissertation has demonstrated the potential of satellite data in large-scale $PM_{2.5}$ estimation and highlighted the long-term attributable health impacts and disparities. The retrieval scheme could be further improved using deep learning models to complete the methodological framework and accelerate performance.

Diverse machine learning and deep learning models have been applied in environmental remote sensing studies (Yuan et al. 2020; Kim et al. 2019; Ma et al. 2019; Snauffer et al. 2018), which extract abstract features from training samples to develop empirical relationships between environmental measurements and satellite observations. These techniques outperform traditional statistical models with remarkable accuracy and have increasingly become popular in aerosol retrievals (Fortin et al. 2011; Li 2020; Reichstein et al. 2019). The primary objective of aerosol retrieval is to obtain AOD from the top of atmosphere (TOA) reflectance by eliminating the surface contribution. Three main issues in the context of AOD retrievals are expected to be addressed by deep learning techniques.

First, AOD retrieval and bias correction. The operational algorithms of MODIS, Dark Target and Deep Blue, are the two mainstream AOD retrieval algorithms. These two algorithms are based on the fact that the surface dominates the satellite observed signal in some spectral channels and the atmosphere dominates in others. The basic principle of these algorithms for AOD retrieval is to combine the appropriate spectral bands (e.g. red and blue). However, the retrieval is still restricted by the algorithm assumptions and limited input information. As noted, deep learning techniques infer empirical relationships with promising performance, which can involve not only satellite radiance from multiple bands but also auxiliary parameters, such as angle information, cloud fraction, meteorological and topographical features. Aerosol physical properties can also be included in these models and benefit the model performance. Taylor et al. (2014) developed a neural network to retrieve not only AOD but also aerosol characteristics, such as complex refractive indices and size distribution. Therefore, it is worth considering multiple modifiers in AOD retrieval and correction using deep learning techniques to achieve better performance.

Second, AOD gap-filling. Though satellite data offer the potential to monitor large-scale air quality, their aerosol products are challenged by non-random missing values resulting from cloud and snow contamination, high surface reflectance, and misclassification (i.e. high aerosol loading can be considered as cloud under the assumption of retrieval algorithm). These missing AOD values may be responsible for bias in exposure assessment by their effect on the AOD-PM relationship. Though this dissertation adopted AOD products from two satellites (Terra and Aqua) and two algorithms (DT and DB), missing values remain in this work. Hence, filling the missing values of AOD products is necessary. In addition to developing new retrieval algorithms as mentioned above, the combination of simulation models (e.g. CTMs) and statistical models (e.g. deep neural networks) may provide a promising alternative for AOD gap-filling. This may not only relieve the computational burden caused

by numerical models, but also offer explanatory power of deep learning models. The combination may be achieved by constraining the cost function of deep neural networks with physical mechanisms or training deep neural networks with the CTM outputs.

Third, AOD downscaling. Currently, MODIS provides AOD products based on three different retrieval algorithms, with respective spatial resolutions of 10 km, 3 km, 1 km, which enable the spatial patterns of aerosol load and PM pollution to be exhibited at national or even global scales. However, the local-scale studies, which are significant for monitoring pollutions attributed to traffic and industrial emissions, are limited by the relatively low spatial resolution of MODIS products. Downscaling is a significant procedure for weather and climate applications, which aims to convert the large-scale low-resolution (including both spatial and temporal scales) data into small-scale and high-resolution products (Chen et al., 2019). Deep learning models have been explored to downscale geospatial data, showing better performance than traditional statistical models (Alexakis and Tsanis 2016; Baño-Medina et al. 2019; Ducournau and Fablet 2016; Vandal et al. 2017). However, these techniques have rarely been applied to obtain high-resolution AOD data. Therefore, the application of deep learning to this issue can be a topic worth investigating.

Deep learning techniques can also be applied in $PM_{2.5}$ exposure estimation, from either satellite AOD observation or TOA reflectance. T. Li et al. (2017) incorporated geographical autocorrelation into an intelligent deep learning framework (i.e. deep belief network) to estimate $PM_{2.5}$ concentrations using satellite AOD observations and auxiliary data. The result shows that the developed models outperformed the traditional neural network. Shen et al. (2018) retrieved ground-level $PM_{2.5}$ concentrations directly from satellite TOA reflectance, which may avoid the bias caused by the AOD retrieval process. The attempt to retrieve $PM_{2.5}$ directly from TOA reflectance also enables more satellite observations (with various resolutions) to be applied in $PM_{2.5}$ retrieval studies. Hence, the application of deep learning for large-scale $PM_{2.5}$ retrieval deserves further attention, which allows multiple datasets (such as socioeconomic, meteorological and remote sensing data) and numerical model outputs to be integrated within one framework.

In addition to methodological recommendations, further work is needed to understand the full intersections between size-resolved $PM_{2.5}$ exposure and attributable health outcomes from epidemiological perspectives. Though national particle radius of $PM_{2.5}$ has been quantified in this dissertation, the health impacts of size-resolved $PM_{2.5}$ exposure are difficult to assess due to the dearth of size-related exposure-response relationships.

References

Abdou WA, Diner DJ, Martonchik JV, Bruegge CJ, Kahn RA, Gaitley BJ, et al. 2005. Comparison of coincident Multiangle Imaging Spectroradiometer and Moderate Resolution Imaging Spectroradiometer aerosol optical depths over land and ocean scenes containing Aerosol Robotic Network sites. J Geophys Res-Atmospheres 110; doi:10.1029/2004jd004693.

Alexakis DD, Tsanis IK. 2016. Comparison of multiple linear regression and artificial neural network models for downscaling TRMM precipitation products using MODIS data. Environ Earth Sci 75:1077; doi:10.1007/s12665-016-5883-z.

Anderson JC, Wang J, Zeng J, Leptoukh G, Petrenko M, Ichoku C, et al. 2013. Long-term statistical assessment of Aqua-MODIS aerosol optical depth over coastal regions: bias characteristics and uncertainty sources. Tellus B Chem Phys Meteorol 65:20805; doi:10.3402/tellusb.v65i0.20805.

Apte JS, Marshall JD, Cohen AJ, Brauer M. 2015. Addressing global mortality from ambient $PM_{2.5}$. Environ Sci Technol 49:8057–8066; doi:10.1021/acs.est.5b01236.

Azimi M, Feng F, Zhou C. 2019. Air pollution inequality and health inequality in China: An empirical study. Environ Sci Pollut Res 26:11962–11974; doi:10.1007/s11356-019-04599-z.

Baars H, Ansmann A, Althausen D, Engelmann R, Heese B, Müller D, et al. 2012. Aerosol profiling with lidar in the Amazon Basin during the wet and dry season. J Geophys Res Atmospheres 117; doi:10.1029/2012JD018338.

Baño-Medina J, Manzanas R, Gutiérrez JM. 2019. Configuration and intercomparison of deep learning neural models for statistical downscaling. Geosci Model Dev Discuss 1–20; doi:https://doi.org/10.5194/gmd-2019-278.

Bell ML, Ebisu K. 2012. Environmental inequality in exposures to airborne particulate matter components in the United States. Env Health Perspect 120:1699–704; doi:10.1289/ehp.1205201.

Belsley DA, Kuh E, Welsch RE. 2005. *Regression Diagnostics: Identifying Influential Data and Sources of Collinearity*. John Wiley & Sons.

Brauer M, Amann M, Burnett RT, Cohen A, Dentener F, Ezzati M, et al. 2012. Exposure assessment for estimation of the global burden of disease attributable to outdoor air pollution. Environ Sci Technol 46:652–660; doi:10.1021/es2025752.

Burnett R, Chen H, Szyszkowicz M, Fann N, Hubbell B, Pope CA, et al. 2018. Global estimates of mortality associated with long-term exposure to outdoor fine particulate matter. Proc Natl Acad Sci 115:9592–9597; doi:10.1073/pnas.1803222115.

Chen D, Tian J. 2010. Monitoring spatial and temporal variability of air quality using satellite observation data: A case study of MODIS-observed aerosols in southern Ontario, Canada. Air Qual; doi:10.5772/9753.

Chen G, Li S, Zhang Y, Zhang W, Li D, Wei X, et al. 2017. Effects of ambient PM_1 air pollution on daily emergency hospital visits in China: an epidemiological study. Lancet Planet Health 1:e221–e229; doi:10.1016/S2542-5196(17)30100-6.

Chen G, Morawska L, Zhang W, Li S, Cao W, Ren H, et al. 2018. Spatiotemporal variation of PM_1 pollution in China. Atmos Environ 178:198–205; doi:10.1016/j.atmosenv.2018.01.053.

Chen J, Zhao CS, Ma N, Yan P. 2014a. Aerosol hygroscopicity parameter derived from the light scattering enhancement factor measurements in the North China Plain. Atmospheric Chem Phys 14:8105–8118; doi:10.5194/acp-14-8105-2014.

Chen L, Liu C, Zou R, Yang M, Zhang Z. 2016. Experimental examination of effectiveness of vegetation as bio-filter of particulate matters in the urban environment. Environ Pollut 208:198–208; doi:10.1016/j.envpol.2015.09.006.

Chen Y, Li Q, Kahn RA, Randerson JT, Diner DJ. 2009. Quantifying aerosol direct radiative effect with Multiangle Imaging Spectroradiometer observations: Top-of-atmosphere albedo change by aerosols based on land surface types. J Geophys Res Atmospheres 114; doi:10.1029/2008JD010754.

Chen Y, Schleicher N, Chen Y, Chai F, Norra S. 2014b. The influence of governmental mitigation measures on contamination characteristics of $PM_{2.5}$ in Beijing. Sci Total Environ 490: 647–658.

Chen Y, Xie S, Luo B, Zhai C. 2019. Characteristics and sources of water-soluble ions in $PM_{2.5}$ in the Sichuan Basin, china. Atmosphere 10: 78.

Chen Y, Zhao P, He D, Dong F, Zhao X, Zhang X. 2015. Characteristics and parameterization for atmospheric extinction coefficient in Beijing. Environ Sci 36: 3582–3589.

Chu Y, Liu Y, Li X, Liu Z, Lu H, Lu Y, et al. 2016. A review on predicting ground $PM_{2.5}$ concentration using satellite aerosol optical depth. Atmosphere 7:129; doi:10.3390/atmos7100129.

Chubarova NY, Poliukhov AA, Gorlova ID. 2016. Long-term variability of aerosol optical thickness in Eastern Europe over 2001-2014 according to the measurements at the Moscow MSU MO AERONET site with additional cloud and NO_2 correction. Atmospheric Meas Tech 9:313–334; doi:https://doi.org/10.5194/amt-9-313-2016.

Clarisse L, Hurtmans D, Prata AJ, Karagulian F, Clerbaux C, Mazière MD, et al. 2010. Retrieving radius, concentration, optical depth, and mass of different types of aerosols from high-resolution infrared nadir spectra. Appl Opt 49:3713–3722; doi:10.1364/AO.49.003713.

Clark LP, Millet DB, Marshall JD. 2014. National patterns in environmental injustice and inequality: outdoor NO_2 air pollution in the United States. PLoS ONE 9: e94431; .

Cohen AJ, Brauer M, Burnett R, Anderson HR, Frostad J, Estep K, et al. 2017. Estimates and 25-year trends of the global burden of disease attributable to ambient air pollution: an analysis of data from the Global Burden of Diseases Study 2015. Lancet 389:1907–1918; doi:10.1016/S0140-6736(17)30505-6.

Day MC, Pandis SN. 2011. Predicted changes in summertime organic aerosol concentrations due to increased temperatures. Atmos Environ 45:6546–6556; doi:10.1016/j.atmosenv.2011.08.028.

De Haar C, Hassing I, Bol M, Bleumink R, Pieters R. 2006. Ultrafine but not fine particulate matter causes airway inflammation and allergic airway sensitization to co-administered antigen in mice. Clin Exp Allergy 36: 1469–1479.

de Hartog JJ, Lanki T, Timonen KL, Hoek G, Janssen NAH, Ibald-Mulli A, et al. 2009. Associations between $PM_{2.5}$ and heart rate variability are modified by particle composition and beta-blocker use in patients with coronary heart disease. Environ Health Perspect 117:105–111; doi:10.1289/ehp.11062.

Delfino RJ, Sioutas C, Malik S. 2005. Potential role of ultrafine particles in associations between airborne particle mass and cardiovascular health. Environ Health Perspect 113:934–946; doi:10.1289/ehp.7938.

Deng C, Zhuang G, Huang K, Li J, Zhang R, Wang Q, et al. 2011. Chemical characterization of aerosols at the summit of Mountain Tai in Central East China. Atmos Chem Phys 11: 7319–7332.

Deroubaix A, Menut L, Flamant C, Brito J, Denjean C, Dreiling V, et al. 2019. Diurnal cycle of coastal anthropogenic pollutant transport over southern West Africa during the DACCIWA campaign. Atmos Chem Phys 19:473–497; doi:https://doi.org/10.5194/acp-19-473-2019.

Di Q, Koutrakis P, Schwartz J. 2016. A hybrid prediction model for $PM_{2.5}$ mass and components using a chemical transport model and land use regression. Atmos Environ 131:390–399; doi:10.1016/j.atmosenv.2016.02.002.

Ding A, Wang T, Zhao M, Wang T, Li Z. 2004. Simulation of sea-land breezes and a discussion of their implications on the transport of air pollution during a multi-day ozone episode in the Pearl River Delta of China. Atmos Environ 38:6737–6750; doi:10.1016/j.atmosenv.2004.09.017.

Dubovik O, Sinyuk A, Lapyonok T, Holben BN, Mishchenko M, Yang P, et al. 2006. Application of spheroid models to account for aerosol particle nonsphericity in remote sensing of desert dust. J Geophys Res Atmos 111; doi:10.1029/2005JD006619.

Ducournau A, Fablet R. 2016. Deep learning for ocean remote sensing: an application of convolutional neural networks for super-resolution on satellite-derived SST data. 9th IAPR Workshop Pattern Recogniton Remote Sens; doi:10.1109/PRRS.2016.7867019.

Esposito V, Lucariello A, Savarese L, Cinelli MP, Ferraraccio F, Bianco A, et al. 2012. Morphology changes in human lung epithelial cells after exposure to diesel exhaust micron sub particles ($PM_{1.0}$) and pollen allergens. Environ Pollut 171:162–167; doi:10.1016/j.envpol.2012.07.006.

Fang D, Wang Q, Li H, Yu Y, Lu Y, Qian X. 2016. Mortality effects assessment of ambient $PM_{2.5}$ pollution in the 74 leading cities of China. Sci Total Environ 569–570:1545–1552; doi:10.1016/j.scitotenv.2016.06.248.

Fang P, Dong S, Xiao J, Liu C, Feng X, Wang Y. 2010. Regional inequality in health and its determinants: Evidence from China. Health Policy 94:14–25; doi:10.1016/j.healthpol.2009.08.002.

Fann N, Coffman E, Timin B, Kelly JT. 2018. The estimated change in the level and distribution of $PM_{2.5}$-attributable health impacts in the United States: 2005–2014. Environ Res 167:506–514; doi:10.1016/j.envres.2018.08.018.

Feng L, Ye B, Feng H, Ren F, Huang S, Zhang X, et al. 2017. Spatiotemporal changes in fine particulate matter pollution and the associated mortality burden in China between 2015 and 2016. Int J Environ Res Public Health 14:1321; doi:10.3390/ijerph14111321.

Feng Y, Chen D, Ouyang X, Zhang X. 2018. Variability of satellite-based total aerosols and the relationship with emission, meteorology and landscape in North China during 2000–2016. Environ Earth Sci 77:499; doi:10.1007/s12665-018-7685-y.

Fortin JG, Anctil F, Parent L-É, Bolinder MA. 2011. Site-specific early season potato yield forecast by neural network in Eastern Canada. Precis Agric 12:905–923; doi:10.1007/s11119-011-9233-6.

Fu J, Jiang D, Huang Y, 2014. 1 km grid population dataset of China (2005, 2010). Acta Geographica Sinica 69: 136-139; doi: 10.11821/dlxb2014S006.

Franck U, Odeh S, Wiedensohler A, Wehner B, Herbarth O. 2011. The effect of particle size on cardiovascular disorders — The smaller the worse. Sci Total Environ 409:4217–4221; doi:10.1016/j.scitotenv.2011.05.049.

Gastwirth JL, Glauberman M. 1976. The interpolation of the Lorenz curve and Gini index from grouped data. Econometrica 44:479–483; doi:10.2307/1913977.

Geng F, Hua J, Mu Z, Peng L, Xu X, Chen R, et al. 2013. Differentiating the associations of black carbon and fine particle with daily mortality in a Chinese city. Environ Res 120: 27–32.

Geng G, Zhang Q, Martin RV, van Donkelaar A, Huo H, Che H, et al. 2015. Estimating long-term $PM_{2.5}$ concentrations in China using satellite-based aerosol optical depth and a chemical transport model. Remote Sens Environ 166:262–270; doi:10.1016/j.rse.2015.05.016.

Gerlofs-Nijland ME, Rummelhard M, Boere AJF, Leseman DLAC, Duffin R, Schins RPF, et al. 2009. Particle induced toxicity in relation to transition metal and polycyclic aromatic hydrocarbon contents. Environ Sci Technol 43:4729–4736; doi:10.1021/es803176k.

Giannadaki D, Lelieveld J, Pozzer A. 2016. Implementing the US air quality standard for $PM_{2.5}$ worldwide can prevent millions of premature deaths per year. Environ Health 15:88; doi:10.1186/s12940-016-0170-8.

Giannakaki E, Zyl PG van, Müller D, Balis D, Komppula M. 2016. Optical and microphysical characterization of aerosol layers over South Africa by means of multi-wavelength depolarization and Raman lidar measurements. Atmos Chem Phys 16:8109–8123; doi:https://doi.org/10.5194/acp-16-8109-2016.

Gobbi GP, Kaufman YJ, Koren I, Eck TF. 2007. Classification of aerosol properties derived from AERONET direct sun data. Atmos Chem Phys 7:453–458; doi:https://doi.org/10.5194/acp-7-453-2007.

Gulliver J, Briggs DJ. 2007. Journey-time exposure to particulate air pollution. Atmos Environ 41:7195–7207; doi:10.1016/j.atmosenv.2007.05.023.

Guo J, Gu X, Yu T, Cheng T, Chen H. 2014. Trend analysis of the aerosol optical depth from fusion of MISR and MODIS retrievals over China. IOP Conf Ser Earth Environ Sci 17:012036; doi:10.1088/1755-1315/17/1/012036.

Guo J, Xia F, Zhang Y, Liu H, Li J, Lou M, et al. 2017a. Impact of diurnal variability and meteorological factors on the $PM_{2.5}$ - AOD relationship: Implications for $PM_{2.5}$ remote sensing. Environ Pollut 221:94–104; doi:10.1016/j.envpol.2016.11.043.

Guo Y, Tang Q, Gong D-Y, Zhang Z. 2017b. Estimating ground-level $PM_{2.5}$ concentrations in Beijing using a satellite-based geographically and temporally weighted regression model. Remote Sens Environ 198:140–149; doi:10.1016/j.rse.2017.06.001.

Gupta P, Christopher SA. 2009. Particulate matter air quality assessment using integrated surface, satellite, and meteorological products: 2. A neural network approach. J Geophys Res Atmospheres 114; doi:10.1029/2008JD011497.

Gupta P, Christopher SA, Wang J, Gehrig R, Lee Y, Kumar N. 2006. Satellite remote sensing of particulate matter and air quality assessment over global cities. Atmos Environ 40:5880–5892; doi:10.1016/j.atmosenv.2006.03.016.

Hajat A, Hsia C, O'Neill MS. 2015. Socioeconomic disparities and air pollution exposure: A global review. Curr Environ Health Rep 2:440–450; doi:10.1007/s40572-015-0069-5.

Han J, Zhao Q, Zhang M. 2016a. China's income inequality in the global context. Perspect Sci 7:24–29; doi:10.1016/j.pisc.2015.11.006.

Han L, Zhou W, Li W. 2016b. Fine particulate ($PM_{2.5}$) dynamics during rapid urbanization in Beijing, 1973-2013. Sci Rep 6:23604; doi:10.1038/srep23604.

Hand JL, Kreidenweis SM. 2002. A new method for retrieving particle refractive index and effective density from aerosol size distribution data. Aerosol Sci Technol 36:1012–1026; doi:10.1080/02786820290092276.

Hansen J E TLD. 1974. Light scattering in planetary atmospheres. Space Sci Rev 16: 527–610.

Hao Y, Liu Y-M. 2016. The influential factors of urban $PM_{2.5}$ concentrations in China: A spatial econometric analysis. J Clean Prod 112:1443–1453; doi:10.1016/j.jclepro.2015.05.005.

Harper S, Ruder E, Roman HA, Geggel A, Nweke O, Payne-Sturges D, et al. 2013. Using inequality measures to incorporate environmental justice into regulatory analyses. Int J Environ Res Public Health 10:4039–4059; doi:10.3390/ijerph10094039.

Hatzianastassiou N, Matsoukas C, Drakakis E, Stackhouse Jr. PW, Koepke P, Fotiadi A, et al. 2007. The direct effect of aerosols on solar radiation based on satellite observations, reanalysis datasets, and spectral aerosol optical properties from Global Aerosol Data Set (GADS). Atmospheric Chem Phys 7:2585–2599; doi:https://doi.org/10.5194/acp-7-2585-2007.

He P, Yang X, Shen X, Chen D. 2010. Analysis on characteristics of ambient air $PM_{2.5}$ pollution in Baoshan District of Shanghai. J Environ Occup Med 27: 724–726.

He Q, Huang B. 2018. Satellite-based mapping of daily high-resolution ground $PM_{2.5}$ in China via space-time regression modeling. Remote Sens Environ 206:72–83; doi:10.1016/j.rse.2017.12.018.

Hilboll A, Richter A, Burrows JP. 2013. Long-term changes of tropospheric NO_2 over megacities derived from multiple satellite instruments. Atmospheric Chem Phys 13:4145–4169; doi:https://doi.org/10.5194/acp-13-4145-2013.

Hiscock R, Bauld L, Amos A, Fidler JA, Munafò M. 2012. Socioeconomic status and smoking: A review. Ann N Y Acad Sci 1248:107–123; doi:10.1111/j.1749-6632.2011.06202.x.

Hobbs PV, Radke LF, Lyons JH, Ferek RJ, Coffman DJ, Casadevall TJ. 1991. Airborne measurements of particle and gas emissions from the 1990 volcanic eruptions of Mount Redoubt. J Geophys Res Atmospheres 96:18735–18752; doi:10.1029/91JD01635.

Hoek G, Boogaard H, Knol A, De Hartog J, Slottje P, Ayres JG, et al. 2009. Concentration response functions for ultrafine particles and all-cause mortality and hospital admissions: results of a European expert panel elicitation. Environ Sci Technol 44: 476–482.

Hofmann DJ, Rosen JM. 1983. Sulfuric acid droplet formation and growth in the stratosphere after the 1982 eruption of El Chichón. Science 222:325–327; doi:10.1126/science.222.4621.325.

Holben BN, Eck TF, Slutsker I, Smirnov A, Sinyuk A, Schafer J, et al. 2006. Aeronet's Version 2.0 quality assurance criteria. SPIE Asia-Pacific Remote Sensing; doi:10.1117/12.706524.

Holben BN, Eck TF, Slutsker I, Tanré D, Buis JP, Setzer A, et al. 1998. AERONET—A federated instrument network and data archive for aerosol characterization. Remote Sens Environ 66:1–16; doi:10.1016/S0034-4257(98)00031-5.

Hong S, Jiao L, Ma W. 2013. Variation of $PM_{2.5}$ concentration in Hangzhou, China. Particuology 11: 55–62.

Hsu NC, Jeong M-J, Bettenhausen C, Sayer AM, Hansell R, Seftor CS, et al. 2013. Enhanced Deep Blue aerosol retrieval algorithm: The second generation. J Geophys Res Atmospheres 118:9296–9315; doi:10.1002/jgrd.50712.

Hu HY. 1935. The distribution of population in China, with statistics and maps. Acta Geogr Sin 2:33–74; doi:10.11821/xb193502002.

Hu J, Huang L, Chen M, Liao H, Zhang H, Wang S, et al. 2017a. Premature mortality attributable to particulate matter in China: Source contributions and responses to reductions. Environ Sci Technol 51:9950–9959; doi:10.1021/acs.est.7b03193.

Hu K, Guo Y, Hu D, Du R, Yang X, Zhong J, et al. 2018. Mortality burden attributable to PM_1 in Zhejiang province, China. Environ Int 121:515–522; doi:10.1016/j.envint.2018.09.033.

Hu X, Belle JH, Meng X, Wildani A, Waller LA, Strickland MJ, et al. 2017b. Estimating $PM_{2.5}$ concentrations in the conterminous United States using the random forest approach. Environ Sci Technol 51:6936–6944; doi:10.1021/acs.est.7b01210.

Hu X, Waller LA, Lyapustin A, Wang Y, Al-Hamdan MZ, Crosson WL, et al. 2014a. Estimating ground-level $PM_{2.5}$ concentrations in the Southeastern United States using MAIAC AOD retrievals and a two-stage model. Remote Sens Environ 140:220–232; doi:10.1016/j.rse.2013.08.032.

Hu X, Waller LA, Lyapustin A, Wang Y, Liu Y. 2014b. 10-year spatial and temporal trends of $PM_{2.5}$ concentrations in the southeastern US estimated using high-resolution satellite data. Atmospheric Chem Phys 14:6301–6314; doi:10.5194/acp-14-6301-2014.

Huang G, Zhou W, Qian Y, Fisher B. 2019. Breathing the same air? Socioeconomic disparities in $PM_{2.5}$ exposure and the potential benefits from air filtration. Sci Total Environ 657:619–626; doi:10.1016/j.scitotenv.2018.11.428.

Huang H, Cao J, Zeng B. 2010. Characterization of organic carbon, elemental carbon and water-soluble organic carbon in $PM_{2.5}$ of Guangzhou City. J Anal Sci 26: 255–260.

Huang J, Minnis P, Chen B, Huang Z, Liu Z, Zhao Q, et al. 2008. Long-range transport and vertical structure of Asian dust from CALIPSO and surface measurements during PACDEX. J Geophys Res Atmospheres 113; doi:10.1029/2008JD010620.

Huang R-J, Zhang Y, Bozzetti C, Ho K-F, Cao J-J, Han Y, et al. 2014. High secondary aerosol contribution to particulate pollution during haze events in China. Nature 514:218–222; doi:10.1038/nature13774.

Jiang M, Sun W, Yang G, Zhang D. 2017. Modelling seasonal GWR of daily $PM_{2.5}$ with proper auxiliary variables for the Yangtze River Delta. Remote Sens 9:346; doi:10.3390/rs9040346.

Jones AM, Rice N, Robone S, Dias PR. 2011. Inequality and polarisation in health systems' responsiveness: A cross-country analysis. J Health Econ 30:616–625; doi:10.1016/j.jhealeco.2011.05.003.

Kalnay E, Kanamitsu M, Kistler R, Collins W, Deaven D, Gandin L, et al. 1996. The NCEP/NCAR 40-year reanalysis project. Bull Am Meteorol Soc 77:437–472; doi:10.1175/1520-0477(1996)077<0437:TNYRP>2.0.CO;2.

Kan H, London SJ, Chen G, Zhang Y, Song G, Zhao N, et al. 2007. Differentiating the effects of fine and coarse particles on daily mortality in Shanghai, China. Environ Int 33: 376–384.

Kaufman YJ, Haywood JM, Hobbs PV, Hart W, Kleidman R, Schmid B. 2003. Remote sensing of vertical distributions of smoke aerosol off the coast of Africa. Geophys Res Lett 30; doi:10.1029/2003GL017068.

Kaufman YJ, Tanre D, Remer LA, Vermote EF, Chu A, Holben BN. 1997. Operational remote sensing of tropospheric aerosol over land from EOS Moderate Resolution Imaging Spectroradiometer. J Geophys Res-Atmospheres 102:17051–17067; doi:10.1029/96jd03988.

Kessner AL, Wang J, Levy RC, Colarco PR. 2013. Remote sensing of surface visibility from space: A look at the United States East Coast. Atmos Environ 81:136–147; doi:10.1016/j.atmosenv.2013.08.050.

Kim N, Ha K-J, Park N-W, Cho J, Hong S, Lee Y-W. 2019. A comparison between major artificial intelligence models for crop yield prediction: Case study of the midwestern United States, 2006–2015. ISPRS Int J Geo-Inf 8:240; doi:10.3390/ijgi8050240.

Knibbs LD, van Donkelaar A, Martin RV, Bechle MJ, Brauer M, Cohen DD, et al. 2018. Satellite-based land-use regression for continental-scale long-term ambient $PM_{2.5}$ exposure assessment in Australia. Environ Sci Technol 52:12445–12455; doi:10.1021/acs.est.8b02328.

Kodros JK, Cucinotta R, Ridley DA, Wiedinmyer C, Pierce JR. 2016. The aerosol radiative effects of uncontrolled combustion of domestic waste. Atmospheric Chem Phys 16:6771–6784; doi:https://doi.org/10.5194/acp-16-6771-2016.

Kodros JK, Pierce JR. 2017. Important global and regional differences in aerosol cloud-albedo effect estimates between simulations with and without prognostic aerosol microphysics. J Geophys Res Atmospheres 122:4003–4018; doi:10.1002/2016JD025886.

Kodros JK, Volckens J, Jathar SH, Pierce JR. 2018. Ambient particulate matter size distributions drive regional and global variability in particle deposition in the respiratory tract. Geohealth 2:298–312; doi:10.1029/2018gh000145.

Koelemeijer RBA, Homan CD, Matthijsen J. 2006. Comparison of spatial and temporal variations of aerosol optical thickness and particulate matter over Europe. Atmos Environ 40:5304–5315; doi:10.1016/j.atmosenv.2006.04.044.

Konishi S, Ng CFS, Stickley A, Nishihata S, Shinsugi C, Ueda K, et al. 2014. Particulate matter modifies the association between airborne pollen and daily medical consultations for pollinosis in Tokyo. Sci Total Environ 499:125–132; doi:10.1016/j.scitotenv.2014.08.045.

Koschmieder H. 1924. Theorie der horizontalen sichtweite. Beitrage Zur Phys Freien Atmosphare 33–53.

Kuang BY, Lin P, Huang XHH, Yu JZ. 2015. Sources of humic-like substances in the Pearl River Delta, China: positive matrix factorization analysis of $PM_{2.5}$ major components and source markers. Atmospheric Chem Phys 15:1995–2008; doi: 10.5194/acp-15-1995-2015.

Kumar N, Chu A, Foster A. 2007. An empirical relationship between $PM_{2.5}$ and aerosol optical depth in Delhi Metropolitan. Atmos Environ 41:4492–4503; doi:10.1016/j.atmosenv.2007.01.046.

Kumar P, Morawska L, Martani C, Biskos G, Neophytou M, Di Sabatino S, et al. 2015. The rise of low-cost sensing for managing air pollution in cities. Environ Int 75:199–205; doi:10.1016/j.envint.2014.11.019.

Larkin A, Geddes JA, Martin RV, Xiao Q, Liu Y, Marshall JD, et al. 2017. Global land use regression model for nitrogen dioxide air pollution. Environ Sci Technol 51:6957–6964; doi:10.1021/acs.est.7b01148.

Lee HJ, Liu Y, Coull BA, Schwartz J, Koutrakis P. 2011. A novel calibration approach of MODIS AOD data to predict PM $_{2.5}$ concentrations. Atmospheric Chem Phys 11: 9769-9795; doi:10.5194/acp-11-7991-2011.

Lee M, Schwartz J, Wang Y, Dominici F, Zanobetti A. 2019. Long-term effect of fine particulate matter on hospitalization with dementia. Environ Pollut 254:112926; doi:10.1016/j.envpol.2019.07.094.

Lelieveld J, Evans JS, Fnais M, Giannadaki D, Pozzer A. 2015. The contribution of outdoor air pollution sources to premature mortality on a global scale. Nature 525:367–371; doi:10.1038/nature15371.

Lelieveld J, Haines A, Pozzer A. 2018. Age-dependent health risk from ambient air pollution: a modelling and data analysis of childhood mortality in middle-income and low-income countries. Lancet Planet Health 2:e292–e300; doi:10.1016/S2542-5196(18)30147-5.

Levy RC, Remer LA, Mattoo S, Vermote EF, Kaufman YJ. 2007. Second-generation operational algorithm: Retrieval of aerosol properties over land from inversion of Moderate Resolution Imaging Spectroradiometer spectral reflectance. J Geophys Res Atmospheres 112; doi:10.1029/2006JD007811.

Li J, Han X, Jin M, Zhang X, Wang S. 2019. Globally analyzing spatiotemporal trends of anthropogenic $PM_{2.5}$ concentration and population's $PM_{2.5}$ exposure from 1998 to 2016. Environ Int 128:46–62; doi:10.1016/j.envint.2019.04.026.

Li J, Liu H, Lv Z, Zhao R, Deng F, Wang C, et al. 2018a. Estimation of $PM_{2.5}$ mortality burden in China with new exposure estimation and local concentration-response function. Environ Pollut 243:1710–1718; doi:10.1016/j.envpol.2018.09.089.

Li J, Liu H, Lv Z, Zhao R, Deng F, Wang C, et al. 2018b. Estimation of $PM_{2.5}$ mortality burden in China with new exposure estimation and local concentration-response function. Environ Pollut 243:1710–1718; doi:10.1016/j.envpol.2018.09.089.

Li L. 2020. A robust deep learning approach for spatiotemporal estimation of satellite AOD and $PM_{2.5}$. Remote Sens 12:264; doi:10.3390/rs12020264.

Li L, Yang J, Wang Y. 2014. An improved dark object method to retrieve 500m-resolution AOT (Aerosol Optical Thickness) image from MODIS data: A case study in the Pearl River Delta area, China. ISPRS J Photogramm Remote Sens 89:1–12; doi:10.1016/j.isprsjprs.2013.12.008.

Li S, Sicular T. 2014. The distribution of household income in china: Inequality, poverty and policies. China Q 217:1–41; doi:10.1017/S0305741014000290.

Li T, Liu Y, Zhu Q, Xu W, Yao D, Ding H. 2013. Analysis of fine particulate near 134 the transportation routes in Guangzhou City. Res Environ Sci 26: 935–941.

Li T, Shen H, Yuan Q, Zhang X, Zhang L. 2017a. Estimating ground-level $PM_{2.5}$ by fusing satellite and station observations: A geo-intelligent deep learning approach. Geophys Res Lett 44:11,985-11,993; doi:10.1002/2017GL075710.

Li X, SHENG L, XU H, QU W. 2012. Element compositions and source of $PM_{2.5}$ aerosols in Qingdao [J]. Environ Sci 5.

Li XK, Zhang CR, Li WD, Liu K. 2017b. Evaluating the use of DMSP/OLS nighttime light imagery in predicting $PM_{2.5}$ concentrations in the Northeastern United States. Remote Sens 9; doi:10.3390/rs9060620.

Li Y, Chen Q, Zhao H, Wang L, Tao R. 2015. Variations in PM_{10}, $PM_{2.5}$ and $PM_{1.0}$ in an urban area of the Sichuan Basin and their relation to meteorological factors. Atmosphere 6:150–163; doi:10.3390/atmos6010150.

Li Y, Xue Y, Guang J, She L, Fan C, Chen G. 2018c. Ground-level $PM_{2.5}$ concentration estimation from satellite data in the Beijing area using a specific particle swarm extinction mass conversion algorithm. Remote Sens 10; doi:10.3390/rs10121906.

Li ZQ, Zhang Y, Shao J, Li BS, Hong J, Liu D, et al. 2016. Remote sensing of atmospheric particulate mass of dry $PM_{2.5}$ near the ground: Method validation using ground-based measurements. Remote Sens Environ 173:59–68; doi:10.1016/j.rse.2015.11.019.

Lim SS, Vos T, Flaxman AD, Danaei G, Shibuya K, Adair-Rohani H, et al. 2012. A comparative risk assessment of burden of disease and injury attributable to 67 risk factors and risk factor clusters in 21 regions, 1990–2010: A systematic analysis for the Global Burden of Disease Study 2010. The Lancet 380:2224–2260; doi:10.1016/S0140-6736(12)61766-8.

Lin C, Li Y, Yuan Z, Lau AKH, Li C, Fung JCH. 2015. Using satellite remote sensing data to estimate the high-resolution distribution of ground-level $PM_{2.5}$. Remote Sens Environ 156:117–128; doi:10.1016/j.rse.2014.09.015.

Lin CQ, Liu G, Lau AKH, Li Y, Li CC, Fung JCH, et al. 2018. High-resolution satellite remote sensing of provincial $PM_{2.5}$ trends in China from 2001 to 2015. Atmos Environ 180:110–116; doi:10.1016/j.atmosenv.2018.02.045.

Lin H, Tao J, Du Y, Liu T, Qian Z, Tian L, et al. 2016. Particle size and chemical constituents of ambient particulate pollution associated with cardiovascular mortality in Guangzhou, China. Environ Pollut 208:758–766; doi:10.1016/j.envpol.2015.10.056.

Liu J, Han Y, Tang X, Zhu J, Zhu T. 2016. Estimating adult mortality attributable to $PM_{2.5}$ exposure in China with assimilated $PM_{2.5}$ concentrations based on a ground monitoring network. Sci Total Environ 568:1253–1262; doi:10.1016/j.scitotenv.2016.05.165.

Liu J, Li J, Zhang Y, Liu D, Ding P, Shen C, et al. 2014. Source apportionment using radiocarbon and organic tracers for $PM_{2.5}$ carbonaceous aerosols in Guangzhou, South China: Contrasting local- and regional-scale haze events. Environ Sci Technol 48:12002–12011; doi:10.1021/es503102w.

Liu M, Huang Y, Jin Z, Ma Z, Liu X, Zhang B, et al. 2017a. The nexus between urbanization and $PM_{2.5}$ related mortality in China. Environ Pollut 227:15–23; doi:10.1016/j.envpol.2017.04.049.

Liu M, Huang Y, Ma Z, Jin Z, Liu X, Wang H, et al. 2017b. Spatial and temporal trends in the mortality burden of air pollution in China: 2004–2012. Environ Int 98:75–81; doi:10.1016/j.envint.2016.10.003.

Liu M, Zhou G, Saari RK, Li J. 2019a. Long-term trend of ground-level $PM_{2.5}$ concentrations over 2012-2017 in China. IGARSS 2019 - 2019 IEEE Int Geosci Remote Sens Symp 7842–7845; doi:10.1109/IGARSS.2019.8900405.

Liu M, Zhou G, Saari RK, Li S, Liu X, Li J. 2019b. Quantifying $PM_{2.5}$ mass concentration and particle radius using satellite data and an optical-mass conversion algorithm. ISPRS J Photogramm Remote Sens 158:90–98; doi:10.1016/j.isprsjprs.2019.10.010.

Liu X, Cheng Y, Zhang Y, Jung J, Sugimoto N, Chang S-Y, et al. 2008. Influences of relative humidity and particle chemical composition on aerosol scattering properties during the 2006 PRD campaign. Atmos Environ 42:1525–1536; doi:10.1016/j.atmosenv.2007.10.077.

Liu Y, Franklin M, Kahn R, Koutrakis P. 2007. Using aerosol optical thickness to predict ground-level $PM_{2.5}$ concentrations in the St. Louis area: A comparison between MISR and MODIS. Remote Sens Environ 107:33–44; doi:10.1016/j.rse.2006.05.022.

Liu Y, He K, Li S, Wang Z, Christiani DC, Koutrakis P. 2012. A statistical model to evaluate the effectiveness of $PM_{2.5}$ emissions control during the Beijing 2008 Olympic Games. Environ Int 44:100–105; doi:10.1016/j.envint.2012.02.003.

Liu Y, Paciorek CJ, Koutrakis P. 2009. Estimating regional spatial and temporal variability of $PM_{2.5}$ concentrations using satellite data, meteorology, and land use information. Environ Health Perspect 117:886–892; doi:10.1289/ehp.0800123.

Liu Y, Sarnat JA, Kilaru V, Jacob DJ, Koutrakis P. 2005. Estimating ground-level $PM_{2.5}$ in the Eastern United States using satellite remote sensing. Environ Sci Technol 39:3269–3278; doi:10.1021/es049352m.

Liu Z, Hu B, Ji D, Wang Y, Wang M, Wang Y. 2015a. Diurnal and seasonal variation of the $PM_{2.5}$ apparent particle density in Beijing, China. Atmos Environ 120:328–338; doi:10.1016/j.atmosenv.2015.09.005.

Liu Z, Hu B, Wang L, Wu F, Gao W, Wang Y. 2015b. Seasonal and diurnal variation in particulate matter (PM_{10} and $PM_{2.5}$) at an urban site of Beijing: analyses from a 9-year study. Environ Sci Pollut Res 22: 627–642.

Lu X, Lin C, Li W, Chen Y, Huang Y, Fung JCH, et al. 2019. Analysis of the adverse health effects of $PM_{2.5}$ from 2001 to 2017 in China and the role of urbanization in aggravating the health burden. Sci Total Environ 652:683–695; doi:10.1016/j.scitotenv.2018.10.140.

Luo J, Du P, Samat A, Xia J, Che M, Xue Z. 2017. Spatiotemporal pattern of $PM_{2.5}$ concentrations in mainland china and analysis of its influencing factors using geographically weighted regression. Sci Rep 7:40607; doi:10.1038/srep40607.

Lyapustin A, Wang YJ, Korkin S, Huang D. 2018. MODIS Collection 6 MAIAC algorithm. Atmospheric Meas Tech 11:5741–5765; doi:10.5194/amt-11-5741-2018.

Ma L, Liu Y, Zhang X, Ye Y, Yin G, Johnson BA. 2019. Deep learning in remote sensing applications: A meta-analysis and review. ISPRS J Photogramm Remote Sens 152:166–177; doi:10.1016/j.isprsjprs.2019.04.015.

Ma Z, Hu X, Huang L, Bi J, Liu Y. 2014. Estimating ground-level $PM_{2.5}$ in China using satellite remote sensing. Environ Sci Technol 48:7436–7444; doi:10.1021/es5009399.

Ma Z, Hu X, Sayer AM, Levy R, Zhang Q, Xue Y, et al. 2016a. Satellite-based spatiotemporal trends in $PM_{2.5}$ concentrations in China, 2004-2013. Environ Health Perspect 124:184–192; doi:10.1289/ehp.1409481.

Ma Z, Liu Y, Zhao Q, Liu M, Zhou Y, Bi J. 2016b. Satellite-derived high resolution $PM_{2.5}$ concentrations in Yangtze River Delta Region of China using improved linear mixed effects model. Atmos Environ 133:156–164; doi:10.1016/j.atmosenv.2016.03.040.

Maji KJ, Dikshit AK, Arora M, Deshpande A. 2018a. Estimating premature mortality attributable to $PM_{2.5}$ exposure and benefit of air pollution control policies in China for 2020. Sci Total Environ 612:683–693; doi:10.1016/j.scitotenv.2017.08.254.

Maji KJ, Ye W-F, Arora M, Shiva Nagendra SM. 2018b. $PM_{2.5}$-related health and economic loss assessment for 338 Chinese cities. Environ Int 121:392–403; doi:10.1016/j.envint.2018.09.024.

Martin RV. 2008. Satellite remote sensing of surface air quality. Atmos Environ 42:7823–7843; doi:10.1016/j.atmosenv.2008.07.018.

Matus K, Nam K-M, Selin NE, Lamsal LN, Reilly JM, Paltsev S. 2012. Health damages from air pollution in China. Glob Environ Change 22:55–66; doi:10.1016/j.gloenvcha.2011.08.006.

Meng X, Wu Y, Pan Z, Wang H, Yin G, Zhao H. 2019. Seasonal characteristics and particle-size distributions of particulate air pollutants in Urumqi. Int J Environ Res Public Health 16:396; doi:10.3390/ijerph16030396.

Miao W, Huang X, Song Y. 2017. An economic assessment of the health effects and crop yield losses caused by air pollution in mainland China. J Environ Sci 56:102–113; doi:10.1016/j.jes.2016.08.024.

Mills NL, Donaldson K, Hadoke PW, Boon NA, MacNee W, Cassee FR, et al. 2009. Adverse cardiovascular effects of air pollution. Nat Clin Pract Cardiovasc Med 6:36–44; doi:10.1038/ncpcardio1399.

Muller NZ, Matthews PH, Wiltshire-Gordon V. 2018. The distribution of income is worse than you think: Including pollution impacts into measures of income inequality. J. Balaguer, ed PLOS ONE 13:e0192461; doi:10.1371/journal.pone.0192461.

Müller T, Schladitz A, Kandler K, Wiedensohler A. 2011. Spectral particle absorption coefficients, single scattering albedos and imaginary parts of refractive indices from ground based in situ measurements at Cape Verde Island during SAMUM-2. Tellus B Chem Phys Meteorol 63:573–588; doi:10.1111/j.1600-0889.2011.00572.x.

Naghavi M, Abajobir AA, Abbafati C, Abbas KM, Abd-Allah F, Abera SF, et al. 2017. Global, regional, and national age-sex specific mortality for 264 causes of death, 1980–2016: a systematic analysis for the Global Burden of Disease Study 2016. The Lancet 390:1151–1210; doi:10.1016/S0140-6736(17)32152-9.

Nakajima T, Tonna G, Rao R, Boi P, Kaufman Y, Holben B. 1996. Use of sky brightness measurements from ground for remote sensing of particulate polydispersions. Appl Opt 35:2672–2686; doi:10.1364/AO.35.002672.

Niu Z, Chen J, Xu L, Yin L, Zhang F. 2013. Application of the environmental internet of things on monitoring $PM_{2.5}$ at a coastal site in the urbanizing region of southeast China. Int J Sustain Dev World Ecol 20: 231–237.

O'Neill MS, Jerrett M, Kawachi I, Levy JI, Cohen AJ, Gouveia N, et al. 2003. Health, wealth, and air pollution: advancing theory and methods. Env Health Perspect 111:1861–70; doi:10.1289/ehp.6334.

Ostro B, Hu J, Goldberg D, Reynolds P, Hertz A, Bernstein L, et al. 2015. Associations of mortality with long-term exposures to fine and ultrafine particles, species and sources: results from the California Teachers Study Cohort. Environ Health Perspect 123:549–556; doi:10.1289/ehp.1408565.

Ozkaynak H, Schatz AD, Thurston GD, Isaacs RG, Husar RB. 1985. Relationships between aerosol extinction coefficients derived from airport visual range observations and alternative measures of airborne particle mass. J Air Pollut Control Assoc 35:1176–1185; doi:10.1080/00022470.1985.10466020.

Pacitto A, Stabile L, Moreno T, Kumar P, Wierzbicka A, Morawska L, et al. 2018. The influence of lifestyle on airborne particle surface area doses received by different Western populations. Environ Pollut 232:113–122; doi:10.1016/j.envpol.2017.09.023.

Pekkanen J, Kulmala M. 2004. Exposure assessment of ultrafine particles in epidemiologic time-series studies. Scand J Work Environ Health 30: 9–18.

Pekkanen J, Pearce N. 2001. Environmental epidemiology: challenges and opportunities. Environ Health Perspect 109:1–5; doi:10.1289/ehp.011091.

Peng J, Chen S, Lü H, Liu Y, Wu J. 2016. Spatiotemporal patterns of remotely sensed $PM_{2.5}$ concentration in China from 1999 to 2011. Remote Sens Environ 174:109–121; doi:10.1016/j.rse.2015.12.008.

Pincus R. 2004. A first course on atmospheric radiation. Eos Trans Am Geophys Union 85:341–341; doi:10.1029/2004EO360007.

Pinto JP, Lefohn AS, Shadwick DS. 2004. Spatial variability of $PM_{2.5}$ in urban areas in the United States. J Air Waste Manag Assoc 54:440–449; doi:10.1080/10473289.2004.10470919.

Pleasants RA, Riley IL, Mannino DM. 2016. Defining and targeting health disparities in chronic obstructive pulmonary disease. Int J Chron Obstruct Pulmon Dis 11:2475–2496; doi:10.2147/COPD.S79077.

Polak M, Genowska A, Szafraniec K, Fryc J, Jamiołkowski J, Pająk A. 2019. Area-based socio-economic inequalities in mortality from lung cancer and respiratory diseases. Int J Environ Res Public Health 16:1791; doi:10.3390/ijerph16101791.

Pope C. Arden, Cohen Aaron J., Burnett Richard T. 2018. Cardiovascular disease and fine particulate matter. Circ Res 122:1645–1647; doi:10.1161/CIRCRESAHA.118.312956.

Pope CA, Ezzati M, Cannon JB, Allen RT, Jerrett M, Burnett RT. 2018. Mortality risk and $PM_{2.5}$ air pollution in the USA: an analysis of a national prospective cohort. Air Qual Atmosphere Health 11:245–252; doi:10.1007/s11869-017-0535-3.

Prats N, Cachorro VE, Berjón A, Toledano C, Frutos AMD. 2011. Column-integrated aerosol microphysical properties from AERONET Sun photometer over southwestern Spain. Atmospheric Chem Phys 11:12535–12547; doi:https://doi.org/10.5194/acp-11-12535-2011.

Qi M, Zhu X, Du W, Chen Y, Chen Y, Huang T, et al. 2017. Exposure and health impact evaluation based on simultaneous measurement of indoor and ambient $PM_{2.5}$ in Haidian, Beijing. Environ Pollut 220:704–712; doi:10.1016/j.envpol.2016.10.035.

Qi YL, Ge JM, Huang JP. 2013. Spatial and temporal distribution of MODIS and MISR aerosol optical depth over northern China and comparison with AERONET. Chin Sci Bull 58:2497–2506; doi:10.1007/s11434-013-5678-5.

Qian J, Liu C. 2018. Distributions and changes of aerosol optical depth on both sides of HU Huanyong Line and the response to land use and land cover. Huanjing Kexue XuebaoActa Sci Circumstantiae 38:752–760; doi:10.13671/j.hjkxxb.2017.0414.

Qian W, Tang X, Quan L. 2004. Regional characteristics of dust storms in China. Atmos Environ 38:4895–4907; doi:10.1016/j.atmosenv.2004.05.038.

Raabe OG. 1976. Aerosol aerodynamic size conventions for inertia! sampler calibration. J Air Pollut Control Assoc 26:856–860; doi:10.1080/00022470.1976.10470329.

Reichstein M, Camps-Valls G, Stevens B, Jung M, Denzler J, Carvalhais N, et al. 2019. Deep learning and process understanding for data-driven Earth system science. Nature 566:195–204; doi:10.1038/s41586-019-0912-1.

Reid JS, Jonsson HH, Maring HB, Smirnov A, Savoie DL, Cliff SS, et al. 2003. Comparison of size and morphological measurements of coarse mode dust particles from Africa. J Geophys Res Atmospheres 108; doi:10.1029/2002JD002485.

Remer LA, Mattoo S, Levy RC, Munchak LA. 2013. MODIS 3 km aerosol product: algorithm and global perspective. Atmospheric Meas Tech 6:1829–1844; doi:https://doi.org/10.5194/amt-6-1829-2013.

Roberts DR, Bahn V, Ciuti S, Boyce MS, Elith J, Guillera-Arroita G, et al. 2017. Cross-validation strategies for data with temporal, spatial, hierarchical, or phylogenetic structure. Ecography 40:913–929; doi:10.1111/ecog.02881.

Rohde RA, Muller RA. 2015. Air pollution in China: Mapping of concentrations and sources. PLOS ONE 10:e0135749; doi:10.1371/journal.pone.0135749.

Rosofsky A, Levy JI, Zanobetti A, Janulewicz P, Fabian MP. 2018. Temporal trends in air pollution exposure inequality in Massachusetts. Environ Res 161:76–86; doi:10.1016/j.envres.2017.10.028.

Saari RK, Mei Y, Monier E, Garcia-Menendez F. 2019. Effect of health-related uncertainty and natural variability on health impacts and co-benefits of climate policy. Environ Sci Technol 53:1098–1108; doi:10.1021/acs.est.8b05094.

Saari RK, Thompson TM, Selin NE. 2017. Human health and economic impacts of ozone reductions by income group. Environ Sci Technol 51:1953–1961; doi:10.1021/acs.est.6b04708.

Sacks JD, Stanek LW, Luben TJ, Johns DO, Buckley BJ, Brown JS, et al. 2011. Particulate matter-induced health effects: who is susceptible? Environ Health Perspect 119:446–454; doi:10.1289/ehp.1002255.

Saha PK, Li HZ, Apte JS, Robinson AL, Presto AA. 2019. Urban ultrafine particle exposure assessment with land-use regression: influence of sampling strategy. Environ Sci Technol 53:7326–7336; doi:10.1021/acs.est.9b02086.

Samoli E, Andersen ZJ, Katsouyanni K, Hennig F, Kuhlbusch TAJ, Bellander T, et al. 2016. Exposure to ultrafine particles and respiratory hospitalizations in five European cities. Eur Respir J 48:674–682; doi:10.1183/13993003.02108-2015.

Schoen C, Radley DC, Riley P, Lippa JA, Berenson J, Dermody C, et al. 2013. Health care in the two Americas: Findings from the Scorecard on State Health System Performance for low-income populations. Available: http://www.commonwealthfund.org/publications/fund-reports/2013/sep/low-income-scorecard [accessed 20 April 2015].

Schuster GL, Dubovik O, Holben BN. 2006. Angstrom exponent and bimodal aerosol size distributions. J Geophys Res Atmospheres 111; doi:10.1029/2005JD006328.

Shao J, Mao J. 2016. Dust particle size distributions during spring in Yinchuan, China. Adv Meteorol 2016:8; doi:10.1155/2016/6940502.

Shen G, Xue M, Yuan S, Zhang J, Zhao Q, Li B, et al. 2014. Chemical compositions and reconstructed light extinction coefficients of particulate matter in a mega-city in the western Yangtze River Delta, China. Atmos Environ 83: 14–20.

Shen H, Li T, Yuan Q, Zhang L. 2018. Estimating regional ground-level $pm_{2.5}$ directly from satellite top-of-atmosphere reflectance using deep belief networks. J Geophys Res Atmospheres 123:13,875-13,886; doi:10.1029/2018JD028759.

Sherbinin A de, Levy MA, Zell E, Weber S, Jaiteh M. 2014. Using satellite data to develop environmental indicators. Environ Res Lett 9:084013; doi:10.1088/1748-9326/9/8/084013.

Snauffer AM, Hsieh WW, Cannon AJ, Schnorbus MA. 2018. Improving gridded snow water equivalent products in British Columbia, Canada: multi-source data fusion by neural network models. The Cryosphere 12:891–905; doi:https://doi.org/10.5194/tc-12-891-2018.

Song C, Wu L, Xie Y, He J, Chen X, Wang T, et al. 2017. Air pollution in China: Status and spatiotemporal variations. Environ Pollut 227:334–347; doi:10.1016/j.envpol.2017.04.075.

Song WZ, Jia HF, Huang JF, Zhang YY. 2014. A satellite-based geographically weighted regression model for regional $PM_{2.5}$ estimation over the Pearl River Delta region in China. Remote Sens Environ 154:1–7; doi:10.1016/j.rse.2014.08.008.

Song YZ, Yang HL, Peng JH, Song YR, Sun Q, Li Y. 2015. Estimating $PM_{2.5}$ concentrations in Xi'an city using a generalized additive model with multi-source monitoring data. PLoS One 10:e0142149; doi:10.1371/journal.pone.0142149.

Steele HM, Eldering A, Lumpe JD. 2006. Simulations of the accuracy in retrieving stratospheric aerosol effective radius, composition, and loading from infrared spectral transmission measurements. Appl Opt 45:2014–2027; doi:10.1364/AO.45.002014.

Steinle S, Reis S, Sabel CE, Semple S, Twigg MM, Braban CF, et al. 2015. Personal exposure monitoring of $PM_{2.5}$ in indoor and outdoor microenvironments. Sci Total Environ 508:383–394; doi:10.1016/j.scitotenv.2014.12.003.

Steyn DG, Galmarini S. 2008. Evaluating the predictive and explanatory value of atmospheric numerical models: Between relativism and objectivism. Open Atmospheric Sci J 2.

Sun Y, Zeng Q, Geng B, Lin X, Sude B, Chen L. 2019. Deep learning architecture for estimating hourly ground-level $PM_{2.5}$ using satellite remote sensing. IEEE Geosci Remote Sens Lett 16:1343–1347; doi:10.1109/LGRS.2019.2900270.

Tang Y, Chai T, Pan L, Lee P, Tong D, Kim HC, et al. 2015. Using optimal interpolation to assimilate surface measurements and satellite AOD for ozone and $PM_{2.5}$: A case study for July 2011. J Air Waste Manag Assoc 65:1206–16; doi:10.1080/10962247.2015.1062439.

Tao J, Zhang M, Chen L, Wang Z, Su L, Ge C, et al. 2012. A method to estimate concentrations of surface-level particulate matter using satellite-based aerosol optical thickness. Sci China Earth Sci 56:1422–1433; doi:10.1007/s11430-012-4503-3.

Taylor M, Kazadzis S, Tsekeri A, Gkikas A, Amiridis V. 2014. Satellite retrieval of aerosol microphysical and optical parameters using neural networks: a new methodology applied to the Sahara desert dust peak. Atmospheric Meas Tech 7:3151–3175; doi:https://doi.org/10.5194/amt-7-3151-2014.

Tian P, Cao X, Zhang L, Wang H, Shi J, Huang Z, et al. 2015. Observation and simulation study of atmospheric aerosol nonsphericity over the Loess Plateau in northwest China. Atmos Environ 117:212–219; doi:10.1016/j.atmosenv.2015.07.020.

Tsai T-C, Jeng Y-J, Chu DA, Chen J-P, Chang S-C. 2011. Analysis of the relationship between MODIS aerosol optical depth and particulate matter from 2006 to 2008. Atmos Environ 45:4777–4788; doi:10.1016/j.atmosenv.2009.10.006.

University of British Columbia. 2016. Poor air quality kills 5.5 million worldwide annually. ScienceDaily, Available at www.sciencedaily.com/releases/2016/02/160212140912.htm [accessed 8 January 2020].

van Donkelaar A, Martin RV, Brauer M, Boys BL. 2015. Use of satellite observations for long-term exposure assessment of global concentrations of fine particulate matter. Env Health Perspect 123:135–43; doi:10.1289/ehp.1408646.

van Donkelaar A, Martin RV, Brauer M, Hsu NC, Kahn RA, Levy RC, et al. 2016. Global estimates of fine particulate matter using a combined geophysical-statistical method with information from satellites, models, and monitors. Environ Sci Technol 50:3762–3772; doi:10.1021/acs.est.5b05833.

van Donkelaar A, Martin RV, Brauer M, Kahn R, Levy R, Verduzco C, et al. 2010. Global estimates of ambient fine particulate matter concentrations from satellite-based aerosol optical depth: development and application. Environ Health Perspect 118:847–855; doi:10.1289/ehp.0901623.

van Donkelaar A, Martin RV, Li C, Burnett RT. 2019. Regional estimates of chemical composition of fine particulate matter using a combined geoscience-statistical method with information from satellites, models, and monitors. Environ Sci Technol 53:2595–2611; doi:10.1021/acs.est.8b06392.

van Donkelaar A, Martin RV, Park RJ. 2006. Estimating ground-level $PM_{2.5}$ using aerosol optical depth determined from satellite remote sensing. J Geophys Res 111; doi:10.1029/2005jd006996.

van Ourti T, van Doorslaer E, Koolman X. 2009. The effect of income growth and inequality on health inequality: Theory and empirical evidence from the European Panel. J Health Econ 28:525–539; doi:10.1016/j.jhealeco.2008.12.005.

Vandal T, Kodra E, Ganguly S, Michaelis A, Nemani R, Ganguly AR. 2017. DeepSD: Generating high resolution climate change projections through single image super-resolution. ArXiv170303126 Cs.

Vicent J, Sabater N, Verrelst J, Alonso L, Moreno J. 2017. Assessment of approximations in aerosol optical properties and vertical distribution into FLEX atmospherically-corrected surface reflectance and retrieved sun-induced fluorescence. Remote Sens 9:675.

Viscusi WK, Aldy JE. 2003. The value of a statistical life: A critical review of market estimates throughout the world. J Risk Uncertain 27:5–76; doi:10.1023/A:1025598106257.

Waheed A, Zhu Y, Tan M, Bao L, Zhang G, Li Y, et al. 2013. Characterization and source identification of fine particulate matter in the atmosphere of downtown Shanghai using -SXRF and ICP-MS. Nucl Sci Tech 21: 197–197.

Wang H, Zhang L, Cao X, Zhang Z, Liang J. 2013. A-Train satellite measurements of dust aerosol distributions over northern China. J Quant Spectrosc Radiat Transf 122:170–179; doi:10.1016/j.jqsrt.2012.08.011.

Wang HL, Qiao LP, Lou SR, Zhou M, Ding AJ, Huang HY, et al. 2016. Chemical composition of $PM_{2.5}$ and meteorological impact among three years in urban Shanghai, China. J Clean Prod 112:1302–1311; doi:10.1016/j.jclepro.2015.04.099.

Wang Q, Wang J, He MZ, Kinney PL, Li T. 2018a. A county-level estimate of $PM_{2.5}$ related chronic mortality risk in China based on multi-model exposure data. Environ Int 110:105–112; doi:10.1016/j.envint.2017.10.015.

Wang S, Liu X, Yang X, Zou B, Wang J. 2018b. Spatial variations of $PM_{2.5}$ in Chinese cities for the joint impacts of human activities and natural conditions: A global and local regression perspective. J Clean Prod 203:143–152; doi:10.1016/j.jclepro.2018.08.249.

Wang X, Dong Z, Zhang J, Liu L. 2004. Modern dust storms in China: an overview. J Arid Environ 58:559–574; doi:10.1016/j.jaridenv.2003.11.009.

Wang X, Zhang C, Wang H, Qian G, Luo W, Lu J, et al. 2011. The significance of Gobi desert surfaces for dust emissions in China: an experimental study. Environ Earth Sci 64:1039–1050; doi:10.1007/s12665-011-0922-2.

West JJ, Cohen A, Dentener F, Brunekreef B, Zhu T, Armstrong B, et al. 2016. "What we breathe impacts our health: improving understanding of the link between air pollution and health." Environ Sci Technol 50:4895–4904; doi:10.1021/acs.est.5b03827.

WHO. 2016. Ambient air pollution: A global assessment of exposure and burden of disease. [accessed 8 January 2020].

WHO. 2018. Ambient (outdoor) air pollution. Available at https://www.who.int/news-room/fact-sheets/detail/ambient-(outdoor)-air-quality-and-health [accessed 8 January 2020].

Wichmann HE, Spix C, Tuch T, Wölke G, Peters A, Heinrich J, et al. 2000. Daily mortality and fine and ultrafine particles in Erfurt, Germany part I: role of particle number and particle mass. Res Rep Health Eff Inst 5–86; discussion 87-94.

Wilper AP, Woolhandler S, Lasser KE, McCormick D, Bor DH, Himmelstein DU. 2009. Health Insurance and Mortality in US Adults. Am J Public Health 99:2289–2295; doi:10.2105/AJPH.2008.157685.

Wu Y, Guo J, Zhang X, Tian X, Zhang J, Wang Y, et al. 2012. Synergy of satellite and ground based observations in estimation of particulate matter in eastern China. Sci Total Environ 433:20–30; doi:10.1016/j.scitotenv.2012.06.033.

Xiao Q, Chang HH, Geng G, Liu Y. 2018. An ensemble machine-learning model to predict historical $PM_{2.5}$ concentrations in China from satellite data. Environ Sci Technol 52:13260–13269; doi:10.1021/acs.est.8b02917.

Xiao Q, Wang Y, Chang HH, Meng X, Geng G, Lyapustin A, et al. 2017. Full-coverage high-resolution daily $PM_{2.5}$ estimation using MAIAC AOD in the Yangtze River Delta of China. Remote Sens Environ 199:437–446; doi:10.1016/j.rse.2017.07.023.

Xie P, Liu X, Liu Z, Li T, Zhong L, Xiang Y. 2010. Impact of exposure to air pollutants on human health effects in Pearl River Delta. China Environ Sci 30: 997–1003.

Xie R, Sabel CE, Lu X, Zhu W, Kan H, Nielsen CP, et al. 2016a. Long-term trend and spatial pattern of $PM_{2.5}$ induced premature mortality in China. Environ Int 97:180–186; doi:10.1016/j.envint.2016.09.003.

Xie Y, Dai H, Dong H, Hanaoka T, Masui T. 2016b. Economic Impacts from $PM_{2.5}$ Pollution-Related Health Effects in China: A Provincial-Level Analysis. Environ Sci Technol 50:4836–4843; doi:10.1021/acs.est.5b05576.

Xie Y, Dai H, Zhang Y, Wu Y, Hanaoka T, Masui T. 2019. Comparison of health and economic impacts of $PM_{2.5}$ and ozone pollution in China. Environ Int 130:104881; doi:10.1016/j.envint.2019.05.075.

Xie Y, Wang Y, Zhang K, Dong W, Lv B, Bai Y. 2015. Daily estimation of ground-level $PM_{2.5}$ concentrations over Beijing using 3 km resolution MODIS AOD. Environ Sci Technol 49:12280–12288; doi:10.1021/acs.est.5b01413.

Xin JY, Zhang Q, Wang LL, Gong CS, Wang YS, Liu ZR, et al. 2014. The empirical relationship between the $PM_{2.5}$ concentration and aerosol optical depth over the background of North China from 2009 to 2011. Atmospheric Res 138:179–188; doi:10.1016/j.atmosres.2013.11.001.

Xu L, Chen X, Chen J, Zhang F, He C, Zhao J, et al. 2012. Seasonal variations and chemical compositions of $PM_{2.5}$ aerosol in the urban area of Fuzhou, China. Atmospheric Res 104: 264–272.

Xue T, Zheng Y, Tong D, Zheng B, Li X, Zhu T, et al. 2019a. Spatiotemporal continuous estimates of $PM_{2.5}$ concentrations in China, 2000–2016: A machine learning method with inputs from satellites, chemical transport model, and ground observations. Environ Int 123:345–357; doi:10.1016/j.envint.2018.11.075.

Xue T, Zhu T, Zheng Y, Liu J, Li X, Zhang Q. 2019b. Change in the number of $PM_{2.5}$-attributed deaths in China from 2000 to 2010: Comparison between estimations from census-based

epidemiology and pre-established exposure-response functions. Environ Int 129:430–437; doi:10.1016/j.envint.2019.05.067.

Yan X, Li ZQ, Luo NN, Shi WZ, Zhao WJ, Yang XC, et al. 2019. An improved algorithm for retrieving the fine-mode fraction of aerosol optical thickness. Part 2: Application and validation in Asia. Remote Sens Environ 222:90–103; doi:10.1016/j.rse.2018.12.012.

Yan X, Shi W, Li Z, Li Z, Luo N, Zhao W, et al. 2017. Satellite-based $PM_{2.5}$ estimation using fine-mode aerosol optical thickness over China. Atmos Environ 170:290–302; doi:10.1016/j.atmosenv.2017.09.023.

Yang B-Y, Qian Z (Min), Li S, Fan S, Chen G, Syberg KM, et al. 2018. Long-term exposure to ambient air pollution (including PM_1) and metabolic syndrome: The 33 Communities Chinese Health Study (33CCHS). Environ Res 164:204–211; doi:10.1016/j.envres.2018.02.029.

Yang C, Peng X, Huang W, Chen R, Xu Z, Chen B, et al. 2012. A time-stratified case-crossover study of fine particulate matter air pollution and mortality in Guangzhou, China. Int Arch Occup Environ Health 85: 579–585.

Yang G, Wang Y, Zeng Y, Gao GF, Liang X, Zhou M, et al. 2013. Rapid health transition in China, 1990–2010: Findings from the Global Burden of Disease Study 2010. The Lancet 381:1987–2015; doi:10.1016/S0140-6736(13)61097-1.

Yang Q, Yuan Q, Yue L, Li T, Shen H, Zhang L. 2019. The relationships between $PM_{2.5}$ and aerosol optical depth (AOD) in mainland China: About and behind the spatio-temporal variations. Environ Pollut 248:526–535; doi:10.1016/j.envpol.2019.02.071.

Yang T, Liu W. 2018. Does air pollution affect public health and health inequality? Empirical evidence from China. J Clean Prod 203:43–52; doi:10.1016/j.jclepro.2018.08.242.

Yang X, Zheng Y, Geng G, Liu H, Man H, Lv Z, et al. 2017. Development of $PM_{2.5}$ and NO_2 models in a LUR framework incorporating satellite remote sensing and air quality model data in Pearl River Delta region, China. Environ Pollut 226:143–153; doi:10.1016/j.envpol.2017.03.079.

Yao F, Wu J, Li W, Peng J. 2019. A spatially structured adaptive two-stage model for retrieving ground-level $PM_{2.5}$ concentrations from VIIRS AOD in China. ISPRS J Photogramm Remote Sens 151:263–276; doi:10.1016/j.isprsjprs.2019.03.011.

Yin L, Niu Z, Chen X, Chen J, Xu L, Zhang F. 2012. Chemical compositions of $PM_{2.5}$ aerosol during haze periods in the mountainous city of Yong'an, China. J Environ Sci 24:1225–1233; doi:10.1016/S1001-0742(11)60940-6.

Yin P, Brauer M, Cohen A, Burnett R, Liu J, Liu Y, et al. 2017. Long-term fine particulate matter exposure and nonaccidental and cause-specific mortality in a large national cohort of Chinese Men. Environ Health Perspect 125:117002; doi:10.1289/EHP1673.

You W, Zang Z, Pan X, Zhang L, Chen D. 2015. Estimating $PM_{2.5}$ in Xi'an, China using aerosol optical depth: A comparison between the MODIS and MISR retrieval models. Sci Total Environ 505:1156–1165; doi:10.1016/j.scitotenv.2014.11.024.

You W, Zang Z, Zhang L, Li Y, Pan X, Wang W. 2016. National-scale estimates of ground-level $PM_{2.5}$ concentration in China using geographically weighted regression based on 3 km resolution MODIS AOD. Remote Sens 8:184; doi:10.3390/rs8030184.

Yu J, Che H, Chen Q, Xia X, Zhao H, Wang HY, et al. 2015. Investigation of aerosol optical depth (AOD) and Ångström exponent over the desert region of northwestern China based on measurements from the China Aerosol Remote Sensing Network (CARSNET). Aerosol Air Qual Res 15:2024–2036; doi:10.4209/aaqr.2014.12.0326.

Yu Q, Lu Y, Xiao S, Shen J, Li X, Ma W, et al. 2012. Commuters' exposure to PM_1 by common travel modes in Shanghai. Atmos Environ 59:39–46; doi:10.1016/j.atmosenv.2012.06.001.

Yu W, Liu Y, Ma Z, Bi J. 2017. Improving satellite-based $PM_{2.5}$ estimates in China using Gaussian processes modeling in a Bayesian hierarchical setting. Sci Rep 7:7048; doi:10.1038/s41598-017-07478-0.

Yu Y, Schleicher N, Norra S, Fricker M, Dietze V, Kaminski U, et al. 2011. Dynamics and origin of $PM_{2.5}$ during a three-year sampling period in Beijing, China. J Environ Monit 13: 334–346.

Yuan C, Lee C, Liu S, Chang J, Yuan C, Yang H. 2006. Correlation of atmospheric visibility with chemical composition of Kaohsiung aerosols. Atmospheric Res 82:663–679; doi:10.1016/j.atmosres.2006.02.027.

Yuan Q, Shen H, Li T, Li Z, Li S, Jiang Y, et al. 2020. Deep learning in environmental remote sensing: Achievements and challenges. Remote Sens Environ 241:111716; doi:10.1016/j.rse.2020.111716.

Yusuf S, Hawken S, Ôunpuu S, Dans T, Avezum A, Lanas F, et al. 2004. Effect of potentially modifiable risk factors associated with myocardial infarction in 52 countries (the INTERHEART study): case-control study. The Lancet 364:937–952.

Zang L, Mao F, Guo J, Wang W, Pan Z, Shen H, et al. 2019. Estimation of spatiotemporal $PM_{1.0}$ distributions in China by combining $PM_{2.5}$ observations with satellite aerosol optical depth. Sci Total Environ 658:1256–1264; doi:10.1016/j.scitotenv.2018.12.297.

Zhang F, Cheng H, Wang Z, Lv X, Zhu Z, Zhang G, et al. 2014. Fine particles ($PM_{2.5}$) at a CAWNET background site in Central China: Chemical compositions, seasonal variations and regional pollution events. Atmos Environ 86: 193–202.

Zhang L, Liu L, Zhao Y, Gong S, Zhang X, Henze DK, et al. 2015a. Source attribution of particulate matter pollution over North China with the adjoint method. Environ Res Lett 10:084011; doi:10.1088/1748-9326/10/8/084011.

Zhang L, Sun JY, Shen XJ, Zhang YM, Che H, Ma QL, et al. 2015b. Observations of relative humidity effects on aerosol light scattering in the Yangtze River Delta of China. Atmospheric Chem Phys 15:8439–8454; doi:https://doi.org/10.5194/acp-15-8439-2015.

Zhang R, Jing J, Tao J, Hsu S-C, Wang G, Cao J, et al. 2013. Chemical characterization and source apportionment of $PM_{2.5}$ in Beijing: seasonal perspective. Atmospheric Chem Phys 13:7053–7074; doi:https://doi.org/10.5194/acp-13-7053-2013.

Zhang X, Ou X, Yang X, Qi T, Nam K-M, Zhang D, et al. 2017. Socioeconomic burden of air pollution in China: Province-level analysis based on energy economic model. Energy Econ 68:478–489.

Zhang Y, Li Z. 2015. Remote sensing of atmospheric fine particulate matter ($PM_{2.5}$) mass concentration near the ground from satellite observation. Remote Sens Environ 160:252–262; doi:10.1016/j.rse.2015.02.005.

Zhao B, Zheng H, Wang S, Smith KR, Lu X, Aunan K, et al. 2018. Change in household fuels dominates the decrease in $PM_{2.5}$ exposure and premature mortality in China in 2005–2015. Proc Natl Acad Sci 115:12401–12406; doi:10.1073/pnas.1812955115.

Zhao H, Geng G, Zhang Q, Davis SJ, Li X, Liu Y, et al. 2019. Inequality of household consumption and air pollution-related deaths in China. Nat Commun 10:1–9; doi:10.1038/s41467-019-12254-x.

Zhao H, Li X, Zhang Q, Jiang X, Lin J, Peters GG, et al. 2017. Effects of atmospheric transport and trade on air pollution mortality in China. Atmos. Chem. Phys. 17:10367–10381.

Zhao M, Qiao T, Huang Z, Zhu M, Xu W, Xiu G, et al. 2015. Comparison of ionic and carbonaceous compositions of $PM_{2.5}$ in 2009 and 2012 in Shanghai, China. Sci Total Environ 536: 695–703.

Zhao TL. 2003. Modeled size-segregated wet and dry deposition budgets of soil dust aerosol during ACE-Asia 2001: Implications for trans-Pacific transport. J Geophys Res 108:8665.

Zhao X, Zhang X, Xu X, Xu J, Meng W, Pu W. 2009. Seasonal and diurnal variations of ambient $PM_{2.5}$ concentration in urban and rural environments in Beijing. Atmos Environ 43: 2893–2900.

Zhao XR, Shi HQ, Yu H, Yang PL. 2016. Inversion of nighttime $PM_{2.5}$ mass concentration in Beijing based on the VIIRS Day-Night Band. Atmosphere 7.

Zheng GJ, Duan FK, Su H, Ma YL, Cheng Y, Zheng B, et al. 2015a. Exploring the severe winter haze in Beijing: the impact of synoptic weather, regional transport and heterogeneous reactions. Atmospheric Chem Phys 15:2969–2983; doi:10.5194/acp-15-2969-2015.

Zheng S, Pozzer A, Cao CX, Lelieveld J. 2015b. Long-term (2001–2012) concentrations of fine particulate matter ($PM_{2.5}$) and the impact on human health in Beijing, China. Atmospheric Chem Phys 15:5715–5725.

Zheng Y, Xue T, Zhang Q, Geng G, Tong D, Li X, et al. 2017. Air quality improvements and health benefits from China's clean air action since 2013. Environ Res Lett 12:114020;.

Zheng Y, Zhang Q, Liu Y, Geng G, He K. 2016. Estimating ground-level PM $_{2.5}$ concentrations over three megalopolises in China using satellite-derived aerosol optical depth measurements. Atmos Environ 124:232–242; doi:10.1016/j.atmosenv.2015.06.046.

Zhou M, Qiao L, Zhu S, Li L, Lou S, Wang H, et al. 2016a. Chemical characteristics of fine particles and their impact on visibility impairment in Shanghai based on a 1-year period observation. J Environ Sci 48: 151–160.

Zhou M, Wang H, Zhu J. 2016b. Cause-specific mortality for 240 causes in China during 1990–2013: a systematic subnational analysis for the Global Burden of Disease Study 2013. The Lancet 387:251–272; doi:10.1016/S0140-6736(15)00551-6.

Zhou W, Tie X, Zhou G, Liang P. 2015. Possible effects of climate change of wind on aerosol variation during winter in Shanghai, China. Particuology 20:80–88; doi:10.1016/j.partic.2014.08.008.

Zhu G, Hu W, Liu Y, Cao J, Ma Z, Deng Y, et al. 2019. Health burdens of ambient $PM_{2.5}$ pollution across Chinese cities during 2006–2015. J Environ Manage 243:250–256.

Zieger P, Fierz-Schmidhauser R, Poulain L, Müller T, Birmili W, Spindler G, et al. 2014. Influence of water uptake on the aerosol particle light scattering coefficients of the Central European aerosol. Tellus B Chem Phys Meteorol 66:22716; doi:10.3402/tellusb.v66.22716.

Appendix A

Supplementary Information for Exposure Estimation

A1. Calibration and Validation of MODIS AOD

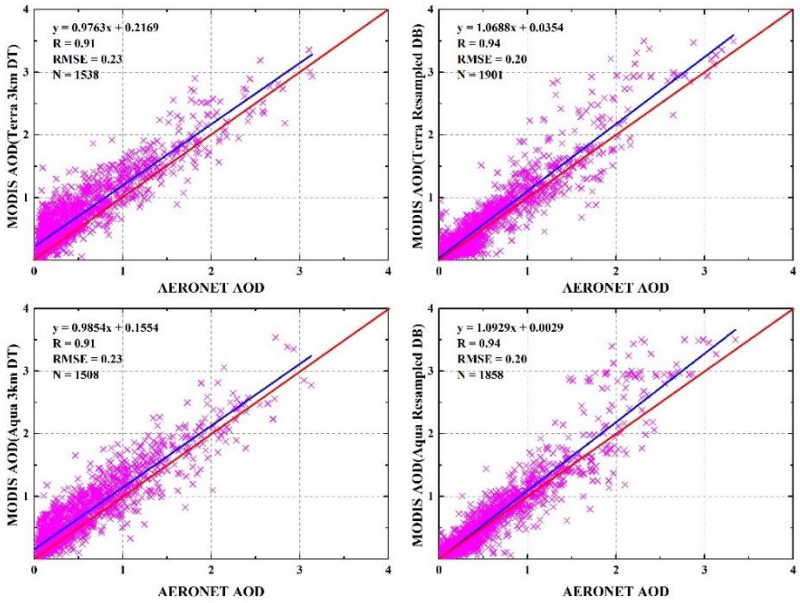

Figure A1 Linear relationship between annual MODIS AOD and AERONET AOD among four datasets from 2013 to 2016 (a) MODIS DT AOD products aboard Terra (b) MODIS DB AOD products aboard Terra (c)MODIS DT AOD products aboard Aqua (d) MODIS DB AOD products aboard Aqua

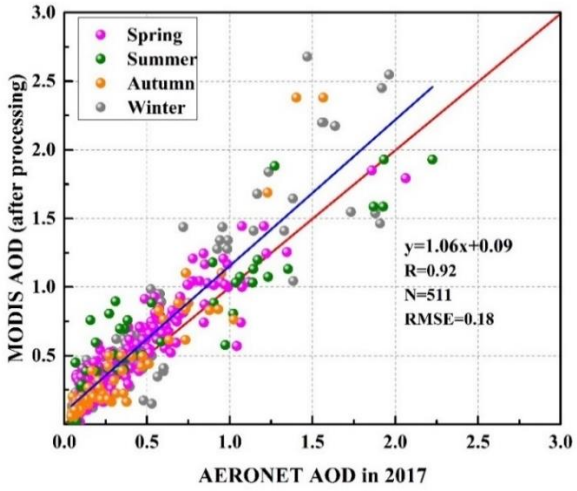

Figure A2 Validation of AOD after calibration and gap-filling

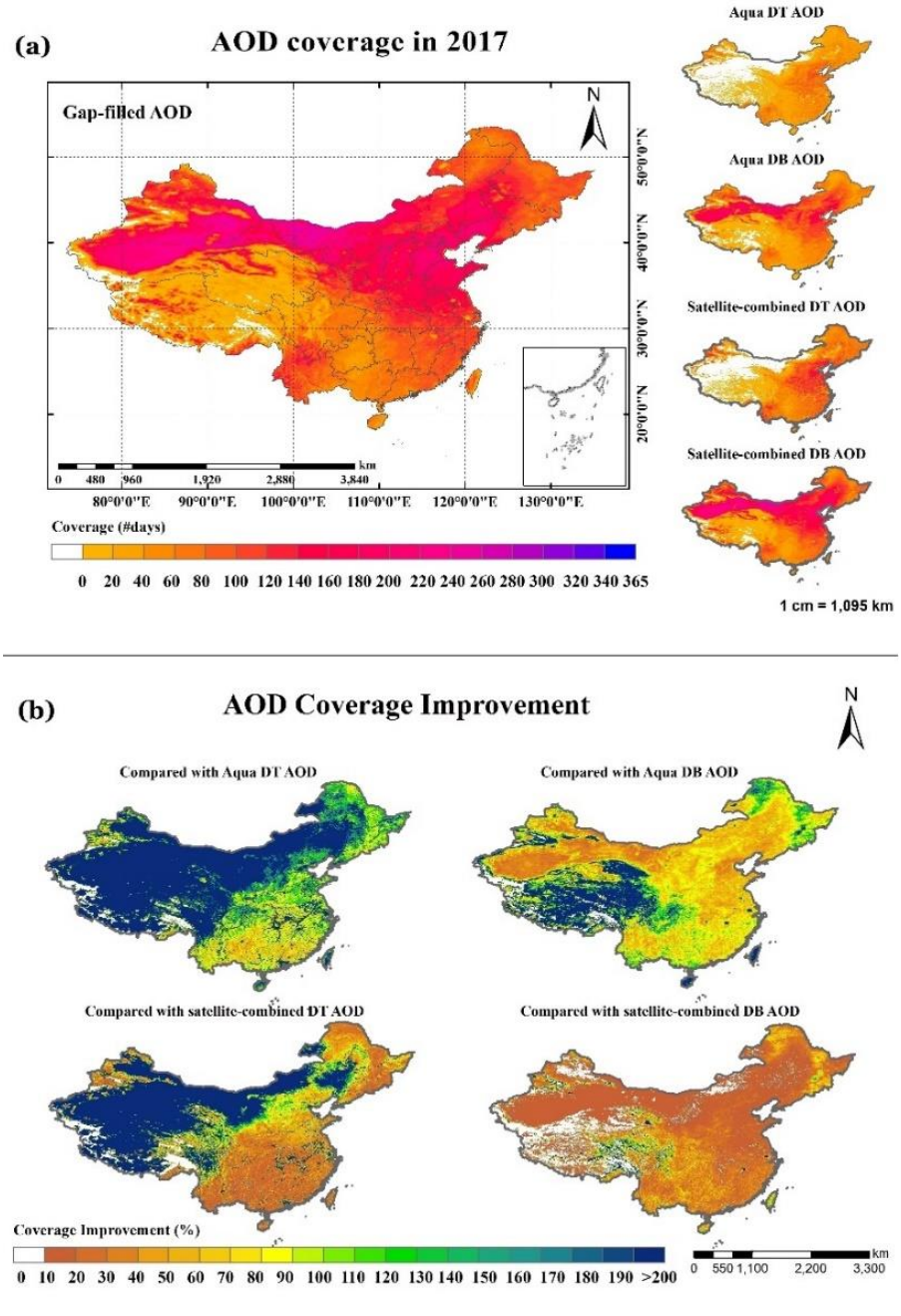

Figure A3 Spatial distribution of annual AOD coverage and improvement

Table A1 Calibration for MODIS AOD products

Season			Spring (DOY 60~149)	Summer (DOY150~241)	Autumn (DOY242~332)	Winter (DOY1~59,333~365)
MODIS 3KM DT	Aqua	Regression equation	y = 0.71x	y = 0.90x - 0.095	y = 0.92x - 0.06	y = 0.96x + 0.01
		R	0.90	0.92	0.93	0.90
		RMSE	0.17	0.26	0.18	0.11
		N	421	448	453	181
	Terra	Regression equation	y = 0.72x + 0.07	y = 0.92x - 0.18	y = 0.95x - 0.12	y = 0.94x - 0.04
		R	0.88	0.92	0.93	0.90
		RMSE	0.19	0.27	0.17	0.10
		N	462	431	445	203
MODIS resampled DB	Aqua	Regression equation	y = 1.00x - 0.01	y = 0.79x + 0.12	y = 0.75x + 0.08	y = 0.74x + 0.05
		R	0.96	0.95	0.96	0.92
		RMSE	0.14	0.24	0.16	0.14
		N	556	297	445	557
	Terra	Regression equation	y = 0.95x - 0.02	y = 0.79x + 0.11	y = 0.84x + 0.03	y = 0.65x + 0.03
		R	0.93	0.94	0.96	0.94
		RMSE	0.17	0.21	0.16	0.14
		N	583	318	433	574

Note: R and RMSE are Pearson correlation coefficient and root mean square error, respectively.

A2. Calculation of hygroscopic growth

No previous studies have measured aerosol hygroscopic properties in China at national scale. Therefore, we adopt three empirical regional models to reflect aerosol hygroscopic growth. Eq. (A1), (A2) and (A3) are fitted by the measured samples located at Beijing (39.93°N, 116.28°E), Lin'an (30.30°N, 119.73°E) and Guangzhou (23.13°N, 113.25°E), representing the aerosol hygroscopic properties in the North China Plain (Chen et al. 2014), Yangtze River Delta (Zhang et al. 2015) and Pearl River Delta(Liu et al. 2008), respectively.

$$f(RH) = \begin{cases} 1.02 * (1 - RH/100)^{-0.21*RH/100} & (RH/100 < 0.6) \\ 1.08 * (1 - RH/100)^{-0.26*RH/100} & (RH/100 \geq 0.6) \end{cases} \quad \text{(A1)}$$

$$f(RH) = 1 + 1.20 * \left(\frac{RH}{100}\right)^{3.90} \quad \text{(A2)}$$

$$f(RH) = 1 + 3.26 * \left(\frac{RH}{100}\right)^{3.85} \quad \text{(A3)}$$

For each pixel, we calculate three $f(RH)_i$ values based on above equations and then conduct the inverse distance weighting algorithm to obtain the final $f(RH)$. Beijing, Lin'an and Guangzhou are set as the reference sites. For one unknown pixel, we

(1) calculate the distances between unknown pixel (x, y) and three reference sites (x_i, y_i), i=1,2,3;

$$d_i = \sqrt{(x - x_i)^2 + (y - y_i)^2} \quad \text{(A4)}$$

(2) calculate the weight w_i, which is the inverse of the distance;

$$w_i = \frac{1}{{d_i}^p} \quad \text{(A5)}$$

(3) calculate the weighted average $f(RH)$.

$$f(RH) = \begin{cases} \sum_{i=1}^{3} w_i * f(RH)_i, & if\ d_i \neq 0\ for\ all\ i \\ f(RH)_i, & \text{if } d_i \neq 0 \text{ for some i} \end{cases} \quad \text{(A6)}$$

We also calculated the maximum difference in these three f(RH) for each RH value and counted the frequency at annual scale to quantify the uncertainty on the hygroscopic growth functions. The maximum $\delta f(RH)$ was estimated to be 0.39 in our conversion algorithm and the error of f(RH) item are about $\pm$23%.

A3. Correlation and Collinearity Analysis in $PM_{2.5}$ Estimation Using the GWR Model

The parameters adopted in the $PM_{2.5}$ estimation model meet the following criteria:

(1) The explanatory parameter is correlated to dependent parameters (Table A2).

(2) No multi-collinearity exists. The variance inflation factor (VIF) was adopted to measure the collinearity of multiple variables in the model (Table A3). A VIF value lower than 10 indicates there is no collinearity among variables and a value higher than 10 indicate high collinearity (Belsley et al. 2005).

(3) The p-value of the variable is less than 0.05.

Table A2 Correlation matrix

Variables	$PM_{2.5}$	AOD	WS	T	VIS	DEM
$PM_{2.5}$	1.000					
AOD	0.518	1.000				
WS	-0.190	-0.054	1.000			
T	-0.249	0.179	-0.011	1.000		
VIS	-0.493	-0.313	0.267	0.126	1.000	
DEM	-0.288	-0.332	0.043	-0.136	0.069	1.000

Table A3 Collinearity analysis of explanatory variables

Variables	AOD/(PBLH*f(RH))	WS	T	VIS	DEM
VIF	1.22	1.37	2.59	1.59	1.30

A4. Influence of Constant Parameters on Radius Estimation

Some estimation error comes from the use of constant parameters since the particle density and size distribution vary across spatial and temporal domains. Hence, we conducted a one-at-a-time parameter sensitivity analysis to explore the influence of constant parameters (geometric standard deviation σ_g and particle density ρ) on radius (Figure A4). The geometric standard deviation was set at 2 in the study, which within the 1.9-2.05 range typically measured for fine-mode aerosols (Clarisse et al. 2010; Steele et al. 2006). The average value of σ_g in the OPAC database for most fine aerosol components is 2.14μm (Hess et al. 1998). The particle mass density was set at 1.5 g/cm^3. The general range of mass density is 1.5-2.1 g/cm^3 in different regions (Gao et al. 2007; Hand and Kreidenweis 2002; Hänel and Thudium 1977; McMurry et al. 2002). The ranges of these two parameters were set with reference to the general values for different types of fine particles, ranging from 1.2 to 2.5 with step size of 0.05. The result indicates that the radius estimates are more sensitive to σ_g since the rate of change of σ_g is higher than that of ρ over the same interval. The assumption of setting σ_g (ρ) at 2 (1.5 g/cm^3) will introduce up to 0.11μm (0.04μm) bias when σ_g=1.2 (ρ=2.5) in the radius retrieval.

According to the Koschmieder equation, the surface aerosol extinction at 550 nm is inversely proportional to surface visibility. If the contrast threshold of human eye was set to 0.02, the constant term in the equation is 3.912. However, various constant values ranging from 1.8 to 3.912 has been reported in different sites (Kessner et al. 2013; Ozkaynak et al. 1985; Yuan et al. 2006). Therefore, we conducted a sensitivity analysis to explore the influence of this constant on extinction. The result shows that the constant 3.912 can result in a maximum error of 0.01 when V=0.2km.

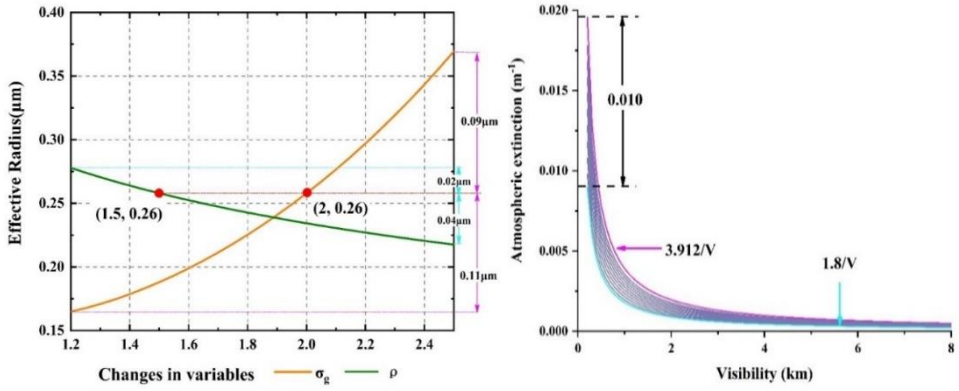

Figure A4 Sensitivity analysis of **σ_g**, **ρ** and constant in Koschmieder's equation

Appendix B

Supplementary Information for Health and Environmental Impacts

Table B1 Annual $PM_{2.5}$ concentrations from 2005 to 2013 reported by previous publications

Year	City	Longitude (°E)	Latitude (°N)	$PM_{2.5}$ (μg/m^3)	Reference
2005	Beijing	116.37	39.97	70.7	(Liu et al. 2015b)
2005	Beijing	116.3	39.9	85.2	(Zhao et al. 2009)
2005	Shanghai	121.43	31.19	56.4	(Kan et al. 2007)
2006	Beijing	116.37	39.97	83.1	(Liu et al. 2015b)
2006	Beijing	116.3	39.9	93.5	(Zhao et al. 2009)
2006	Guangzhou	113.3	23.1	60	(Xie et al. 2010)
2007	Beijing	116.37	39.97	75.7	(Liu et al. 2015b)
2007	Beijing	116.3	39.9	84.5	(Zhao et al. 2009)
2007	Beijing	116.35	39.99	64.2	(Yu et al. 2011)
2007	Fuzhou	119.3	26.08	44.3	(Xu et al. 2012)
2007	Guangzhou	113.26	23.16	70.1	(Yang et al. 2012)
2007	Guangzhou	113.2	23.1	42.4	(Huang et al. 2010)
2007	Hangzhou	120.17	30.25	69.0	(Hong et al. 2013)
2007	Qingdao	120.4	36.1	86.6	(Li et al. 2012)
2007	Taishan	117.1	36.25	70.1	(Deng et al. 2011)
2007	Weifang	119.1	36.7	90.4	(Li et al. 2013)
2007	Shanghai	121.48	31.23	54.8	(Waheed et al. 2013)
2008	Beijing	116.41	40.04	88.7	(Chen et al. 2014b)
2008	Beijing	116.37	39.97	67.3	(Liu et al. 2015b)
2008	Guangzhou	113.3	23.1	62.1	(Li et al. 2013)
2008	Shanghai	121.43	31.2	53.9	(Geng et al. 2013)
2008	Shanghai	121.48	31.34	52	(He et al. 2010)
2009	Beijing	116.41	40.04	80.5	(Chen et al. 2014b)
2009	Beijing	116.37	39.97	64.6	(Liu et al. 2015b)
2009	Beijing	116.47	39.95	97.5	U.S. Consulate
2009	Guangzhou	113.3	23.13	56	(Kuang et al. 2015)
2009	Guangzhou	113.3	23.1	50.2	(Li et al. 2013)
2009	Shanghai	121.43	31.18	44.4	(Yin et al. 2011)
2010	Beijing	116.41	40.04	80.9	(Chen et al. 2014b)
2010	Beijing	116.37	39.97	73.7	(Liu et al. 2015b)
2010	Beijing	116.47	39.95	98.2	U.S. Consulate
2010	Guangzhou	113.3	23.1	57.2	(Li et al. 2013)
2010	Shanghai	121.41	31.15	47.4	Li and Pan, 2013
2011	Beijing	116.37	39.97	68.4	(Liu et al. 2015b)
2011	Beijing	116.47	39.95	93.9	U.S. Consulate
2011	Guangzhou	113.3	23.1	47.7	(Li et al. 2013)

Year	City	Longitude (°E)	Latitude (°N)	$PM_{2.5}$ (μg/m^3)	Reference
2011	Shanghai	121.42	31.17	49	(Zhou et al. 2016a)
2011	Shanghai	121.43	31.17	48	(Wang et al. 2016)
2012	Beijing	116.37	39.97	71.5	(Liu et al. 2015b)
2012	Beijing	116.47	39.95	88.3	U.S. Consulate
2012	Chengdu	104.1	30.6	86.7	(Chen et al. 2019)
2012	Chongqing	106.5	29.62	71.7	(Chen et al. 2019)
2012	Guangzhou	113.3	23.1	48.4	(Li et al. 2013)
2012	Jinsha	114.2	29.63	48.7	(Zhang et al. 2014)
2012	Nanjing	118.8	32.06	40.9	(Shen et al. 2014)
2012	Neijiang	105.07	29.7	78.6	(Chen et al. 2019)
2012	Shanghai	121.43	31.17	42.6	(Wang et al. 2016)
2012	Shanghai	121.44	31.21	50.8	U.S. Consulate
2012	Shanghai	121.42	31.14	68.4	(Zhao et al. 2015)
2012	Xiamen	118.06	24.61	32.7	(Niu et al. 2013)
2013	Beijing	116.47	39.95	94.7	U.S. Consulate
2013	Guangzhou	113.32	23.12	55.5	U.S. Consulate
2013	Shanghai	121.43	31.17	49.4	(Wang et al. 2016)
2013	Shanghai	121.44	31.21	59.2	U.S. Consulate

Table B2 Selected previous studies on $PM_{2.5}$ attributable mortality assessment in China

Study Year	$PM_{2.5}$ exposure	Baseline mortality	CRF	Mortality (million)	References
2006	WRF-Chem	NBSC	LL	1.7	(Miao et al. 2017)
2010	Satellite/ TM5	WHO	IER	1.08	(Lim et al. 2012)
2010	Satellite/GEOS-Chem	WHO	IER	1.27	(Apte et al. 2015)
2010	EMAC	WHO	IER	1.36	(Lelieveld et al. 2015)
2010	Satellite/GAINS-China	GBD	IER	1.33	(Xie et al. 2016b)
2010	EMAC	WHO	IER	1.33	(Giannadaki et al. 2016)
2010	Satellite/GEOS−Chem	GBD	IER	1.02	(Zhao et al. 2017)
2010	Satellite/four methods	GBD	IER	1.27	(Wang et al. 2018a)
2012	Satellite/TSM	NHFPCC	IER	1.25	(Liu et al. 2017b, 2017a)
2013	Ground measurements	NBSC	IER	1.37	(Liu et al. 2016)
2013	Ground measurements	NBSC	LL	3.03	(Fang et al. 2016)
2013	Satellite	WHO	IER	0.91	(IHME 2016)
2013	CMAQ	WHO	IER	1.3	(Hu et al. 2017a)
2013				2.19	
2014	Satellite/LUR	NBSC	SCHIF	1.94	(Li et al. 2018b)
2015				1.65	
2014	Ground measurements	WHO	IER	1.6	(Rohde and Muller 2015)

Study Year	$PM_{2.5}$ exposure	Baseline mortality	CRF	Mortality (million)	References
2015	Ground measurements	NBSC and GBD (Matus et al. 2012)	IER	1.52	(Song et al. 2017)
2015	Ground measurements		IER	1.85	(Zhang et al. 2017)
2015 /2016	Ground measurements	NHFPCC	IER	1.13 /1.09	(Feng et al. 2017)
2015	WRF-CMAQ	Ministry of Health of China	IER	1.1	(Zheng et al. 2017)
2015	Satellite/GEOS-Chem	WHO	IER	1.11	GBD 2015 (2017)
2016	Satellite/GEOS-Chem	WHO	IER	1.08	GBD 2016 (2017)
2016	Ground monitoring	GBD	IER	0.96	(Maji et al. 2018b)

Note: TM5: Tracer Model 5; WRF-Chem: the Weather Research and Forecasting (WRF) model coupled with Chemistry; EMAC: the ECHAM/MESSy Atmospheric Chemistry model; CMAQ: Community Multi-scale Air Quality Model; GEOS-Chem: the Goddard Earth Observing System Chemical Model with Chemistry; LUR: Land Use Regression; TSM: Two-Stage Model; NBSC: National Bureau of Statistics of China; WHO: World Health Organization; GBD: Global Burden of Disease; NHFPCC: National Health and Family Planning Commission of China ERF: Exposure-response function; LL: Log-linear function; IER: Integrated Exposure Risk function; SCHIF: Shape Constrained Health Impact Function.

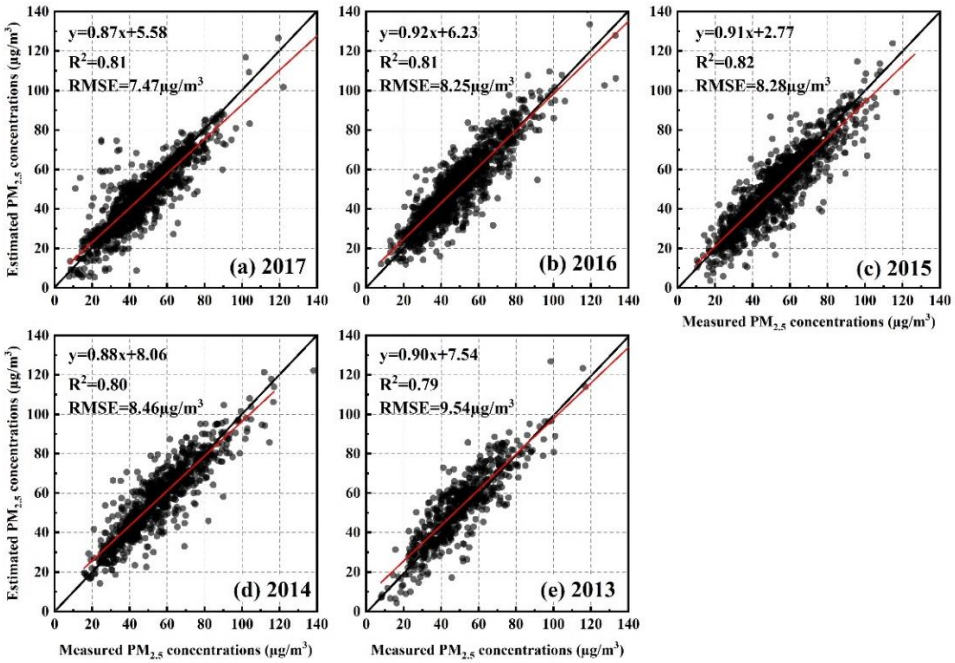

Figure B1 Validation of annual $PM_{2.5}$ concentrations using semi-GWR model from 2013 to 2017

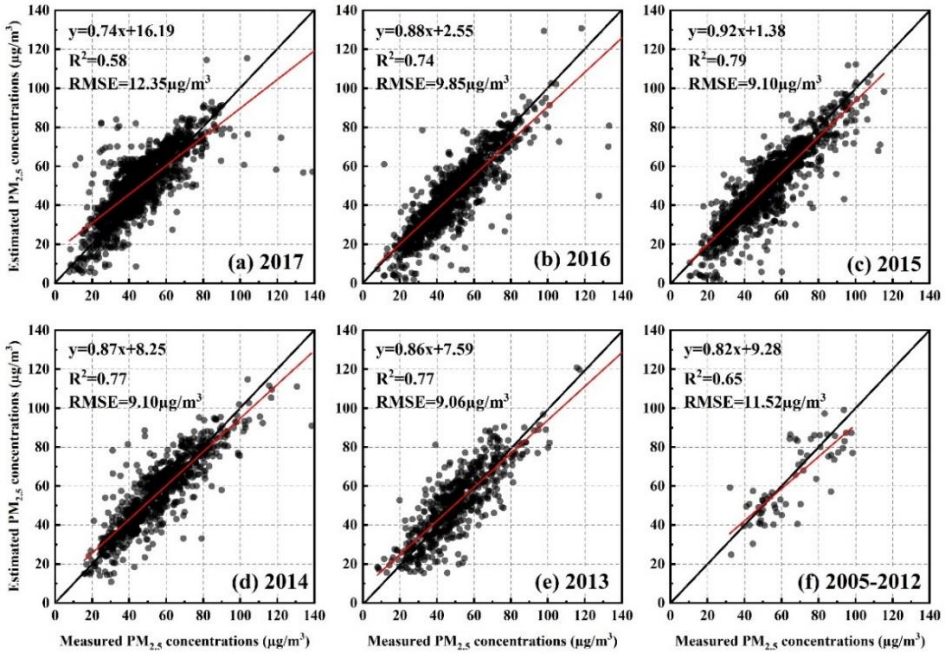

Figure B2 Validation of annual $PM_{2.5}$ concentrations based on GEOS-Chem model from 2005 to 2017

Table B3 Parameters for disease-specific RR calculations (Burnett et al., 2018)

ill	Age range	θ	standard error θ	α	μ	v
IHD	>25	0.2969	0.01787	1.9	12	40.2
	27.5	0.507	0.02458	1.9	12	40.2
	32.5	0.4762	0.02309	1.9	12	40.2
	37.5	0.4455	0.0216	1.9	12	40.2
	42.5	0.4148	0.02011	1.9	12	40.2
	47.5	0.3841	0.01862	1.9	12	40.2
	52.5	0.3533	0.01713	1.9	12	40.2
	57.5	0.3226	0.01564	1.9	12	40.2
	62.5	0.2919	0.01415	1.9	12	40.2
	67.5	0.2612	0.01266	1.9	12	40.2
	72.5	0.2304	0.01117	1.9	12	40.2
	77.5	0.1997	0.00968	1.9	12	40.2
	85	0.1536	0.00745	1.9	12	40.2
Stroke	>25	0.272	0.07697	6.2	16.7	23.7
	27.5	0.4513	0.11919	6.2	16.7	23.7
	32.5	0.424	0.11197	6.2	16.7	23.7
	37.5	0.3966	0.10475	6.2	16.7	23.7
	42.5	0.3693	0.09752	6.2	16.7	23.7
	47.5	0.3419	0.0903	6.2	16.7	23.7
	52.5	0.3146	0.08307	6.2	16.7	23.7
	57.5	0.2872	0.07585	6.2	16.7	23.7
	62.5	0.2598	0.06863	6.2	16.7	23.7
	67.5	0.2325	0.0619	6.2	16.7	23.7
	72.5	0.2051	0.05418	6.2	16.7	23.7
	77.5	0.1778	0.04695	6.2	16.7	23.7
	85	0.1368	0.03611	6.2	16.7	23.7
COPD	>25	0.251	0.06762	6.5	2.5	32
LC	>25	0.2942	0.06147	6.2	9.3	29.8
LRI	>25	0.4468	0.11735	6.4	5.7	8.4

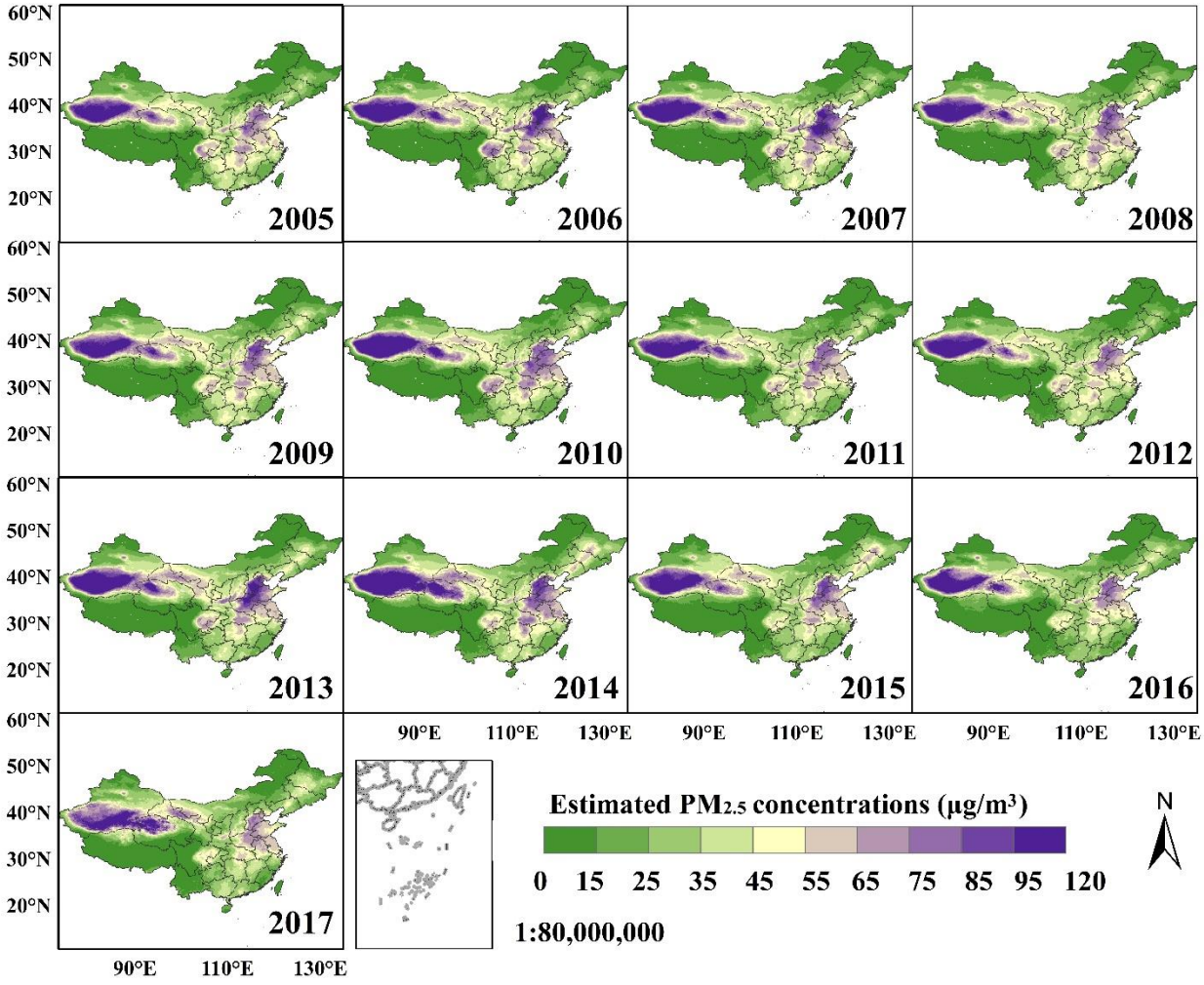

Figure B3 Spatial distributions of annual mean $PM_{2.5}$ concentrations from 2005 to 2017

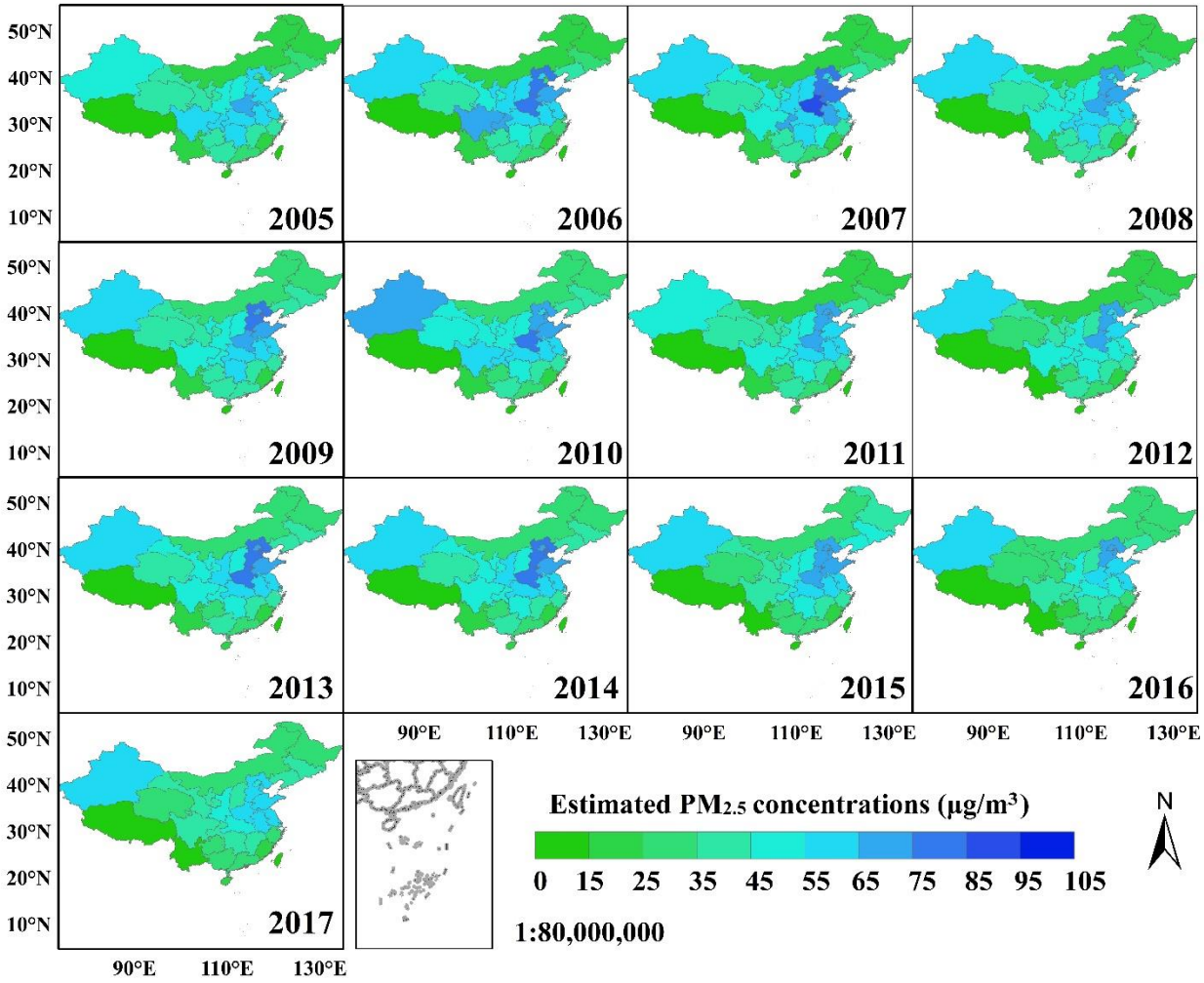

Figure B4 Spatial distributions of population-weighted annual mean $PM_{2.5}$ concentrations from 2005 to 2017

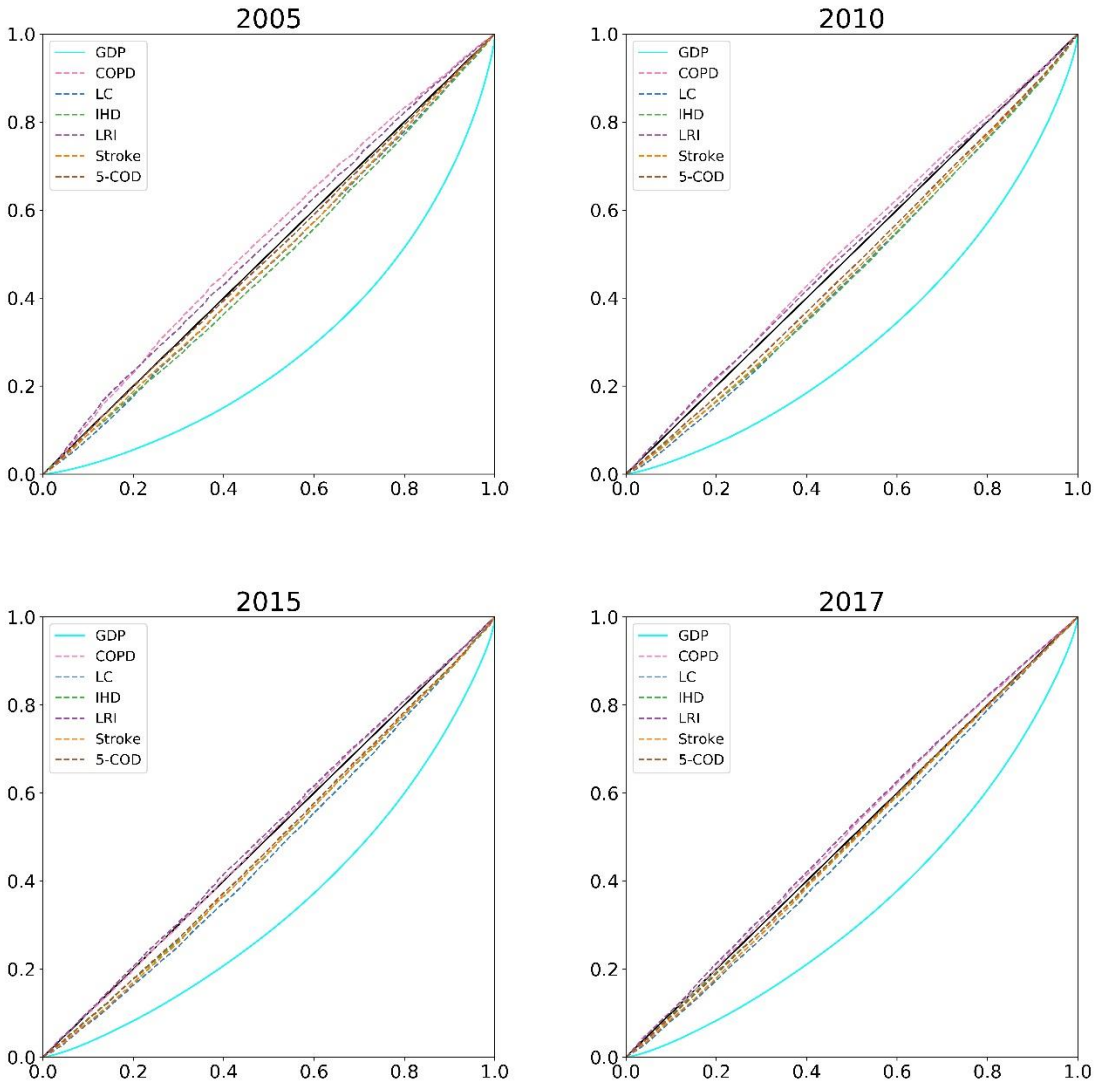

Figure B5 National Lorenz curves for $PM_{2.5}$ attributable mortalities and economic development during 2005-2017

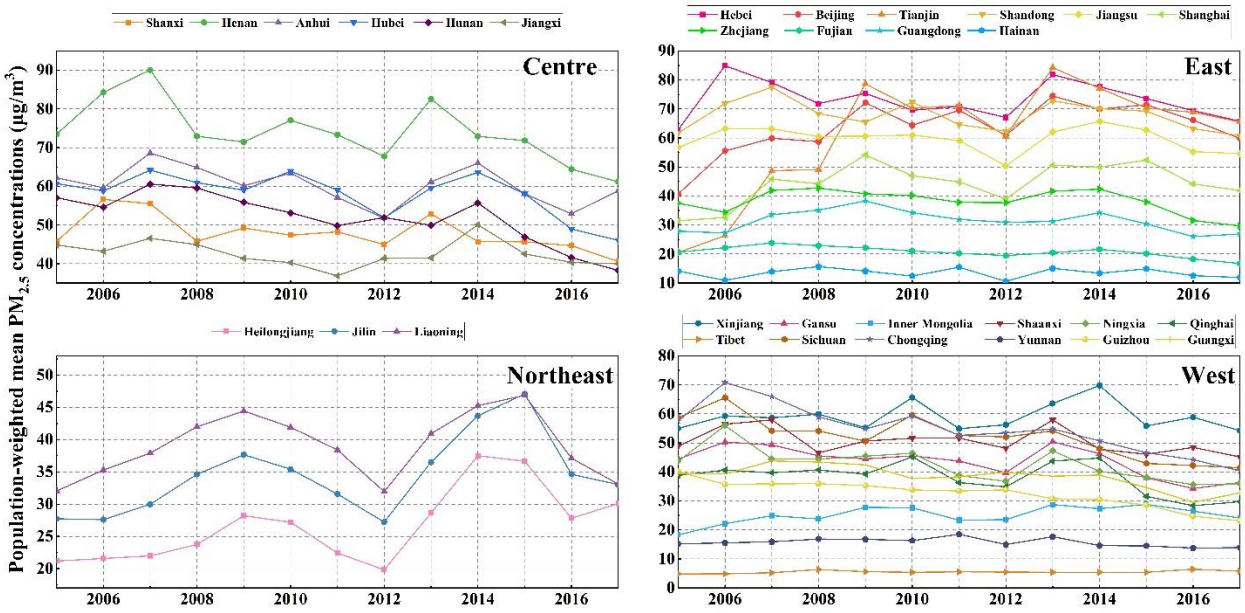

Figure B6 Provincial trends of population-weighted mean $PM_{2.5}$ concentrations from 2005 to 2017

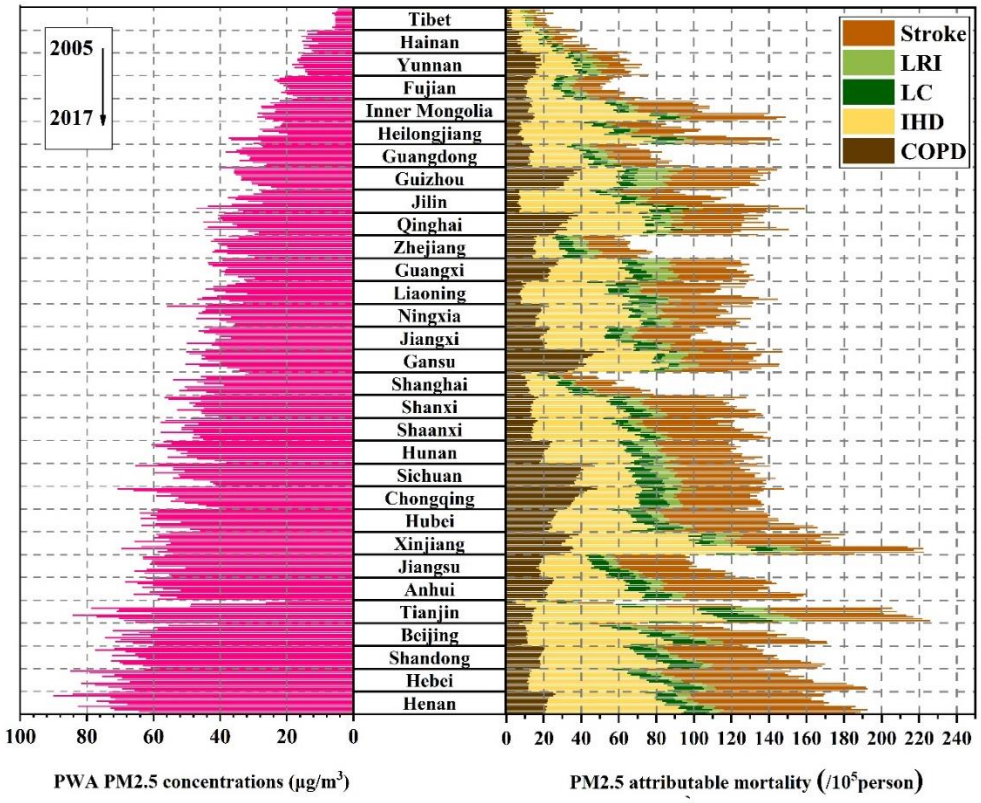

Figure B7 Provincial mortality per 100.000-person attributable to $PM_{2.5}$ during 2005-2017

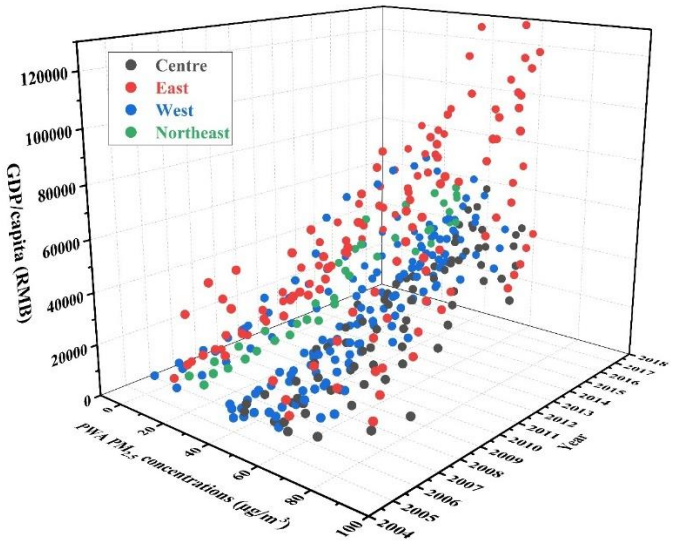

Figure B8 The relations between provincial economic development and $PM_{2.5}$ exposure in four regions during 2005-2017

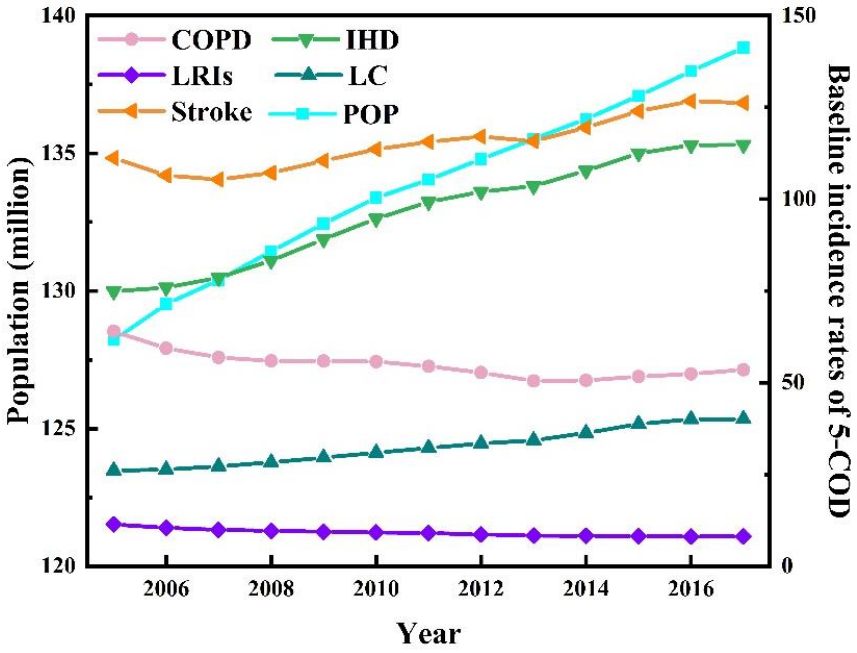

Figure B9 Time-series of population and baseline incidence rates during 2005-2017